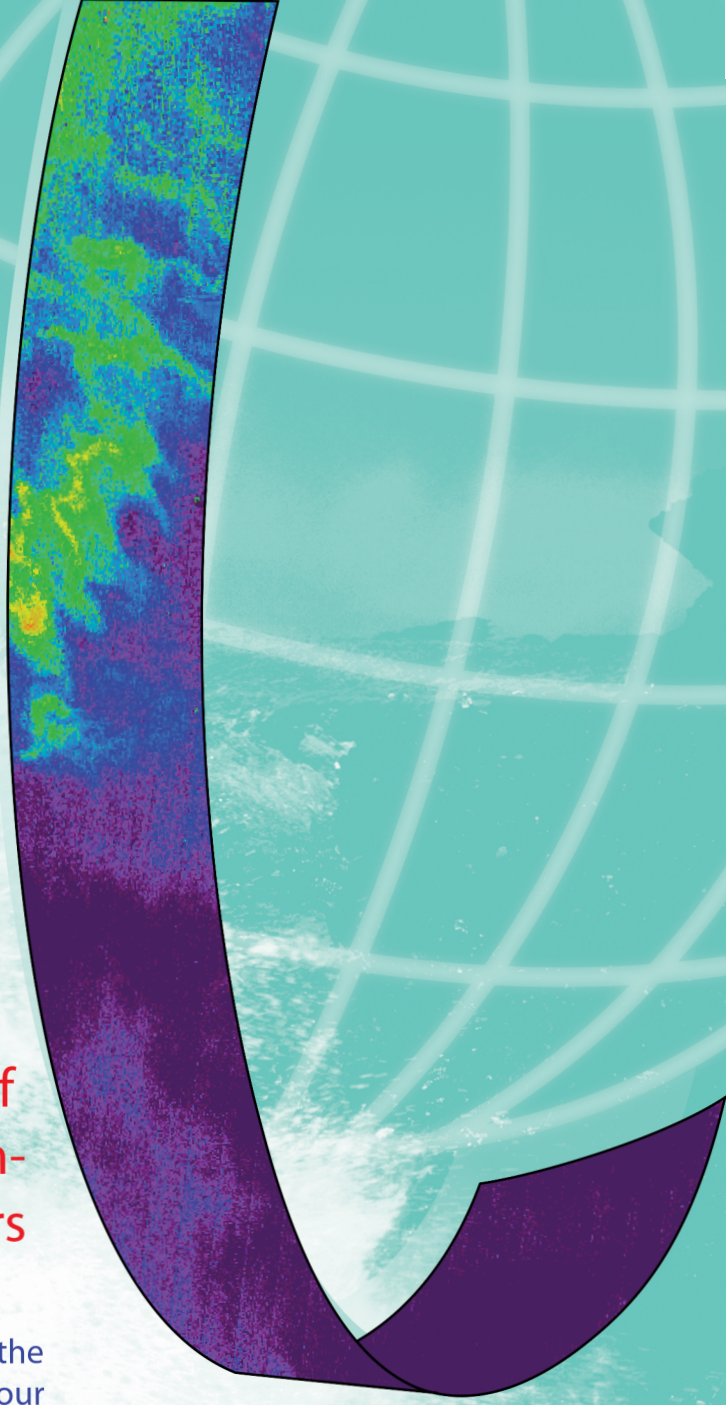

In-flight Calibration of Satellite Ocean-Colour Sensors

Reports of the
International Ocean-Colour
Coordinating Group

REPORT NUMBER 14

IOCCG

An Affiliated Program of SCOR
An Associate Member of CEOS

In the IOCCG Report Series:

1. *Minimum Requirements for an Operational Ocean-Colour Sensor for the Open Ocean (1998)*
2. *Status and Plans for Satellite Ocean-Colour Missions: Considerations for Complementary Missions (1999)*
3. *Remote Sensing of Ocean Colour in Coastal, and Other Optically-Complex, Waters (2000)*
4. *Guide to the Creation and Use of Ocean-Colour, Level-3, Binned Data Products (2004)*
5. *Remote Sensing of Inherent Optical Properties: Fundamentals, Tests of Algorithms, and Applications (2006)*
6. *Ocean-Colour Data Merging (2007)*
7. *Why Ocean Colour? The Societal Benefits of Ocean-Colour Technology (2008)*
8. *Remote Sensing in Fisheries and Aquaculture (2009)*
9. *Partition of the Ocean into Ecological Provinces: Role of Ocean-Colour Radiometry (2009)*
10. *Atmospheric Correction for Remotely-Sensed Ocean-Colour Products (2010)*
11. *Bio-Optical Sensors on Argo Floats (2011)*
12. *Ocean-Colour Observations from a Geostationary Orbit (2012)*
13. *Mission Requirements for Future Ocean-Colour Sensors (2012)*
14. *In-flight Calibration of Satellite Ocean-Colour Sensors (this volume)*

The printing of this report was sponsored and carried out by the Joint Research Centre (JRC) of the European Commission, which is gratefully acknowledged. Ewa Kwiatkowska (EUMETSAT) and Giuseppe Zibordi (JRC) are also thanked for their helpful comments.

Reports and Monographs of the International Ocean-Colour Coordinating Group

An Affiliated Program of the Scientific Committee on Oceanic Research (SCOR)
An Associated Member of the (CEOS)

IOCCG Report Number 14, 2013

In-flight Calibration of Satellite Ocean-Colour Sensors

Edited by:
Robert Frouin (Scripps Institution of Oceanography, La Jolla, California, USA)

Report from an IOCCG working Group on In-flight Calibration of Ocean-Colour Sensors, chaired by Robert Frouin, and based on contributions from (in alphabetic order):

David Antoine	Laboratoire d'Océanologie de Villefranche (France)
Steven Delwart	European Space Research Institute (Italy)
Pierre-Yves Deschamps	Laboratoire d'Optique Atmosphérique (France)
Robert E. Eplee	NASA Goddard Space Flight Center (USA)
Cédric G. Fichot	University of South Carolina (USA)
Bertrand Fougnie	Centre National d'Etudes Spatiales (France)
Robert Frouin	Scripps Institution of Oceanography (USA)
Howard R. Gordon	University of Miami (USA)
Jean-Paul Huot	ESA/ESTEC (The Netherlands)
Gerhard Meister	NASA Goddard Space Flight Center (USA)
Andreas Neumann	German Aerospace Center (Germany)
Mayumi Yoshida	Remote Sensing and Technology Center, Tsukuba (Japan)

Series Editor: Venetia Stuart

Correct citation for this publication:

IOCCG (2013). In-flight Calibration of Satellite Ocean-Colour Sensors. Frouin, R. (ed.), Reports of the International Ocean-Colour Coordinating Group, No. 14, IOCCG, Dartmouth, Canada.

The International Ocean-Colour Coordinating Group (IOCCG) is an international group of experts in the field of satellite ocean colour, acting as a liaison and communication channel between users, managers and agencies in the ocean-colour arena.

The IOCCG is sponsored by Centre National d'Etudes Spatiales (CNES, France), Canadian Space Agency (CSA), Commonwealth Scientific and Industrial Research Organisation (CSIRO, Australia), Department of Fisheries and Oceans (Bedford Institute of Oceanography, Canada), European Space Agency (ESA), European Organisation for the Exploitation of Meteorological Satellites (EUMETSAT), Helmholtz Center Geesthacht (Germany), National Institute for Space Research (INPE, Brazil), Indian Space Research Organisation (ISRO), Japan Aerospace Exploration Agency (JAXA), Joint Research Centre (JRC, EC), Korea Institute of Ocean Science and Technology (KIOST), National Aeronautics and Space Administration (NASA, USA), National Centre for Earth Observation (NCEO, UK), National Oceanic and Atmospheric Administration (NOAA, USA), and Second Institute of Oceanography (SIO), China.

http: //www.ioccg.org

Published by the International Ocean-Colour Coordinating Group,
P.O. Box 1006, Dartmouth, Nova Scotia, B2Y 4A2, Canada.
ISSN: 1098-6030

Printed by the Joint Research Centre (JRC) of the European Commission

— In Memoriam —

To the memory of Andreas Neumann (1957 — 2012)
Esteemed Colleague and Friend

Photograph courtesy of Peter Gege, German Aerospace Center (DLR)

Contents

Chapter 1

Introduction

Robert Frouin and Andreas Neumann

Radiometric calibration of an optical sensor is the process that establishes the link between sensor output signal (voltage, digital number) and absolute physical values of the sensor input signal (radiant energy), i.e., the overall transfer function of the sensor. It is part of the sensor characterization, with respect to spectral and radiometric parameters. The parameters to be determined during the calibration process depend on sensor principle, detector type, and application.

Accurate radiometric calibration of space borne ocean-colour sensors is essential to retrieving geophysical variables (concentration of water constituents, inherent optical properties, aerosol content, etc.) quantitatively in terms of absolute values. The retrieval algorithms use values of spectral radiance (or derived reflectance) in the inversion procedures, and the accuracy of the derived product strongly depends on the accuracy of the radiance measurement. Furthermore, the evaluation of the remotely sensed quantities, including models and algorithms, requires a link between the data acquired in orbit and surface-based measurements.

The accuracy requirements for absolute calibration are especially demanding in ocean-colour remote sensing, because the extracted signal is relatively small compared with the measured signal, which is dominated by atmospheric scattering. More than 90% of the measured radiance in the blue and green may originate from the atmosphere and surface, i.e., may not contain any information about the water body. Atmospheric correction subtracts the atmospheric scattering and surface signal, but amplifies the errors on the retrieved ocean parameters due to imperfect radiometric calibration. Consequently, retrieving marine reflectance to within $\pm 5\%$ in the blue, in clear waters (the objective of major satellite ocean-colour missions), requires knowing the top-of-atmosphere reflectance to within a fraction of one percent. The situation is further complicated by the existence of several satellite missions that independently employ a variety of calibration techniques (but not the same) to achieve good performance. Consequently, the ocean-colour products from different instruments may be biased, making it difficult to merge the data correctly and generate consistent long-term time series.

Radiometric calibration is generally performed in the laboratory before launch, but accuracy is not perfect and sometimes insufficient. In fact, this engineering

calibration refers to standards while science applications require a calibration with respect to solar irradiance. The calibration standards provide reference light sources with known spectral distribution, but due to lower temperature they generally do not correspond to the spectrum of the Sun, with signals too low in the blue and too high in the red. The pre-launch calibration covers all measurements by laboratory means before instrument delivery that describe spectral and radiometric sensor performance. The objective is to provide an initial set of parameters that serves as a reference for monitoring in-orbit performance and/or in-orbit calibration, as well as initial functions to be used for data processing to basic physical values. The procedures involve extensive laboratory set-ups and careful and time-consuming measurements.

Pre-launch calibration needs to be checked in orbit, because instruments are subject to degradation after launch. The reasons include out-gassing when the satellite leaves the atmosphere, aging of the optics, contamination of optical parts in orbit, and exposure of optical parts, detectors, and electronics to space radiation. In-orbit calibration is therefore essential to ensure valuable data during the lifetime of the instrument through monitoring of sensor stability. The process covers all measurements made in orbit to either re-calibrate the sensor or to monitor and quantify changes in instrument parameters. This gives the basis to account for possible sensor changes in the data processing and makes sure that the observed changes exist in reality, i.e., are the manifestation of geophysical phenomena. To address sensor degradation, satellite platforms are often equipped with onboard calibration devices. Indirect, so-called “vicarious", methods are also used, either alternatively (in the absence of onboard calibrators) or to check the onboard device.

Absolute calibration in orbit of ocean-colour sensors is usually performed using the Sun as a calibration source. An onboard diffuser is required to convert the Sun irradiance into radiance. The advantages are that the Sun is the most stable light source, the complete sensor performance from entrance optics to detector is accounted for, and the nadir measurement can be referred to the natural illumination source. A problem is the degradation of the diffuser and the use of moving parts to position the diffuser in front of the entrance optics. Vicarious techniques based on Earth target observations can be used alternatively and complementarily. They include the Rayleigh scattering technique for blue spectral bands, which exploits the fact that molecular scattering can be computed accurately and may dominate the top-of-atmosphere radiance in some situations. The absolute calibration in the blue bands can then be transferred to longer wavelengths using the specular reflection of the Sun over the ocean. The top-of-atmosphere radiance can also be computed from measurements of marine reflectance and atmospheric parameters using an accurate radiation transfer code. Since atmospheric correction is necessary to retrieve water-leaving radiance (the variable of interest), a “system" vicarious calibration, in which retrieved and measured water-leaving radiance are forced into agreement, may ultimately allow sufficient accuracy, within the $\pm 5\%$ requirement on

marine reflectance, for science applications.

For relative calibration in orbit, i.e., monitoring and quantification of sensor parameters with respect to a reference status (pre-launch calibration or initial post-launch status), one may use built-in light sources such as lamps or diodes and extra-terrestrial sources like the Moon. Lamps do not necessarily cover the entire optical path, depending on construction, but they allow linearity checks and other features (spectral properties). The problems are long-term stability and spectral irradiance distribution. The Moon, on the other hand, covers the entire path from entrance optics to detector, but it does not fill the total field of view for push-broom instruments, and may cause problems due to spatial heterogeneity. Inter-band and multi-temporal calibration can also be achieved by viewing high and dense clouds. Such clouds are white spectrally, isotropic, and minimally influenced by the surface and atmosphere below and above. Other suitable targets are desert sites, provided that they are homogeneous spatially and stable with time.

Since the Coastal Zone colour Scanner (CZCS) onboard NIMBUS-7, ocean-colour sensors have matured, capabilities have improved, systems are no longer experimental but operational, and several satellites carrying different sensors are presently providing ocean-colour data on a regular basis over long time periods. These sensors may acquire data of the same phenomena at distinct overpass times with specific viewing geometry and spectral and spatial resolution. The separate and independent measurements may complement each other (e.g., to improve spatial coverage of ocean-colour products) and allow new science through synergistic investigations. Therefore a common, absolute scale is necessary for all sensors. This is especially important for generating consistent long-term records from multiple satellites. Since all sensors are calibrated before launch to a laboratory standard, the individual calibrations can be linked together using transfer radiometers. Once in orbit, however, the situation is more complicated, but intercalibration of the sensors can be achieved by common measurements of dedicated targets or sources like the Sun, the Moon, and selected Earth sites.

This report provides a review of techniques developed and employed for the radiometric calibration of satellite ocean-colour sensors while they operate in orbit. In Chapter 2, basic definitions and concepts are given, as well as accuracy requirements to generate ocean-colour products of sufficient quality for science applications. In Chapter 3, the techniques that utilize onboard calibration devices, including lamps and diffusers, require a specific spacecraft manoeuvre, and/or use Space targets (Sun and Moon) are described. In Chapter 4, the focus is on vicarious calibration, absolute and relative, using natural Earth targets, including “system" vicarious calibration. The Earth targets may be located at the surface or in the atmosphere, over the ocean or land, and they may exploit specific physical processes, such as molecular scattering and Fresnel reflection, and viewing conditions. All the techniques, whether using onboard artificial light sources or Space and Earth targets, are presented with their accuracy, advantages, and limitations. Application examples are given. Finally,

in view of the available techniques and their characteristics, recommendations are given on how to proceed with the radiometric calibration of ocean-colour sensors during operational phase, in order to generate and maintain quality retrievals of water-leaving radiance during mission lifetime, including selection of calibration sites, requirements for *in situ* measurements, and sensor inter-calibration.

Chapter 2

Definitions and Requirements

Howard R. Gordon

2.1 Scope of the Review

The goal of this introductory review is to provide (1) the basic definitions of the quantities involved in the radiometric calibration of ocean-colour sensors, (2) the principle ideas and methodology of radiance and reflectance-based calibration, (3) some of the issues relating to non-ideal sensors (sensor characterization), (4) the calibration accuracy that is required to generate ocean-colour products with the desired accuracy, and (5) vicarious calibration methods for achieving this accuracy.

2.2 Definitions and Concepts

All ocean-colour sensors measure *radiance*. Figure 2.1 provides the operational definition of radiance. A detector of area A_d (sensitive only to radiation in a small band of wavelengths $\lambda \pm \Delta\lambda/2$ around a central wavelength λ) is allowed to view a scene with a field of view that is restricted to the solid angle Ω. If the radiant power measured by the detector is P, then the detector is said to measure a *radiance* L given by

$$L(\lambda) = \frac{P}{A_d \Omega \Delta\lambda}.$$

The SI units of radiance are W/(m^2-Steradian-nanometers), but an equally popular unit is mW/(cm^2-Steradian-μm). Note that in this equation P is proportional to $\Delta\lambda$ so as $\Delta\lambda \to 0$, L approaches a well-defined limit. The radiance measured in this way is sometimes referred to as the *field radiance* as it is not always associated with a physical surface (e.g., the radiance of the sky). The device shown – the detector *plus* some form of solid angle restrictor – is called a *radiometer*. If the radiometer is pointed toward a physical surface, and if there are no losses (by scattering or absorption) or gains (by light sources or emitting gases) between the surface and the radiometer, e.g., if the surface and the radiometer are separated by a short distance in vacuum (or practically, in the visible spectrum, by a short distance in air), then the radiance measured by the radiometer is also the radiance leaving the surface: in

the absences of losses, the radiance is conserved in propagating from the surface to the radiometer.

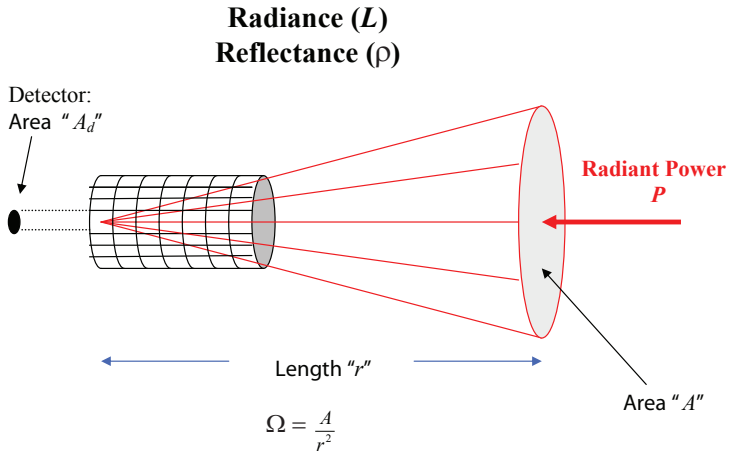

Figure 2.1 Schematic of a radiometer. A detector of area A_d (sensitive only to radiation in a small band of wavelengths $\lambda \pm \lambda/2$ around a central wavelength λ) is allowed to view a scene with a field of view that is restricted to the solid angle Ω. The tube restricting the field of view of the detector in the schematic is usually referred to as a *Gershun tube.*

The ocean-colour sensors of interest here are located at the top of the atmosphere (TOA) aimed toward the Earth in such a manner as to measure the radiance escaping from the TOA. They measure the radiance L_t that is the result of sunlight being reflected from the ocean-atmosphere system. The associated reflectance ρ_t is defined by

$$\rho_t = \frac{\pi L_t}{F_0 \cos\theta_0},$$

where F_0 is the instantaneous solar irradiance (the radiant power of the solar beam per unit area, in a wavelength interval $\Delta\lambda$, perpendicular to the Sun's rays, measured at the top of the atmosphere) and θ_0 is the solar zenith angle. In fact, for the radiance measured anywhere within the ocean atmosphere system, the associated reflectance is defined in the same manner as above.

We shall use the term *diffuse source* to represent a (plane) source of radiance for which the measured radiance is independent of the angle (with respect to the normal to the plane) with which it is viewed in the measurement of the radiance. A sheet of white paper (non-glossy) illuminated by a small distant source of light and viewed in reflection is a good approximation to a diffuse source (and is referred to as a *Lambertian reflector*). Near-Lambertian reflectors with known (and usually near 100% reflecting) are usually referred to as calibration *plaques* or *reflectance plaques.* Another example is a spherical shell painted on the inside with flat white paint, illuminated by sources that are inside, and having a circular hole to allow light to escape. The hole itself then approximates a diffuse source in that the radiance

exiting the plane of the hole is nearly independent of direction. Devices such as this are commercially available and are referred to as *calibration spheres*.

2.3 Radiance- and Reflectance-Based Calibration of Ideal Sensors

The detector in Figure 2.1 is a device that produces an electrical output dependent on the radiant power falling on its surface. Calibration is the act of determining the relationship between the electrical response and the magnitude of the radiance inducing the electrical response. There are two methods of calibration that are useful for ocean-colour remote sensing. These are *radiance-based*, where the radiometer is aimed toward a source of known radiance, and *reflectance-based*, where the radiometer is aimed toward an illuminated target of known reflectance. These methods are described in this section.

2.3.1 Radiance-based calibration:

Consider an ideal sensor (assumed to have an electrical response that is a linear function of the radiant power incident on it) that responds only to radiation in a small band of wavelengths $\lambda \pm \Delta\lambda/2$ around a central wavelength λ. Then viewing a diffuse source (calibration source) of known radiance $L_c(\lambda)$, e.g., a calibration sphere or a plaque illuminated by a known power per unit area, the sensor's response V_c (voltage, current, etc.) will be

$$V_c(\lambda) = k_L(\lambda)L_c(\lambda).$$

Then if the same sensor views a scene of radiance $L(\lambda)$, the sensor's response will be

$$V(\lambda) = k_L(\lambda)L(\lambda) = [V_c(\lambda)/L_c(\lambda)] \times L(\lambda),$$

so the measurement of $V(\lambda)$ then provides measurement of the radiance of the scene. The MODIS sensor has an on-board calibration sphere that enables the *calibration constant* $k_L(\lambda)$ to be monitored with time.

2.3.2 Reflectance-based calibration:

Let the same sensor view a Lambertian reflectance plaque of reflectance R_p, defined to be the power per unit area reflected (reflected *irradiance*) from the plaque divided by the power per unit area illuminating the plaque (incident *irradiance*). If the plaque is illuminated by irradiance E_p the reflected radiance observed by the sensor will be R_pE_p/π, and the sensor responds with an electrical signal

$$V_p(\lambda) = k_L(\lambda)R_p(\lambda)E_p(\lambda)/\pi.$$

Now, if the sensor views a scene that is illuminated by an irradiance E, its response will be

$$V(\lambda) = k_L(\lambda)\rho(\lambda)E(\lambda)/\pi,$$

so

$$V(\lambda)/V_p(\lambda) = \rho(\lambda)E(\lambda)/R_p(\lambda)E_p(\lambda).$$

If $E(\lambda)$ and $E_p(\lambda)$ are the same (as would be the case if the reflectance plaque was carried along with the sensor in orbit and illuminated by the Sun as in Figure 2.2), then

$$V(\lambda)/V_p(\lambda) = \rho(\lambda)/R_p(\lambda),$$

and measurement of $V(\lambda)$ provides $\rho(\lambda)$. Reflectance plaques are in fact attached to the sensors on SeaWiFS and MODIS to monitor the calibration in orbit as discussed next.

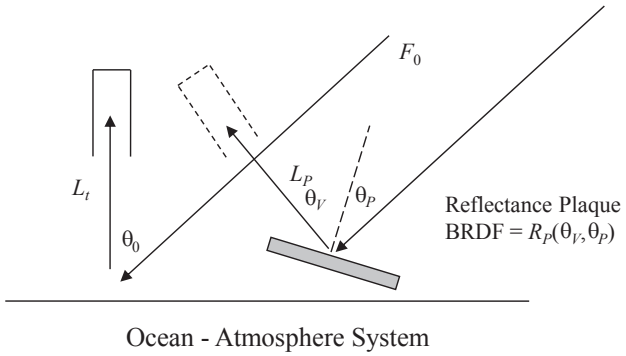

Figure 2.2 Schematic describing the use of a reflectance plaque to effect on-orbit reflectance calibration of SeaWiFS and MODIS. The radiometer first views the ocean-atmosphere system and records a radiance L_t. It the views a reflectance plaque having a known bi-directional reflectance distribution function (BRDF) and measures a radiance L_P.

Consider the situation displayed in Figure 2.2. The sensor first views the Earth and measures a voltage or current $V_t = k_r L_t = k_r F_0 \rho_t \cos(\theta_0)/(\pi a^2)$, where a is the Earth-Sun distance in Astronomical Units (AU). Then the sensor views the in-orbit reflectance plaque and measures a voltage or current $V_P = k_r L_P = k_r F_0 R_P \cos(\theta_P)/(\pi a^2)$. Note that R_P is a known function (measured in the laboratory prior to launch) of the viewing angles θ_0 and θ_P. Therefore,

$$\rho_t \cos(\theta_0) = \frac{V_t}{V_P} R_P \cos(\theta_P).$$

The reader should note that F_0 is not needed to find ρ_t. This is important because error in measurements of F_0 would cause a similar error in computing the reflectance associated with a radiance-based measurement of L_t.

It has been the experience that the reflectance of solar diffuser plaques in orbit will degrade with time. If account is not taken of this degradation, the estimated

ρ_t will be too large. This is remedied by monitoring the stability of R_P (SeaWiFS uses the Moon, and MODIS uses an onboard monitoring device and occasional Lunar views).

2.4 Characterization of Non-Ideal Sensors

Assuming the calibration procedures described above are exact, i.e., the radiance of the calibration sources or the reflectance of the calibration plaques are precisely known, all sensors still have non-ideal performance that must be understood to properly utilize them. These need to be *characterized*. Among these are:

- *Out-of-band response*: the detector responds not only to radiant power in a small band of wavelengths $\lambda \pm \Delta\lambda/2$ around a central wavelength λ, but has some response to radiant power outside this interval.
- *Polarization sensitivity*: the sensor's response is dependent on the polarization of the radiance it is measuring.
- *Bright target response*: a given pixel may respond not only to radiant power within its field of view, but to power outside its field of view as well (this is particularly serious for array detectors).
- *Non-linearity*: the relationship between the electrical response and the radiant power is non-linear.

We will discuss the first three of these in some detail.

2.4.1 Out-of-band response:

Sensors do not view the Earth with narrow spectral bands as we have been assuming (Gordon, 1995). Figure 2.3 shows the pre-launch measured spectral response of SeaWiFS Band 8 (nominally 865 nm). The quantity provided $S_8(\lambda)$ is the electrical output of SeaWiFS from a nearly monochromatic input of radiance 1 mW/(cm^2 - Steradian-μm) at λ. Clearly, the notion that the sensor views only a narrow band of wavelengths is an oversimplification.

For a broad spectral source, e.g., the ocean-atmosphere system, the output of the sensor is proportional to

$$\langle L(\lambda)\rangle_{S_i} \equiv \frac{\int L(\lambda)S_i(\lambda)d\lambda}{\int S_i(\lambda)d\lambda}.$$

For SeaWiFS 865 band, approximately 9% of the Rayleigh component $\langle L_r(\lambda)\rangle_{S_8}$ of the radiance at the TOA ($\propto \lambda^{-4}$) is backscattered from wavelengths below 600 nm! Thus, the influence of even an apparently small amount of out-of-band sensitivity can be significant, especially when the radiance is a strong function of wavelength. With out-of-band response, the "measured" radiance is dependent on the spectral distribution of the calibration source, which could be the Moon, a calibration lamp, solar diffuser, or in the case of vicarious calibration, the ocean (Figure 2.4). Even if

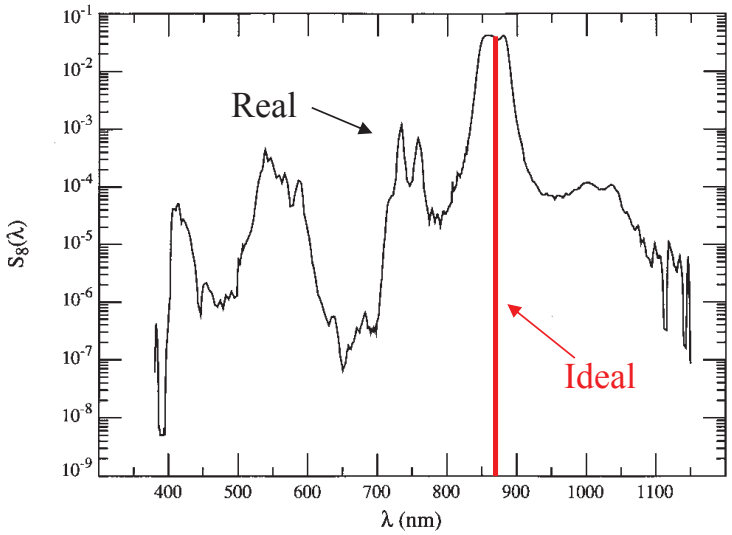

Figure 2.3 The spectral response of SeaWiFS band 8 (nominally 845–885 nm). (From Gordon, 1995.)

the radiances at λ_0 from the various sources, in the somewhat pathological example, for the $S(\lambda)$ shown in Figure 2.4 are all the same at λ_0, the "measured" radiances will all be different. This suggests vicarious calibration, i.e., using the radiance reflected from the ocean-atmosphere system, will be best because the spectral distribution of the calibration source (the ocean-atmosphere system) will be similar to that of the radiance the sensor will actually be measuring in operation; however, characterization of the out-of-band response is still essential.

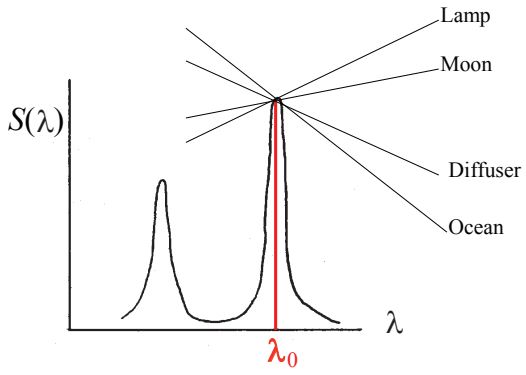

Figure 2.4 Schematic showing how various sources all having the same radiance at λ_0 but different spectral distributions would produce considerably different measured radiance $\langle L \rangle_S$.

2.4.2 Polarization sensitivity

The polarization sensitivity of a radiometer can be understood in the following manner (Gordon *et al.*, 1997). Shine linearly polarized radiance from a source of radiance L_{Source} into the instrument. Let the polarization (direction of E field) be specified by the angle χ, in a plane normal to the direction of propagation, with respect to some direction fixed in that plane with respect to the radiometer.

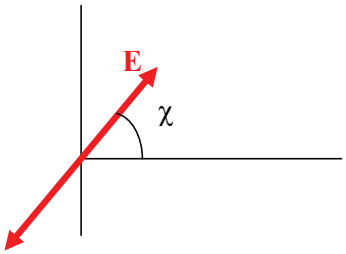

Then, as the angle χ is varied, the radiance measured by the sensor will be

$$L_m(\chi) = M_{11} L_{\text{Source}}[1 + a\cos 2(\chi - \delta)],$$

where M_{11} is a calibration constant ($M_{11} = 1$ if the radiometer is perfectly calibrated). If the incident light is partially polarized rather than fully polarized, i.e., has a degree of polarization $P (0 \le P \le 1)$, then

$$L_m(\chi) = M_{11} L_{\text{Source}}[1 + aP\cos 2(\chi - \delta)]$$

To calibrate the instrument, we use an unpolarized source (*UP*) of known radiance, so

$$L_m^{UP}(\chi) = M_{11} L_{\text{Source}}^{UP},$$

provides M_{11}. Note that this would be the measured radiance for $a = 0$, i.e., an instrument with no polarization sensitivity. Call this L_{True}. Then

$$L_m(\chi) = L_{\text{True}}[1 + aP\cos 2(\chi - \delta)],$$

and if the polarization sensitivity is not addressed, the error in the associated radiance could be as much as $\pm aP$.

Given a and δ (determined through pre-launch characterization) along with P and χ, (characteristic of the radiance exiting the atmosphere), we can find L_{True} from L_m. It should be noted, as we shall see later, that a radiance error of 1% at 412 nm results in a water-leaving radiance error of $\sim$ 10% in low-chlorophyll Case 1 waters.

Potentially, how large can the error be due to polarization sensitivity for ocean-colour sensors? Consider a specific example. Figure 2.5 shows the amplitude (a) of the polarization sensitivity as a function of angle of incidence (AOI) on the scan mirror of MODIS on Terra. (Note that AOI's of 15° and 60° are at the edges of the MODIS scan, west and east, respectively, while 38° is at the center of the scan.) The blue curves are for 412 nm (Band 8) and the red curves for 869 nm (Band 16). For

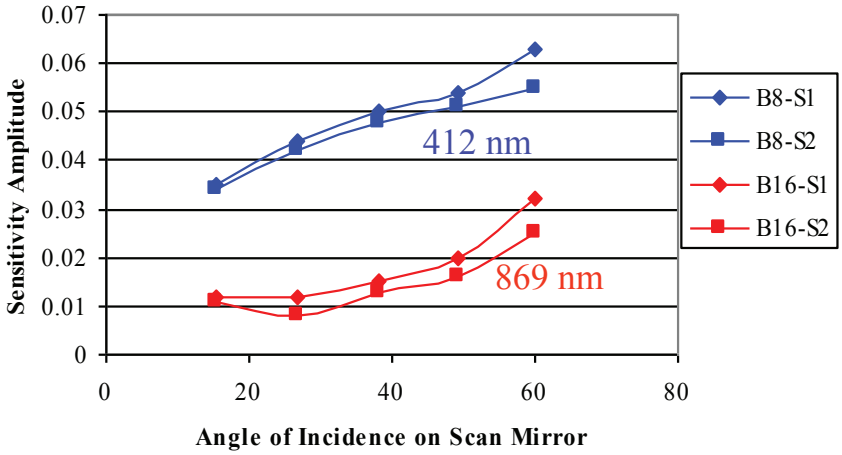

Figure 2.5 Measured polarization sensitivity amplitude of MODIS (on Terra) in the blue and in the near infrared.

each spectral band, the individual curves refer to a specific side of the two-sided scan mirror. Thus, the polarization sensitivity can be several percent in the blue.

To understand the magnitude of the error the polarization sensitivity in Figure 2.5 could induce, we need to know the degree of polarization of the radiance. In the blue, approximately 80% of the total radiance is due to Rayleigh scattering in the atmosphere. Figure 2.6 provides the degree of polarization of the Rayleigh component of the total radiance as a function of position for two successive orbital passes of Terra in December. Notice that there are significant regions of the orbit where the polarization of the Rayleigh component is above 60%. Combining this with the polarization sensitivity amplitude suggests that the induced radiance error at 412 nm could be as much as 3.5% of the total radiance, which, as we will see later, is much too large (it could lead to a normalized water-leaving radiance error of ~ 35%). Thus, polarization sensitivity is a significant issue with MODIS, and may be in future sensors as well. It must be carefully characterized in future sensors if they are to fulfill their promise.

2.4.3 Bright target/internally scattered light.

Modern sensors have large focal planes containing linear or rectangular arrays of detectors. A cloud on one part of the focal plane can influence the signal on another part of the focal plane through internal reflections. This is shown schematically in Figure 2.7. The green circle represents a cloud superimposed over the four focal planes of MODIS. The vertical strips are the individual detector arrays with each strip corresponding to a different spectral band. Each element in an array corresponds to a single pixel. In the blue, the reflectance of a cloud is 4-5 times that of the ocean-atmosphere system, while in the NIR the associated factor is 30-40 times.

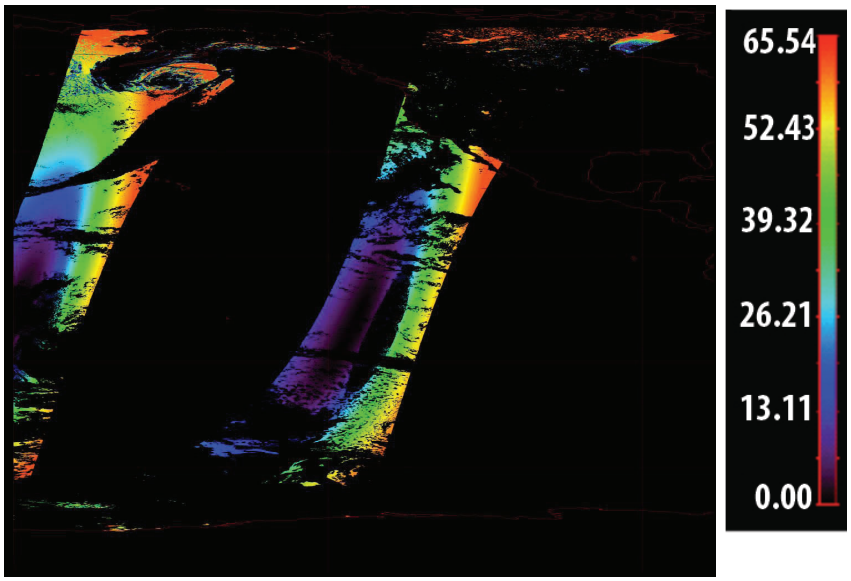

Figure 2.6 Degree of polarization P (in %) of the Rayleigh scattering component of the top-of-atmosphere radiance at 412 nm for an orbital pass in December.

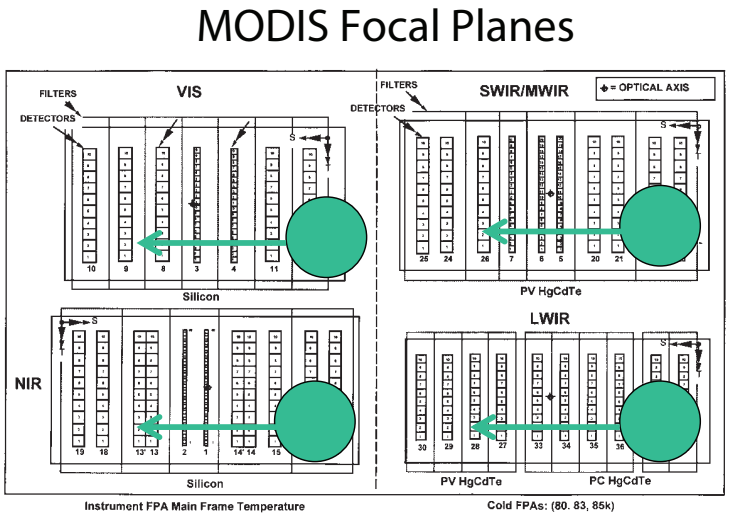

Figure 2.7 Schematic showing a bright cloud (green circle) moving across the four MODIS focal planes (as the instrument scans the scene).

Radiance from the cloud can reflect off a focal plane and be scattered within the focal chamber to another part of the focal plane and thus, even though the cloud might be several pixels from a particular detector, it could provide a significant contribution to the measured radiance, especially in the NIR. This effect must be included in pre-launch characterizations.

2.5 Calibration Requirements for Ocean-Colour Sensors

Figure 2.8 is a schematic of the remote sensing problem. Solar irradiance F_0 is incident at the top of the atmosphere (TOA) at a solar zenith angle θ_0. This results in an upwelling radiance $L_u(z_1, \theta_w, \phi_w)$, just beneath the sea surface, a water-leaving radiance $L_w(z_1, \theta, \phi)$, just above the sea surface, and a radiance $L_t(0, \theta, \phi)$ exiting the TOA. The goal of remote sensing is, given L_t find L_w. Actually, we want $[L_w]_N \equiv L_w / t_s \cos\theta_0$ (Gordon and Clark, 1981), where t_s is the transmittance of F_0 from the TOA to the sea surface. t_s is called the *diffuse transmittance* because it is a transmittance of irradiance, as opposed to the *direct transmittance* which is the transmittance of a beam of collimated radiation.

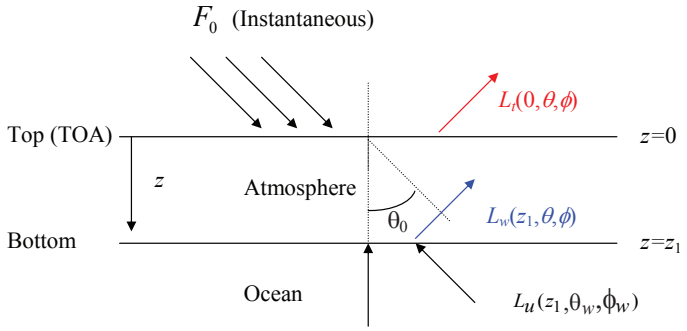

Figure 2.8 Schematic of the remote sensing geometry showing the various radiances discussed in the text.

We will use reflectance ρ rather than radiance L to describe the processes. As described earlier, they are related by

$$\rho = \pi L / F_0 \cos\theta_0$$

The TOA reflectance is (Gordon and Wang, 1994)

$$\rho(\lambda) = \rho_r(\lambda) + \rho_A(\lambda) + t_v(\lambda) t_s(\lambda) [\rho_w(\lambda)]_N,$$

where $\rho_A(\lambda) = \rho_a(\lambda) + \rho_{ra}(\lambda)$, $\rho_r(\lambda)$ is the Rayleigh reflectance in the absence of aerosols, $\rho_a(\lambda)$ is the aerosol reflectance in the absence of Rayleigh Scattering, $\rho_{ra}(\lambda)$ is the reflectance component for photons that have been both Rayleigh and aerosol scattered, t_v is the diffuse transmittance from the sea surface to the sensor, and $[\rho_w(\lambda)]_N$ is the reflectance corresponding to $[L_w]_N$, the normalized water-leaving radiance: $[\rho_w(\lambda)]_N = \pi [L_w]_N / F_0$.

Figure 2.9 shows the variation of $[\rho_w(\lambda)]_N$ with pigment concentration (the pigment concentration is the sum of the concentrations of Chlorophyll-*a* plus phaeophytin *a*) at four wavelengths (λ = 443, 520, 550, and 670 nm) for Case 1 Waters (Gordon 1997). The red line on each panel indicates 0.001 on the scale. Generally see that the reflectance at 443 nm rapidly decreases with pigment concentration,

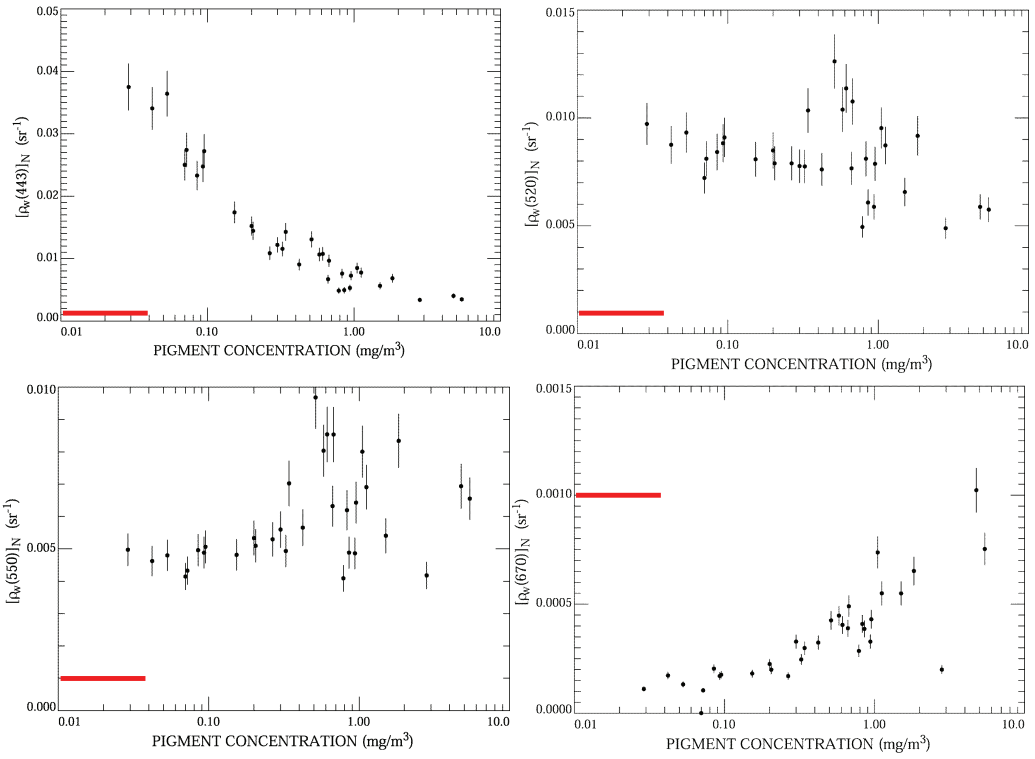

Figure 2.9 Dependence of $[\rho_w]_N$ on the pigment concentration for 443, 520, 555, and 670 nm. The red bar corresponds to a reflectance of 0.001. (From Gordon 1997).

and is only a weak function of the concentration in the green. These data are not corrected for instrumental self-shading, which is strongly dependent on absorption, so the reflectance at 670 nm is too low by roughly a factor of 1.5 to 2.

After considerable experience with the CZCS proof-of-concept mission, the originally announced goal for future ocean-colour sensors (SeaWiFS, MODIS, etc.) was that:

> *The uncertainty in the (normalized) water-leaving radiance retrieved from the sensor in oligotrophic waters at 443 nm should not exceed 5%, and uncertainty in Chlorophyll should be* ±30%.

For such waters, $[\rho_w(443)]_N$ is approximately 0.04 (Figure 2.9), meaning that the maximum error allowed is 0.002. The atmospheric correction algorithm was specifically designed to meet this goal. If we take the error in atmospheric correction to typically be of the order of 0.001 in reflectance at 443 nm, then since the TOA reflectance is ~ 0.20 under these conditions, meeting this goal would require the sensor have a calibration uncertainty no more than about 0.001/0.20 or ~ 0.5% at 443 nm. This is difficult to meet even under pre-launch conditions. (This implies that an in-orbit calibration or calibration adjustment is required: *vicarious calibration*).

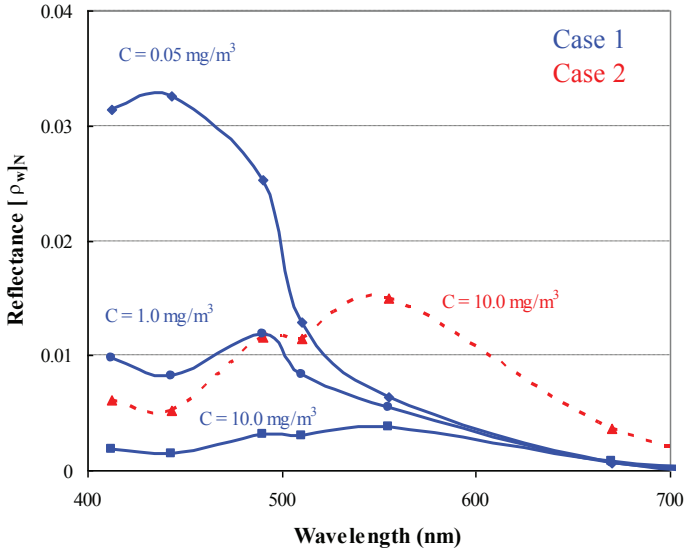

Figure 2.10 Examples of computed $[\rho_w]_N$ spectra for various chlorophyll concentrations for Case 1 and Case 2 waters.

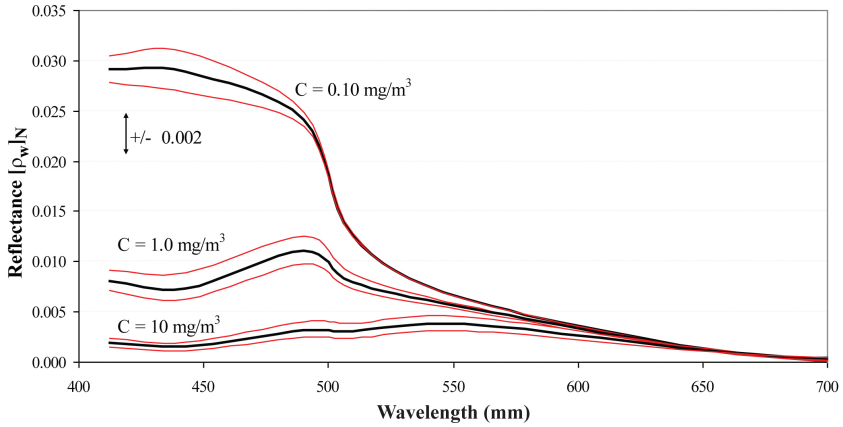

Figure 2.11 Examples of computed $[\rho_w]_N$ spectra for various chlorophyll concentrations. The red lines correspond to a ±30% change in C for Case 1 waters.

However, we can try to look at the radiometric calibration requirements in another way, i.e., using the *Chlorophyll-a* (C) requirement of 30% uncertainty. Figures 2.10 and 2.11 provide spectra of $[\rho_w(\lambda)]_N$ computed using the Garver-Siegel reflectance model (Garver and Siegel, 1997; Maritorena et al., 2002). They show that only in the low to moderate-C waters is an accuracy of ±0.002 sufficient in the blue, and that the shape of the spectra is as important, or more important, than the absolute reflectance. This is manifest in the "ratio algorithms" traditionally used in ocean colour (Clark, 1981; Gordon and Morel, 1983). Figure 2.12 (Gordon, 1997) provides measurements of the ratio $[\rho_w(443)]_N/[\rho_w 550)]_N$ taken from Figure 2.9. It shows

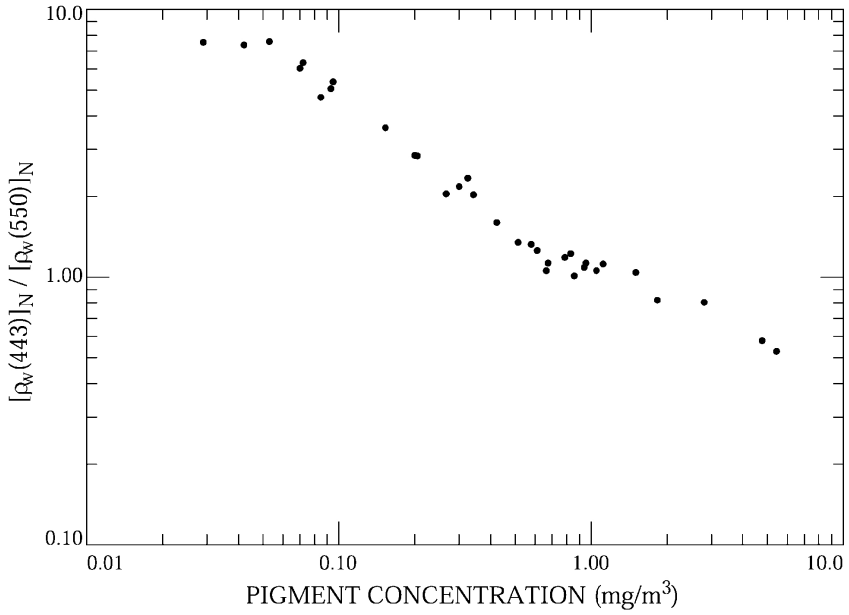

Figure 2.12 The reflectance ratio $[\rho_w(443)]_N/[\rho_w(550)]_N$ as a function of the pigment concentration from the data in Figure 2.9 (from Gordon, 1997.)

a clear relationship between the reflectance ratio and the pigment concentration. For these data,

$$C \cong \left(\frac{[\rho_w(550)]_N}{[\rho_w(443)]_N}\right)^{1.7}$$

so the relative error in C is (after dropping the cumbersome square bracket notation of $[\rho_w]_N$)

$$\frac{\delta C}{C} \cong 1.7 \times \left(\frac{\delta\rho_w(550)}{\rho_w(550)} - \frac{\delta\rho_w(443)}{\rho_w(443)}\right)$$

and if the $\delta\rho_w$'s are the direct result of calibration errors, we see again that the *impact on C* is minimized if the calibration error in the two bands is of the same sign! Similarly, for high C, Gordon *et al.* (1983) used

$$C \cong A\left(\frac{\rho_w(550)}{\rho_w(520}\right)^{2.5}$$

yielding

$$\frac{\delta C}{C} \cong 2.5 \times \left(\frac{\delta\rho_w(550)}{\rho_w(550)} - \frac{\delta\rho_w(520)}{\rho_w(520)}\right)$$

In the worst-case scenario, the errors at the two wavelengths are of opposite signs, and assuming the magnitude of the relative errors at the two wavelengths is identical, a 30% error in C requires

$$\frac{\delta\rho_w(443)}{\rho_w(443)} \cong 0.09$$

for the low-C algorithm. But

$$\frac{\rho_w(443)}{\rho_t(443)} \sim 0.12 \Rightarrow \frac{\delta\rho_t(443)}{\rho_t(443)} \sim 0.09 \times 0.12 \sim 0.011$$

$$\frac{\rho_w(550)}{\rho_t(550)} \sim 0.05 \Rightarrow \frac{\delta\rho_t(550)}{\rho_t(550)} \sim 0.09 \times 0.05 \sim 0.0045$$

Again, these calibration errors (~1% at 443 nm and 0.5% at 550 nm) are difficult to obtain even in a laboratory environment. In addition, note that for high C (~5 mg/m^3), where $\rho_w(443)$ is approximately 0.002 to 0.004, we find that $\rho_w(443)/\rho_t(443) \sim 0.012 - 0.024$ or $\delta\rho_t(443)/\rho_t(443) \sim 0.12 - 0.24\%$. Calibration to this accuracy is not possible at the present time.

The similar worst-case scenario using the 550 nm to 520 nm ratio algorithm for high C yields

$$\frac{\rho_w(520)}{\rho_t(520)} \sim 0.10 \Rightarrow \frac{\delta\rho_t(520)}{\rho_t(520)} \sim 0.06 \times 0.10 \sim 0.006$$

$$\frac{\rho_w(550)}{\rho_t(550)} \sim 0.05 \Rightarrow \frac{\delta\rho_t(550)}{\rho_t(550)} \sim 0.06 \times 0.05 \sim 0.003$$

In the best-case scenario, the errors in the individual bands have the same magnitude and the same sign. Then

$$\frac{\delta C}{C} \cong 1.7 \times \left(\frac{\delta\rho_w(550)}{\rho_w(550)} - \frac{\delta\rho_w(443)}{\rho_w(443)} \right) \sim 0$$

This can likely happen at low C, but for high C, ρ_w's are small in the blue (~ 0.001 to 0.002), so the $\delta\rho_w$'s must be correspondingly smaller. Reality is somewhere between the best and worst cases.

We have seen that the calibration accuracy requirements are extremely severe if there is no correlation between the ρ_w error in one band and the ρ_w error in other bands. The principal error in ρ_w results from atmospheric correction. The atmospheric correction algorithm has the property that under most conditions it will yield the desirable situation in which the error in ρ_w will be of similar sign in each spectral band when the exact TOA reflectances are provided. What if the input TOA reflectances contain error, i.e., calibration error? To investigate this, we assume that the estimated reflectance in a given band has a relative error α, i.e.,

$$\rho(\lambda)_{Est} = \rho(\lambda)_{True}[1 + \alpha(\lambda)],$$

and operate the algorithm to find the error in atmospheric correction in the blue induced by various values of α, in the blue and near infrared (NIR). The resulting error in

$$t_v(443)\rho_w(443)$$

is provided in Figure 2.13 (Gordon 1997).

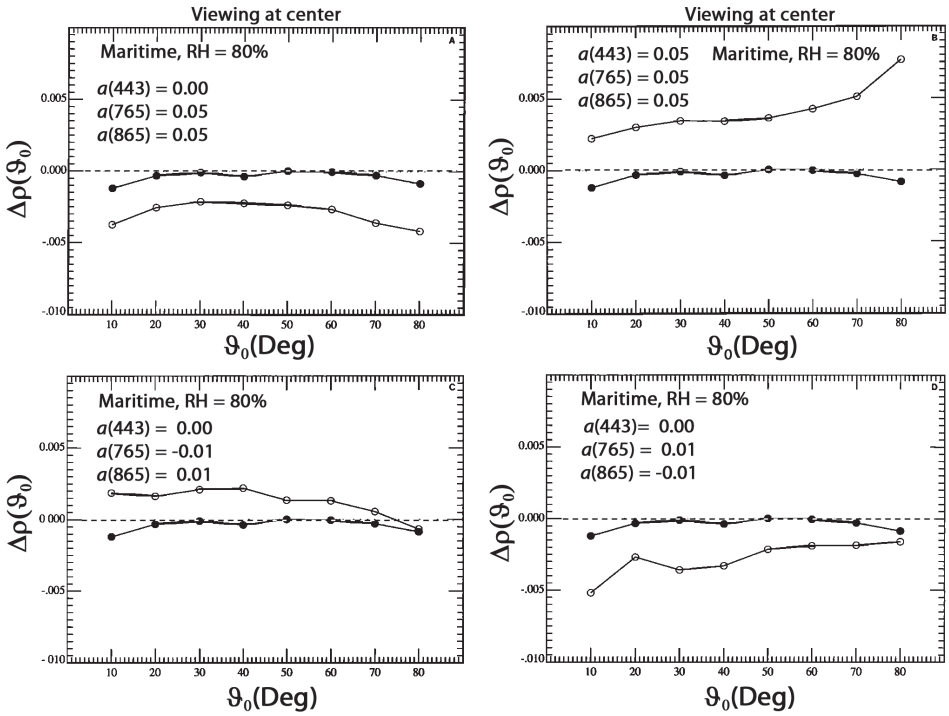

Figure 2.13 The error in the retrieved $t_v(443)\rho_w(443)$ for various calibration errors (from Gordon, 1997). In these simulations the aerosol optical depth at 685 nm was 0.2 and the Maritime model for a relative humidity of 80% was used to characterize the aerosol scattering.

These show that, in the NIR, small calibration errors of opposite sign are as important as large errors with the same sign, and when calibration errors are of the same sign in all bands, their effect is significantly reduced. In addition, Figure 2.13 shows that calibration error can void the tendency for the algorithm to cause errors of similar sign in all bands.

The following conclusions can be made regarding acceptable calibration errors:

- The 30% uncertainty in C can be met with this error as long as the error in the water-leaving radiances have the same sign in all spectral bands, but even then there will be difficulties at high C where $\rho_w(443) \sim 0.002 - 0.004$.
- To meet 5% uncertainty in $\rho_w(443)$ in oligotrophic waters, $\delta\rho_t(443)/\rho_t(443) \sim 0.5\%$. (The relative error in L_w in these waters in the blue is approximately 10 times the relative error in L_t.)
- The effect of calibration error on the error in atmospheric correction is also minimized when the calibration errors in all bands have the same sign.

It would seem that the calibration requirements of ocean-colour sensors are too stringent to be met by standard calibration techniques. However, they can be met to a certain extent by vicarious calibration techniques (Gordon 1987; Zhang and Gordon, 1997; Gordon 1998). We shall review these now.

2.6 Vicarious Calibration Concepts

The term *vicarious calibration* means an adjustment of the sensor's radiometric calibration coefficients, $k_L(\lambda)$ or $K_r(\lambda)$, based on radiometric (and possibly other) measurements made at the surface. There are two basic kinds of vicarious calibration: *radiometric and system*.

2.6.1 Radiometric vicarious calibration

In radiometric vicarious calibration, each term in the equation

$$\rho_t(\lambda) = \rho_r(\lambda) + \rho_A(\lambda) + t_v(\lambda)t_s(\lambda)[\rho_w(\lambda)]_N$$

for the TOA reflectance (Gordon and Wang, 1994) is estimated based on measurements made at the surface. This is accomplished as follows:

- $\rho_r(\lambda)$ is computed using the atmospheric pressure measured at the surface;
- $\rho_A(\lambda), t_v(\lambda)$, and $t_s(\lambda)$ are estimated using sun photometer and sky radiance measurements (to retrieve aerosol properties) made simultaneously with the sensor estimate of $\rho_t(\lambda)$; and
- $[\rho_w(\lambda)]_N$ is determined by *in-situ* measurements of the upwelling water-leaving radiance.

Given the estimate of $\rho_t(\lambda)$ based on these measurements, the calibration of the sensor is then adjusted so the sensor-estimated and the surface-estimated values of $\rho_t(\lambda)$ agree. The accuracy of such a calibration is limited by the accuracy of the surface measurements (Zhang and Gordon, 1997).

2.6.2 System vicarious calibration

By "system" we mean calibration of the *combined* sensor *and* the atmospheric correction algorithm. This is accomplished in the following manner (Gordon 1998):

- Assume the calibration in longest NIR band, i.e., 865 nm for SeaWiFS, is correct (e.g., for SeaWiFS, assume there is no calibration error at 865 nm).
- Adjust the calibration in second longest NIR band (765 nm for SeaWiFS) so that the spectral variation of ρ_A is consistent with the aerosol type actually measured at the calibration site, or typical of the calibration site.
- Apply atmospheric correction algorithm to ρ_t and adjust the calibration to force agreement between the retrieved and the measured values of $[\rho_w(\lambda)]_N$. (Note that the various ancillary data, e.g., Ozone absorption, etc., are also measured at the calibration site.)
- The first bullet can be avoided by applying radiometric vicarious calibration methods to longest NIR band.

System vicarious calibration has several advantages over radiometric vicarious calibration (Gordon, 1998):

- The residual calibration errors will all be of the same sign.
- The residual calibration errors will decrease from the NIR to the blue.
- The NIR error can be reduced/quantified by radiometric vicarious calibration. Reducing this error will concomitantly reduce the residual error in all shorter wave bands.
- Pragmatically, the sensor is being forced to do the job for which it was designed.

2.7 Concluding Remarks

We have tried to provide a brief introduction to the calibration of ocean-colour sensors. It is interesting to point out that, with a cursory glance at the requirements outlined in Section 2.5, one would naturally be led to conclude that the requirements for sensor calibration are so severe (beyond what is presently possible even in the laboratory) it would be impossible to derive useful information from ocean-colour observations beyond the "pretty pictures" that show patterns produced by currents, surface slicks, etc. Fortunately, because of the nature of the atmospheric correction algorithm, the in-water chlorophyll algorithms, and the concept of vicarious calibration, this conclusion is absolutely incorrect.

Chapter 3

Onboard Calibration Techniques and Devices

Steven Delwart, Robert Frouin, Robert E. Eplee, Gerhard Meister

3.1 Introduction

The quantitative relation between the responses (i.e., voltage, digital number) of the ocean-colour instrument to the input radiance it is intended to measure, are affected by the space environment (e.g., exposure to ultraviolet light and particles) and the normal aging process of optical parts, detectors, and electronics. The variables of prime consideration in the check-of-calibration process are the radiant amplitude and the spectral location. The spatial response, affected by scattering and crosstalk, should also be considered, but will not be discussed in this Chapter.

To monitor the radiometric gain or sensitivity in space, i.e., the slope of the relation between input and output signal, and the spectral response, several light sources are generally used. They are either internal, such as Tungsten lamps, or external, such as the Sun or the Moon. Zero radiation energy, used to determine the dark signal, is generally achieved by activating a shutter that blocks the Sun and Earth optical paths. Using space targets, unlike Earth targets, avoids atmospheric interference, which causes variation in the reflected energy observed from space. The Sun, a stable light source of well-known spectral irradiance, is the ultimate calibration standard. In this Chapter, the techniques and systems used for on-orbit calibration of ocean-colour sensors are described.

3.2 Lamp Calibration

Tungsten lamps are commonly used as internal light sources. They have low energy requirements, and their emission spectra are precise. In essence, the laboratory standard calibration is monitored for change by reference to the internal lamp. The lamp output generally decreases with time, i.e., only changes in the sensitivity of the instrument can be observed. In other words, the internal lamp calibration is relative in nature. Traceability and repeatability with time are checked, but not traceability to a known source.

The lamp source radiation is typically collected and imaged at the entrance

aperture by a transfer system, often after reflection by transmission through a diffuser. Variable density filters, with transmission continuously varying from one end to the other (e.g., from 100% to a few %), can be swept across the optical path to change the input radiance at the entrance aperture. Superposing lamps also allow for different radiance levels. In general, redundant lamps are used, and some are activated less frequently. In some systems, the radiance from the source is monitored by photodiodes, which may be placed at different locations along the optical path. This allows a check-of-stability of the source. Comparing the signals from the monitoring photodiodes and from the instrument detectors provides information about changes in the transmission of the calibration optics.

Calibration subsystems with internal lamps of light-emitting diodes for a relative check have been incorporated in several ocean-colour instruments, especially early ones, for example CZCS, MOS, OCTS, GLI, and OCM. The principle of internal calibration is illustrated in Figure 3.1, which depicts schematically the assembly contained in MOS.

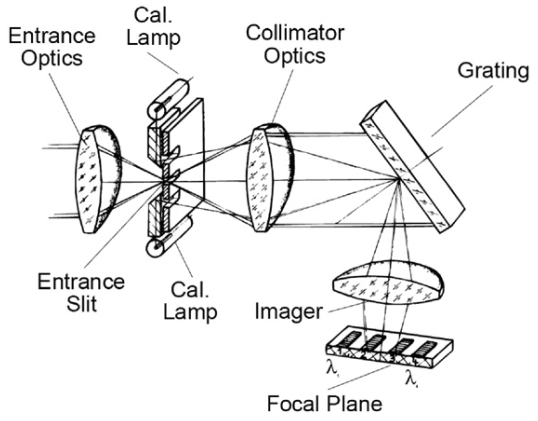

Figure 3.1 Principle of the Modular Optoelectronic Scanner (MOS) internal calibration (after Zimmermann and Neumann, 2000.)

Two small filament lamps, mounted besides the entrance slit, illuminate the collimator optics via auxiliary slits. By powering the lamps to 4 highly stabilized current levels, 16 different illumination intensities were generated for each spectral band of the instrument. Using this calibration assembly, significant changes in the sensitivity of MOS-B onboard IRS-P3 were detected during April to December 1996, i.e., during the first months after launch (Neumann, 2001). They reached about 3% in bands 2 (444 nm) and 10 (869 nm) (Figure 3.2). The gain for band 2 became fairly stable after that period, but the gain for band 10 continued to increase, reaching 6% in June 1999 (Figure 3.2). To give another example, the results obtained by Yoshida et al. (2004) for GLI onboard ADEOS-2 are displayed in Figure 3.3, including the relative output of the monitoring photodiode. They show a degradation of the instrument responsivity (inverse of gain) with time in all the spectral bands

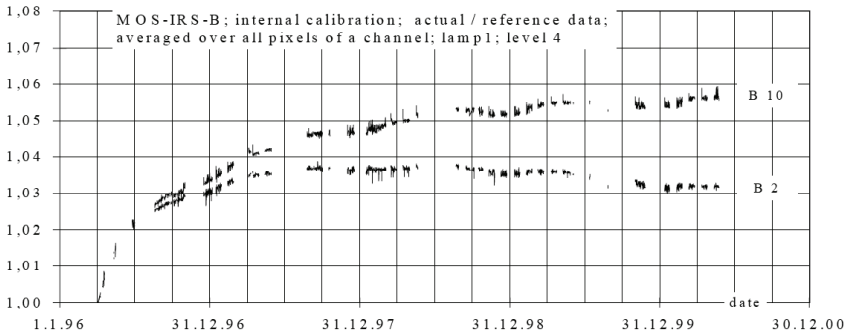

Figure 3.2 Change in the gain of the Modular Optoelectronic Scanner (MOS) in spectral bands 2 and 10 during the period from April 1996 to December 2000, as determined by internal lamp calibration (after Neumann, 2001.)

in the ultraviolet, visible, and near infrared, reaching 3% at the end of the sensor life in November 2003. The diode output also decreased with time, to about 2% in November 2003.

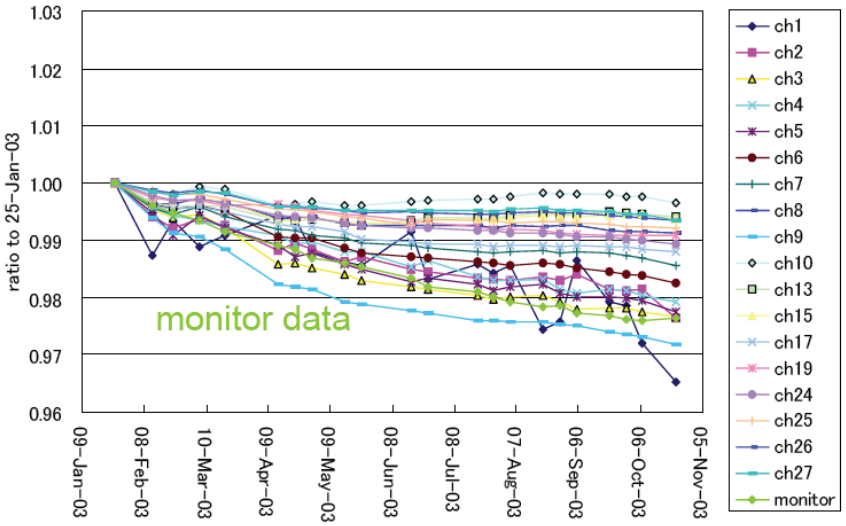

Figure 3.3 Change in the responsivity (inverse of gain) of the Global Imager (GLI) spectral bands in the ultraviolet, visible, and near infrared, scan mirror B, from January to November 2003, as determined by internal lamp calibration (after Yoshida et al., 2004.)

Internal calibrators thus allow monitoring and, to some extent, quantification of the sensor parameters with respect to a reference, for example pre-launch calibration or initial post-launch calibration. They allow a check of linearity in sensor response, and they may be selected for specific spectral characteristics. However, they do not necessarily cover the entire field of view, depending on construction. Long-term stability is a major problem. Furthermore, their spectral distribution may

differ substantially from the solar spectrum, which may introduce uncertainties when out-of-band response is significant. Relying solely on internal light sources to calibrate ocean-colour sensors operating in orbit, which was the case for CZCS, is definitely insufficient. Lunar calibration, by orienting the spacecraft for moon viewing, provides an effective way to monitor sensor degradation after launch (see Section 3.3 below). Complementary onboard techniques, such as solar calibration (Section 3.4), are necessary to know the absolute magnitude of the measured radiance in fundamental units.

3.3 Lunar Calibration

3.3.1 Method description

All historic and current space-borne ocean-colour sensors have experienced change (degradation) over time, e.g., by about 50% for the MODIS 412 nm bands on both the Terra and Aqua spacecrafts (Franz et al., 2008). Degradation trending of radiometric sensitivity, therefore, is a major aspect of on-orbit sensor calibration and characterization activities. Instead of using internal lamps (Section 3.2), radiometric sensor degradation can be determined by measuring the sunlight reflected off the Moon throughout the mission in regular intervals, e.g., monthly. The ocean-colour community recognizes that lunar measurements have a superior track record (e.g. IOCCG, 2012). The main advantages of using the Moon for calibration are that lunar observations are made without any atmospheric contamination and the lunar reflectance is constant over geological time scales (Kieffer, 1997), surpassing any reasonable radiometric precision requirements.

Although the lunar reflectance is constant, the lunar irradiance as seen from Earth, or from an Earth-orbiting spacecraft, varies considerably, even for a constant lunar phase angle (a lunar phase angle of 0° corresponds to full moon, 90° to new moon; note that the irradiance from a new moon is essentially 0). This is illustrated in Figure 3.4, which displays the Moon irradiance measured by SeaWiFS, in terms of normalized radiance, during the first 10 years of the mission. The variations are predictable and depend mainly on the Moon-Sun and Earth-Moon distances, and on libration (slight variations of the orientation of the Moon relative to the Earth). The ROLO (Robotic Lunar Observatory, U.S. Geological Survey) model predicts these variations. The ROLO model has been derived from a multi-year measurement campaign of lunar irradiance using an Earth-based radiometer (Kieffer and Stone, 2005).

Each detector in the radiometer must acquire an image of the entire moon to enable tying the radiance measurements to the ROLO spectral irradiance model (the ROLO model only provides the irradiance for the entire moon). This prevents certain radiometer types (e.g., a push-broom scanner like MERIS) from using the Moon as a calibration source. Over-sampling, however, may occur. SeaWiFS, for example,

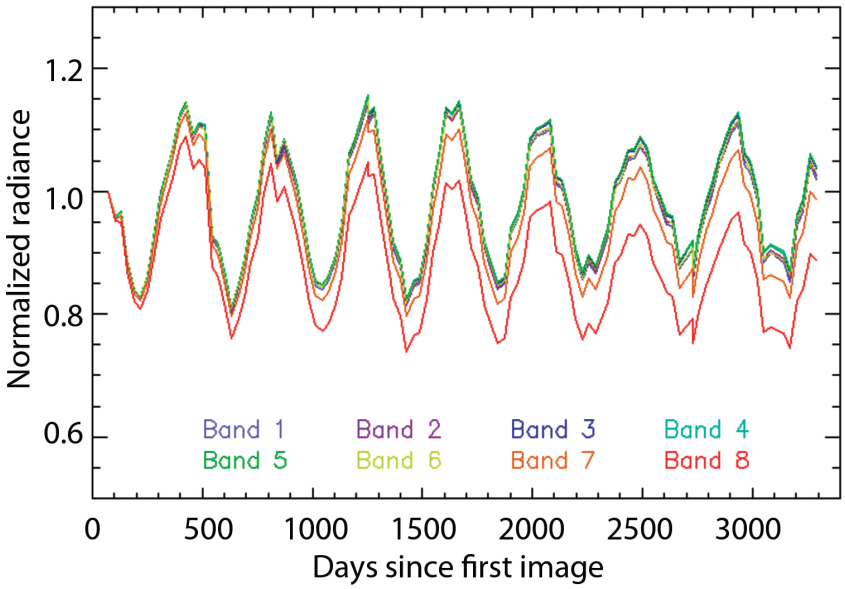

Figure 3.4 Lunar irradiance as measured by SeaWiFS, plotted as radiance normalized to 1 for all bands at the first measurement (first 10 years of data). The data are dominated by the true variations of the lunar irradiance, even though the lunar phase angle is almost constant (about 7°) for each measurement.

over-sampled the Moon in track direction, i.e., the Moon appeared elongated in track direction relative to scan direction (see Figure 3.5), leading to an increase in apparent irradiance. This effect can be corrected (Barnes et al., 2004), as opposed to under-sampling, where information is lost.

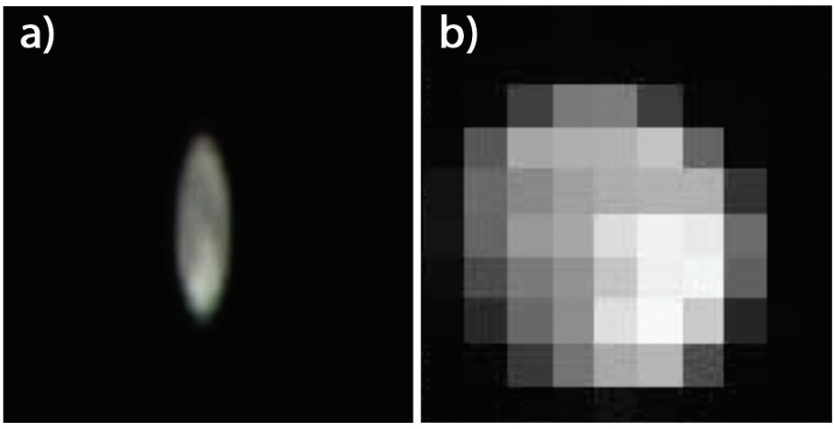

Figure 3.5 a) The moon (at 7° phase angle) as seen in several scan lines by SeaWiFS on 14 November 1997. The track direction (vertical) is elongated because of over-sampling. b) The Moon (at 55° phase angle) as seen in one scan line by the MODIS-Aqua 412 nm band (1-km nominal spatial resolution). In this case, seven detectors scanned across the Moon horizontally. Image credit SeaWiFS Project - NASA GSFC.

For any ocean-colour sensor viewing the Moon, the lunar calibration time series takes the form (Eplee et al., 2004):

$$\begin{aligned} A(t,\lambda) = & [L_{obs}(t,\lambda,\alpha,\gamma,l_{sc},b_{sc},l_{sun},b_{sun})/L_{obs}(t_0,\lambda,\alpha,\gamma,l_{sc},b_{sc},l_{sun},b_{sun})] \\ & f_1(t)f_2(t,\alpha,\gamma)f_3(l,\alpha)f_4(l_{sc},b_{sc},l_{sun},b_{sun})f_5(t,\lambda) \end{aligned} \tag{3.1}$$

where A is the relative calibration coefficient (time and spectral band dependent), L_{obs} is the integrated radiance observed at time t, f_1, f_2, f_3, f_4 and f_5 are correction factors for distance, over-sampling, phase angle, libration, and noise, respectively, and t_i is the reference time to anchor the relative calibration (e.g., the time of the first lunar calibration). These factors depend on t (f_1, f_2, f_3, and f_5), the phase angle, α(f_2 and f_3), the track angle γ(f_2), and the latitude and longitude of the sub-spacecraft point, l_{sc} and b_{sc}, and the latitude and longitude of the sub-solar point, l_{sun} and b_{sun}(f_4).

Compared to lamp calibrations (Section 3.2) and solar diffuser calibrations (Section 3.4), the main advantages of lunar calibrations are:

- long term stability of the source (no degradation of lamp or diffuser),
- instruments on different spacecrafts can view the Moon (without simultaneity requirement), allowing cross-calibration even without temporal overlap of the missions (Eplee et al., 2011)
- no requirement for pre-launch characterization (lamps and solar diffuser BRDF need to be characterized before launch),
- no additional cost during instrument built, and
- no on-orbit mechanism (on MODIS-Terra, the solar diffuser door failed, see Franz et al., 2008).

The main disadvantages are:

- a spacecraft manoeuvre is generally required,
- typically only one to two opportunities exist per month (up to one opportunity per orbit for solar diffuser calibrations, more for lamp calibrations),
- a photometric model of the Moon (e.g., ROLO) is required, and
- the lunar image is typically acquired only at one scan angle (some, but not all, solar diffuser or lamp calibration approaches cover all scan angles).

3.3.2 Challenges

Using the Moon as a calibration source requires addressing satisfactorily a number of challenging issues. These include taking into account lunar intensity variations, selecting optimum phase angle and calibration frequency, and performing spacecraft manoeuvres.

3.3.2.1 Lunar irradiance variations

Lunar irradiance measured from an earth-orbiting sensor depends strongly on several factors, such as the instrument-Moon distance, the Moon-Sun distance, libration, and lunar phase angle (see Figure 3.4). The ROLO model captures these variations. Therefore, lunar irradiance variations are a manageable issue. However, it should be noted that the availability of the ROLO model to non-U.S. missions should not be taken for granted due to export control restrictions imposed on U.S. agencies. For example, in the case of the OCM-2 sensor on Oceansat-2 (ISRO), a significant administrative effort was required for the delivery of lunar irradiances calculated with ROLO to ISRO.

3.3.2.2 Spatial reflectance variations

Lunar reflectance has strong spatial variation, as evidenced by the dark marias and bright highlands that are readily visible to human observers. For a typical Earth-observing sensor with 1-km resolution, these brightness variations are resolved in the acquired image, as shown in Figure 3.5a and b. The ROLO model provides only the disk-integrated lunar irradiance (i.e., the sum of radiances over all lunar pixels); it cannot provide the radiance for individual pixels. Although a lunar radiance model for individual pixels is under development, the expected precision is at best about 5.0% for individual measurements and 0.5% for long-term precision (T. Stone, private communication). This is an issue for sensors like MODIS, because these sensors measure the lunar image with multiple detectors. MODIS uses up to 10 detectors for its 1-km resolution bands. Only one calibration factor per band and mirror side is derived for the operational MODIS calibration. Note that MODIS uses lunar measurements only as a detector-independent adjustment to the scan angle dependence of the radiometric sensitivity (Sun et al., 2007), and secondly, it is possible to derive one calibration factor per detector for the MODIS 1-km bands, but the uncertainties are much larger (Sun et al., 2007). To summarize, the spatial reflectance variations of the lunar surface severely complicate the calibration effort, unless each sensor element (e.g., each detector) that needs to be calibrated acquires a complete image of the lunar disk to allow a comparison with the irradiance provided by the ROLO model. SeaWiFS fulfilled this condition.

3.3.2.3 Calibration frequency

Lunar irradiance varies strongly with phase angle. To optimize the long-term trending precision, phase angle should be kept constant, which means that lunar calibration measurements could be performed only once every lunar month (29.5 days). If measurements are scheduled at the same absolute value of phase angle before and after full moon, two lunar calibrations per month are possible, leading to a potential increase in precision. This would be especially helpful at the beginning of

the mission (trending precision is usually worst at the beginning and end of a time series). Although the interval of once or twice a month is sufficient for long-term trending, a separate calibration mechanism (e.g. a solar diffuser) is needed to resolve short-term variations of radiometric sensitivity of the sensor.

3.3.2.4 Optimum phase angle

The choice of phase angle involves at least two considerations. The first consideration is that the larger the phase angle, the fewer the useful (sunlit) lunar pixels are available for the irradiance calculation. Therefore, a larger phase angle is expected to decrease the precision of the irradiance measured by the sensor, although this has not been quantified. The second consideration is that at very small phase angles, lunar backscatter decreases the accuracy of the ROLO model (the opposition effect, Stone et al., 2004). For SeaWiFS, a phase angle of 7° was chosen, leading to excellent results (note that SeaWiFS was used to validate the ROLO model, see Barnes et al., 2004). The ROLO model uncertainty of 1% for each measurement is valid for phase angles larger than 7°, but the ROLO model uncertainty for long-term measurements of 0.1% has only been demonstrated for the SeaWiFS phase angle. Preferably, the phase angle should be always at either waxing or waning Moon (no preference for either one) to avoid switching phase angle between calibrations. For different target phase angles, long-term precision implications must be analyzed. Note that lunar phase increases by about 0.85° per orbit, so in any lunar month, an Earth-orbiting sensor may miss the optimal phase angle by up to 0.85°/2. Limiting the range of phase angles to 6.5° to 7.5°, for example, will allow one measurement in this range per lunar month (or two for both the waxing and waning Moon).

3.3.2.5 Lunar calibration manoeuvres

The type of spacecraft manoeuvre that will be performed has implications for the optimum lunar phase angle. Low phase angles, such as were observed by SeaWiFS, require a back flip of the satellite so that the instrument observes the Moon near nadir. Intermediate phase angles (50° to 58°) can be observed by a roll of the spacecraft, as is done by MODIS on the Terra and Aqua spacecrafts and by VIIRS on Suomi NPP. For either type of manoeuver, the timing of the calibration can be optimized within the spacecraft operational constraints to maintain the phase angle of the lunar observations to within one degree, over the mission.

3.3.3 Uncertainty

The uncertainty related to phase angle dominates the relative uncertainty of the ROLO model. By acquiring lunar measurements over a small range of phase angles, the uncertainty related to phase angle can be effectively eliminated, and a long-term trending precision of 0.1% can be achieved (Stone and Kieffer, 2004).

Increasing the frequency of lunar measurements is expected to increase the precision of the trending of radiometric degradation of the sensor (but not necessarily the accuracy). The amount of this increase is speculative at the moment. The SeaWiFS precision was achieved with only one measurement per month. Possible advantages of additional phase angles have to be weighed against the increased resources needed to obtain the additional measurements (e.g. the power needed to manoeuver the instrument into a position where it can see the Moon). An obvious choice for increasing the number of lunar measurements beyond a single measurement would be to calibrate at both 7° before and after full Moon, as discussed above.

Note that lunar irradiances provided by the ROLO model are known to contain a relatively large bias (about 5-10%, see Stone and Kieffer, 2004). Nevertheless, the precision of the lunar irradiance provided by the ROLO model is excellent. Therefore, lunar measurements are ideal (depending on instrument type, see above) for relative temporal gain trending, but not the first choice for absolute calibration accuracy. At the time of this writing, efforts are in the early planning stages at NIST (National Institute of Standards and Technology, Gaithersburg, USA) to develop a lunar measurement campaign that may allow significant improvement in the absolute accuracy of the ROLO model.

3.3.4 Application example

Lunar calibration was the primary calibration approach for SeaWiFS. The radiometric gain trends after all corrections (but before fitting to an analytical function in time) are shown in Figure 3.6. The long-term stability that has been achieved with this methodology for the SeaWiFS mission lifetime is on the order of 0.1% (Eplee et al., 2011). The MODIS sensors on the Terra and Aqua spacecrafts have used lunar calibrations as secondary calibration approaches (to monitor the scan angle dependence of the radiometric degradation; a solar diffuser acts as the primary calibration source (see Sun et al., 2007). For the recently launched VIIRS sensor on Suomi NPP, the current operational calibration uses the solar diffuser measurements only. It is expected that in the near future, lunar calibration will be used as the primary calibration approach for VIIRS ocean-colour products produced by NASA (Eplee et al., 2012).

3.4 Solar Calibration

3.4.1 Method description

It is generally accepted that reflectance-based radiometric calibration of optical sensors in the visible and near-infrared spectral domain using the Sun as light source provides the best absolute radiometric accuracy for space-borne radiometers (Slater

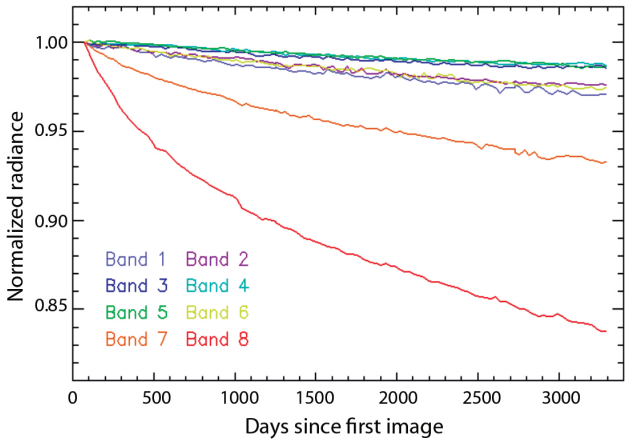

Figure 3.6 Same data as in Figure 3.4 after correcting for the true variability of the lunar irradiance as calculated by the ROLO model (and after correction for over-sampling, an effect on the order of about 1% for SeaWiFS).

et al., 1995; see also Section 2.3). The extraterrestrial solar irradiance illuminating the calibration plaques is very well known and very stable in the visible and near infrared, and the solar diffuser plaque can be considered as an embarked secondary reflectance standard, traceable to standard laboratories, such as NIST (USA), NPL (UK) or PTB (Germany). Solar diffusers have been used in the majority of the heritage ocean-colour missions, such as SeaWiFS, MOS, GLI, OCM, MODIS, and MERIS as well as in recent and future missions such as GOCI, VIIRS, and OLCI.

Carefully designed solar diffuser-based calibration hardware can allow for full pupil and full optical path radiometric calibration for scanning radiometers such as SeaWiFS and MODIS, and for full pupil, full optical path, and full field of view radiometric calibration for push-broom instruments such as MERIS (Figure 3.7). It can be used over the complete solar reflective spectral domain ranging from the ultra violet to the short wave infrared.

During radiometric calibration, the solar diffuser is illuminated by a solar flux proportional to the square of the distance between the Sun and the Earth leading to a yearly variation of ±1% in irradiance. The resulting calibration radiance field, after correction of the Sun-Earth distance, will vary spectrally and spatially according to the Bidirectional Reflectance Distribution Function (BRDF) behavior of the diffuser plaque (e.g., Nicodemus et al., 1977). We have:

$$L = F_0 r_P \cos(\theta_0)/(\pi a^2) \tag{3.2}$$

where L is the input radiance, F_0 is the Sun irradiance, r_p the bidirectional reflectance of the plaque, θ_0 is the Sun zenith angle, and a is the Earth-Sun distance. During the calibration process, the above terms need to be applied to compute the radiance L, and the instrument radiometric equation must include all instrument specific

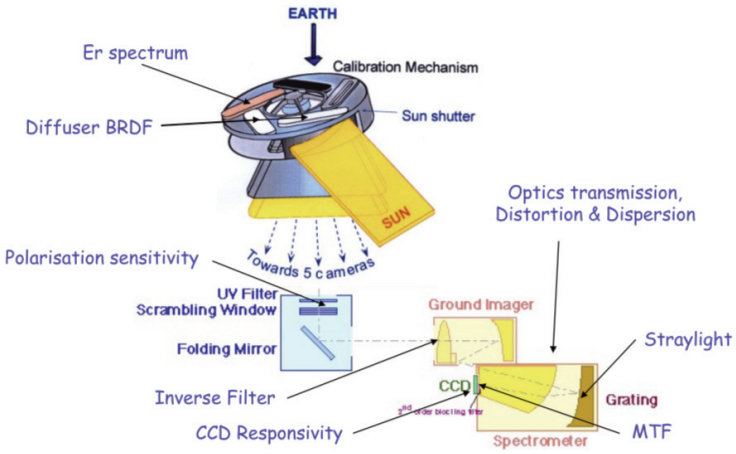

Figure 3.7 Diagram of the MERIS onboard calibration hardware.

corrections such as: non-linearity, time delay integration, smearing, polarization, stray light, scan mirror position etc., before determining the end-to-end instrument "gains" (counts to radiance conversion factors) per pixel and per band, from which the instrument's degradation model - also known as radiometric trending - can be derived. For MERIS, the radiometric model that relates measured radiance to digital count can be written as (e.g., MERIS Team, 2011):

$$X_{b,k,m,t} = NL_{b,m}\{(g(T_t^{VEU})[A_{b,k,m}(L_{b,k,m,t} + G_{b,k,m}(L_{*,*,*,t})) + Sm_{b,k,m,t}(L_{b,k,m,*})] + g_c(T_t^{CCD})C^0_{b,k,m}\} \tag{3.3}$$

where subscripts b, k, m, and t denote the spectral band, the spatial pixel, the camera, and the acquisition time, respectively, subscript $*$ stands for multiple values up to the entire range of the subscript it replaces, $X_{b,k,m,t}$ is the MERIS raw sample (numerical count), NL is a non-linear function, T is the temperature of the amplifiers, and T^{CCD} is temperature of the detectors, g and g_c are (dimensionless temperature correction functions, G is a linear operator representing the stray light contribution to the signal, A is the "absolute radiometric gain", S is the smear signal, due to continuous sensing of light, and C^0 is the calibrated dark signal (depends on band and gain settings).

The uncertainty associated with the Sun-Earth distance is minimal as it is known with great accuracy. The solar flux in the visible, near infrared and shortwave infrared domain have been demonstrated to be very stable and the spectral irradiance level is well known (Thuillier et al., 2003). Furthermore, the space-craft's orbit and attitude are generally very well known allowing for precise computation of the calibration geometry, leaving the lion's share of the uncertainty of reflectance-based calibration to the knowledge of the BRDF of the calibration plaque, and the spectral response function of the detectors (see Section 3.4.5).

During the yearly orbital cycle of helio-synchronous orbits, the solar illumination angle on the plaque during calibration can be timed in such a way as to occur at fixed solar elevation angles on the plaque. However, the illumination azimuth angle will vary by up to 15 degrees if no dedicated yaw manoeuvres are performed to correct for the variation. This change in illumination geometry on real diffusers, which are not perfect Lambertian scatterers, can have a significant impact on the calibration radiance level (up to ±3%), in particular for low solar elevation geometries as used in MERIS (Delwart and Bourg, 2009). In the case of MODIS, the seasonal change in illumination geometry leads to a variation (after correction using characterization results from a yaw manoeuver) of the measured gain factors of about ±0.5% (Meister et al., 2008). An improved angular dependence of the transmission of the solar diffuser screen has recently been derived (Wang et al., 2011), but has not yet been implemented into the operational processing.

An in-depth analysis of the diffusion characteristics of a volume scattering diffuser such as Spectralon has shown (Bruegge et al., 2001) that in order to provide well behaved "Lambertian" BRDF characteristics, it was necessary to keep the solar illumination of the plaque at elevation angles > 45 degrees (the closer the illumination to grazing incidences, the more pronounced the asymmetry in the scattering lobe, in both view azimuth and elevation). Nevertheless, in order to have a calibration signal level close to what is commonly found in ocean-colour missions, the design choice is frequently to select a white diffuser and a low solar illumination angle, i.e., MERIS, or include a sieve attenuator, e.g., MODIS (Waluschka et al., 2004) or VIIRS, which will introduce azimuthally-dependent calibration signal levels. A grey diffuser (see Section 3.4. for more details of diffuser types), when qualified for space use, will allow for higher illumination angles. This should provide a BRDF much less sensitive to the Sun's azimuth annual cycle, at optimum radiance levels, and hence could ensure a more consistent absolute radiometric accuracy across the field of view of large swath pushbroom instrument such as MERIS and OLCI.

It should be noted, that vicarious calibration can only bring a single scaling factor per band (for the complete field of view) approximately every year, due to the difficulty of gathering sufficient amounts of high quality *in-situ* data to determine this system level correction. For both push-broom and scanning instruments, the final system level accuracy of the absolute radiometric calibration across the instrument's field of view will always include the systematic errors of the BRDF model used during calibration for MERIS (Delwart and Bourg, 2009), and the response versus scan (Chen et al., 2011) and polarization corrections errors for MODIS.

Diffusers, at least for the most commonly used material, Spectralon^{tm}, have been shown to age (browning) after exposure to solar radiation, mainly ultraviolet radiation (Siegman et al., 1993; Petroy et al., 1994; Leland and Arrechi, 1995; Chommeloux et al., 1998). A strategy to correct for this aging is necessary to achieve the radiometric accuracy required by ocean-colour missions over their lifetime. Different methods have been employed historically, i.e., MODIS and GOCI use a solar

diffuser stability monitor (Chen and Xiong, 2009; Kang et al., 2010), while MERIS uses a second, less frequently exposed, diffuser plaque to measure the relative aging of the regularly used plaque (Rast et al., 1999). Calibration methodology using the Moon as a reflectance standard (Kieffer and Stone, 2005) have also been used for radiometric trending as well as the evaluation of the aging of the diffusers for both SeaWiFS and MODIS. This this is discussed in Section 3.3.

After accounting for all the factors above comprehensively (i.e., the Sun-Earth distance, solar elevation being identical, the plaque's BRDF, and the diffuser aging), the end-to-end instrument detector gain degradation with time can be determined, trended, and included in the Level-1 processing (Xiong et al., 2007; Delwart and Bourg, 2011). Note that due to an inability to monitor the solar diffuser reflectance change on-orbit independently, the SeaWiFS solar diffuser was used to verify short-term stability, but was ultimately not used to calculate the on-orbit gains (Eplee et al., 2007).

Instruments with a rotating telescope (e.g., SeaWiFS, MODIS, and VIIRS) typically acquire the solar diffuser signal only for a very limited range of angles. In the case of MODIS, the scan-angle mirror reflectance degradation has an angular dependency (Xiong et al., 2007). Therefore, the solar diffuser calibration is not sufficient for a determination of the gain at all scan angles. Initially, lunar calibrations were used to support the on-orbit gain determination. However, especially for the shorter wavelengths (400 nm – 500 nm), additional, scan-angle dependent corrections (not derived from the solar diffuser measurements) are required to produce ocean-colour products (Kwiatkowska et al., 2008; Meister et al., 2012). In the case of SeaWiFS, it was determined that the scan angle dependency of the gains did not change on-orbit, and therefore a calibration source at a single scan angle (e.g., using a solar diffuser) would be adequate (but was ultimately not used, see above).

3.4.2 Characterizing diffuser plaques on the ground

The scattering characteristics of a diffuser plaque can be very well measured in the laboratory. However, great care is needed in the acceptance of the characterization bench before starting a characterization campaign, as these are very costly and lengthy efforts (Datla et al., 2009). The characterization method to be used has to be tailored to the application, i.e., large plaques, position of entrance pupil on the plaque, large viewing angle range, spectral domain, etc., to restrict the measurements to the lowest number of degrees of freedom possible, while being as close as possible to the optical conditions expected during calibration on-orbit.

A number of facilities exist today where such measurements are performed (Figure 3.8), and the techniques have been improving continuously. For more details on the method used, see Feng et al. (1993), Shiff et al. (1993), Smorenburg et al. (1995), Proctor and Barnes (1996), Barnes et al. (1998), and Yoon et al. (2009). Round-robin activities have been performed across laboratories, and have shown

that, in general, an agreement to better than 1% can be achieved over a large spectral and geometrical domain (Early et al., 2000; Butler et al., 2003).

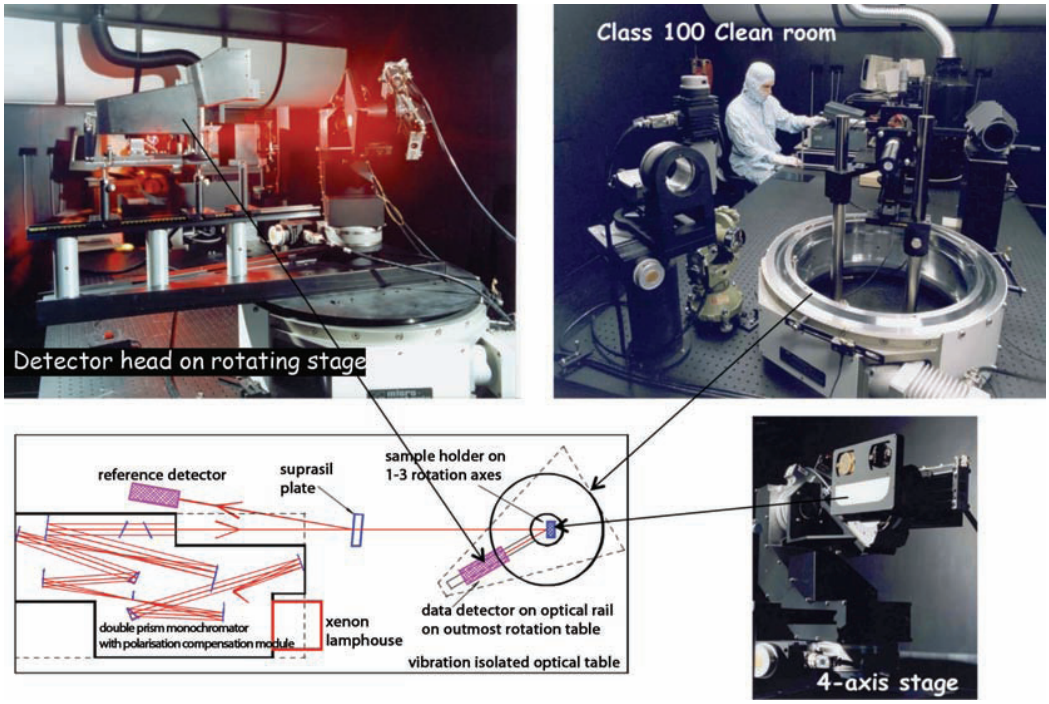

Figure 3.8 TPD-TNO characterization facility in the Netherlands used for MERIS calibration measurements of the bidirectional reflection function (BRDF).

3.4.3 Modelling the BRDF of diffuser plaques

To exploit the BRDF characterization data, one needs to fit a BRDF model before applying it during calibration. This is necessary in order to cover the complete spectral and geometrical domain of interest in a consistent way. A simple model can be used when the geometrical domain is small, such as for scanning instruments, however, it becomes critical when used for the calibration of large field of view push-broom instruments.

Attempts have been made for MISR (Flasse et al., 1993; Bruegge et al., 2001) and for MERIS (Courréges-Lacoste et al., 2003; Delwart and Bourg, 2009). These models have their limitations, however, and the residual error introduced by the model cannot be corrected for by the system level vicarious calibration, even if this system-level correction will compensate on average for its shortcomings.

3.4.4 Characterizing the instrument on the ground

The instrument radiometric response can be measured on the ground with an integrating sphere (IS) to an accuracy sufficient to determine the instrument's saturation level ±5% (or better). Such measurements establish a radiometric baseline for a "transfer to orbit"' experiment — a comparison of the instrument's gains as measured with on-ground and onboard methods, i.e., IS versus Sun illuminated diffuser plaque, as performed for example by SeaWiFS (Barnes and Zalewski, 2003a; 2003b). Attempts have been made to illuminate the diffuser plaque on-ground with a solar simulator (i.e., for MERIS). However, due to relatively small size and non-uniformity of the solar simulator illuminating spot (not covering the diffuser plaque uniformly) the analysis of these results was limited to a relative verification of the diffuser's BRDF characteristics and associated BRDF model.

The transfer to orbit exercise will have limitations due to the difference in the illumination signal on the plaque on-orbit with the Sun at approximately 6000-K, while sources commonly used on-ground, whether in the integrating sphere or in a solar simulator, will only have a brightness temperature of approximately 3000-K. This will lead to significantly different signal levels across the spectral domain (colour), resulting in different sensor responses even if only a small amount of integrated out-of-band response is present. Further, the Fraunhofer absorption lines present in the solar spectrum are not present in the output of a tungsten lamp, and for sensors with band-passes of 10 nm, this can affect the response by up to a few percent.

SeaWiFS was taken out of the laboratory, and the solar diffuser illuminated directly by the Sun (Barnes and Zalewski, 2003b). This provided a uniform illumination with the appropriate spectrum, and although this method allows a substantial reduction of the difference in the illumination signal between on-ground and on-orbit, it is still significantly affected by atmospheric scattering (Rayleigh and Mie) and atmospheric absorption (by water vapor, ozone, and oxygen), which needs to be carefully corrected for before determining the instrument's absolute radiometric response. In the end, the uncertainties associated with such a method can reach levels similar to those available in laboratories (although it is extremely risky from a contamination point of view), reducing the main usefulness of such an experiment to only verifying the impact of the out-of-band response of filter-based scanning radiometers such as MODIS and SeaWiFS.

3.4.5 Diffusers types

A number of diffuser types have been used historically as on-orbit reflectance secondary standards, such as white thermal control paint YB71 panels (SeaWiFS), de-polished aluminium (OMI, SCIAMACHY, GOME), de-polished quartz quasi volume diffusers (OMI, GOMES-2), and Russian Opal tiles (Clarke, 1998) (ATSR series). Space

grade Spectralon^{tm} by Labsphere, Inc., however, is by far the most commonly used reflectance standard in space applications to date (Brueggge et al., 1993), and is used for MODIS, MERIS, VIIRS, etc.

Spectralon is made from sintered polytetrafluoroethylene (PTFE - or Teflon) pellets according to a proprietary method developed by Labsphere, Inc. (see Chang et al., 2007 for high power applications). Labsphere also produces "doped" diffusers, which can include rare Earth elements (i.e., Erbium), and provide spectral features used in spectral calibration (see Section 3.5), and black pigments (proprietary) used in grey scale diffusers. Grey scale diffusers (Georgiev and Butler, 2008) have not flown on space missions to date, but hopefully they will be used in the future. For more on Spectralon, see http://www.labsphere.com/products/reflectance-materials-and-coatings/default.aspx. Note that other companies also make sintered space grade PTFE diffusers such as SphereOptics, which will be used for the MERIS follow-on OLCI, and Fluorion diffusers from Altran technologies with no past or planned space experience.

The mechanical characteristics of Spectralon are suitable (Tsai et al., 2008), i.e., the material is sufficiently stiff to keep the stringent flatness requirements, and sufficiently supple to sustain the vibration loads of a launch into orbit. As PTFE is a dielectric, it is important to provide an adequate grounding within the calibration mechanism to prevent charges from accumulating and producing arching. Great care must be taken in the manufacturing of space-grade Spectralon due to contamination, from the selection of the original PTFE pellets to the milling and shaving post-manufacturing process. Contaminants, mainly organics, are known to produce both photoluminescence, and degradation of the plaque reflective properties in the ultraviolet to blue-green regions when exposed to solar radiation (Petroy et al., 1994; Leland and Arrechi, 1995). In order to mitigate these effects, a post-manufacturing cleaning process must be applied (Chommeloux et al., 1998) to minimize the level of contaminants remaining.

It must be noted, that in order to keep the plaque's reflectance as stable as was achieved on MERIS (<2% at 412 nm and <1% above 490 nm after ten year on-orbit, Delwart and Bourg, 2011), great care must be taken regarding cleanliness. The diffusers need to be kept at Class 100 standards cleanliness throughout the diffuser characterization campaign, shipping, integration, and testing phase of the instrument, up to on-orbit. The plaques have to be followed by cleanliness witnesses until they are integrated on the instrument, and then kept in a positive pressure of clean dry nitrogen, which requires a purge to be continuously applied until the launcher fairings are closed, and the count down begins. Note that such periods can last for many years! Finally, on-orbit the calibration mechanism should be such as to protect the diffuser from solar radiation while the diffuser is not deployed for calibration. For the MERIS diffuser (deployed every 200 orbits), the accumulated duration of solar illumination, at 30° elevation, was less than 7 hours after ten years (50,000 orbits) of operations. The aging of Spectralon at these levels of illumination

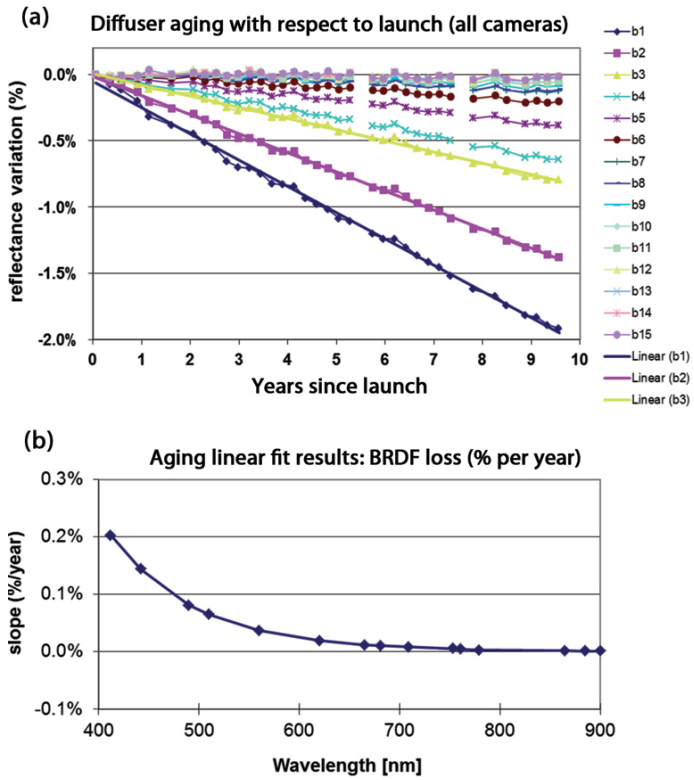

Figure 3.9 (a) Relative evolution of diffusers response ratio. (b) Diffuser aging rate for MERIS channels, in percent per year.

behaves in a very linear manner (Figure 3.9), allowing determination of the foreseen aging of the Spectralon plaque for different instrument designs.

3.4.6 Speckle in diffuser-based calibration

Speckle is an optical interference pattern created when partially coherent radiation is scattered from a large number of "secondary emitters" as found on rough surfaces (Dainty, 1975). Solar diffusers are chosen for their good scattering characteristics and hence will introduce speckling in the calibration radiation field, the amplitude of which will increase with increasing wavelength, i.e., coherence for a fixed bandwidth. Such effects have been measured on MERIS, and can reach up to a few tenths of a percent in the near infrared for a 10 nm bandwidth.

Note that although this effect is quite small, it will nevertheless introduce observable across-track striping in the data products of push-broom instruments if not corrected for, e.g., using image equalization methods. Speckling is only a minor problem for scanning telescope radiometers like MODIS or SeaWiFS, because the solar diffuser signal for these instruments is acquired and averaged over a certain angular range (forty 1-km frames in the case of MODIS), which smoothes out the

speckling effect.

Speckle in diffuser based calibration of spectrometers has been investigated in depth (van Brug and Courréges-Lacoste, 2007), and has shown to be much more pronounced in surface rather than in volume scattering materials. Furthermore, speckle also affects atmospheric chemistry profiling spectrometers in the spectral dimension (i.e., spectral features), while push-broom radiometers will be primarily affected by spatial speckle, creating across-track striping. Care must also be taken regarding speckle during the definition of the BRDF characterization bench (Georgiev and Butler, 2005), particularly when using coherent illumination, such as tunable lasers or diodes, so as to minimize the errors associated with speckle during the characterization campaign.

3.4.7 Polarization characteristics of diffusers

At the interface between any two materials, an electromagnetic field will be transmitted and reflected differently according to the polarization of the incident ray and the geometry. This will polarize the light reflected or transmitted from this interface, e.g., as for a Brewster polarization plate. Hence, one expects that the solar diffuser also polarizes the un-polarized radiation illuminating it from the Sun, and will introduce errors in the calibration method if not properly accounted for, in particular for instruments with intrinsic polarizing characteristics i.e., that do not include a polarization scrambler. The use of polarization scramblers as in SeaWiFS and MERIS reduces the instrument's sensitivity to polarization during calibration and observation to roughly the level of the radiometric noise, and no polarization correction needs to be applied for such designs.

Note that the s-polarization, for a 30° elevation illumination angle, scatters more than the p-polarization in MERIS view geometries, suggesting a stronger volume scattering for s-polarization than p, with a marked increase in the scattering lobe as one gets closer to the specular direction. Classically, the p-polarized incident light is preferentially transmitted into the material, with less light reflected in the forward direction. Therefore, the p-polarized irradiance will contribute most efficiently to the multiple scattering, which is depolarizing (Haner et al., 1999). This behavior further reinforces the need to illuminate the Spectralon solar diffuser at a high elevation angle, not only to have a better behaved and more Lambertian scattering lobe, but also for the calibration signal to be as un-polarized as possible, in particular for instrument designs with intrinsic polarizing characteristics.

3.4.8 Application example: MERIS on-orbit calibration

For MERIS, the absolute calibration coefficients (inverse gain), $A_{b,k,m}$ (see Equation 3.3), are computed as follows:

$$A_{b,k,m,t} = L_{b,k,m,t} / X'_{b.k,m,t} \tag{3.4}$$

where $X'_{b.k,m,t} = NL^{-1}(X_{b.k,m,t}) - C^0_{b,k,m} - Sm_{b,k,m,t}$ is the calibration count corrected for non-linearity, dark offset and smear. The stray light contribution is computed and added to the calibration radiance before use. This process includes an iterative loop: as the stray light contribution is estimated from the corrupted signal, the corrected signal allows the derivation of a better estimate of the stray light contribution that in turn allows the computation of a better corrected signal. Iterations are stopped when the improvement ceases to be significant.

Exposure of the instrument to the space environment implies aging of its components, including diffuser plates and optics. If degradation of the sensor itself is inherently part of the instrument response, and as such must be accounted for in the $A_{b,k,m,t}$ computation, aging of the diffuser plate impacts the estimation of the radiance at instrument entrance. It is thus necessary to monitor and quantify this aging independently, and this was accomplished for MERIS using a second diffuser plate deployed much less frequently.

Two approaches are possible to handle the variation of the instrument response with time. The first one is to frequently update the calibration coefficients, and the second one is to model their evolution in time. The second option (trending) was selected for MERIS.

3.4.8.1 Dark offset

In nominal operations, dark offset is measured during every radiometric calibration. One thousand frames acquired and averaged on-board are transmitted to ground stations along with the radiometric measurements, allowing offset correction coefficients to be derived as well as long-term stability to be monitor.

OCL-ON dark offset, i.e. dark offset obtained with the on-board Offset Control Loop (OCL) enabled, proved to be extremely stable over the mission as shown in Figure 3.10 for band 1 and the smear band (all observation bands behave similarly to band 1). Long-term stability is better than 0.04 counts at ADC output for all observation bands and lower than 0.16 counts for the smear band.

Analysis of the OCL-ON temporal behavior of dark offset shows that there is temporal stability with no trends. Such behaviour justifies the use of a temporal average to build the dark offset correction coefficient table per pixel. In conclusion, in OCL-ON mode, the MERIS dark offset is extremely stable to better than a tenth of a bit of a twelve bit word.

3.4.8.2 Radiometric gain

In nominal operations, the radiometric gain is measured during every radiometric calibration, i.e., every two weeks. 500 frames are acquired during solar illumination

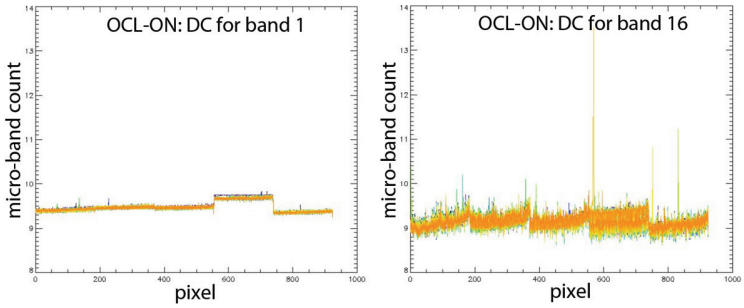

Figure 3.10 Dark calibration measurements as a function of spatial pixel for all orbits in OCL-ON setting for band 1 (left) and smear band (right), scaled to micro-band level. 215 orbits are plotted on top of each other.

and averaged on-board before transmission to the ground, where the radiometric gains are derived and long-term stability monitored.

The gain measurements show an instrument degradation of 5% max (B1, Cam5) for the whole duration of the mission, and cameras 1, 3 and 4 show seasonal variations in their gains, due to the limitation of the diffuser's BRDF model in azimuth. Different strategies have been employed to mitigate these BRDF model limitations (Delwart and Bourg, 2011), normalizing to the near infrared band gains assumed constant during the early years of the mission, and using all measured gains once the data availability is such that the degradation trend results are not biased by azimuth effects.

3.4.8.3 Optics degradation model

Optics are known to degrade exponentially when exposed to a space environment (Barnes et al., 2001). These authors developed a degradation model for SeaWiFS that was also selected for MERIS (see Equation below). Starting from a reference value $G(t_0)$, the gain evolution with time is given by:

$$G(t) = G(t_0)[1 - b(1 - ge^{-dt})] \tag{3.5}$$

where t is time, t_0 a time of reference, b can be considered as the maximum degradation, d as the time scale of the exponential, and g as a time offset. The degradation model fit is estimated to be better than 0.1% RMS. The same estimator applied to the diffuser-2 validation data set restricted to the same time period is even better. It is assumed that this improvement is due to better quality of the BRDF model for diffuser-2. The degradation model derived using the complete calibration data set, was compared to the gains measured within a limited azimuth range (0.2 degrees centered around 27.3 degrees). This methodology of comparing the modelled degradation with raw degradation measurements at close to constant Sun azimuth angles is used to estimate the performance of the model for all pixels of

bands 1 and 15 (412 and 900 nm respectively) for all the calibration orbits satisfying the Sun azimuth constraint over the time period used for the fit. Results indicate that the ratios remain within 1 ± 0.001 for both bands.

In summary, the instrument's throughput has only suffered a limited level of degradation (max 5% at 412nm in only one camera, after 9 years on-orbit), and this degradation was very well captured by regular radiometric calibration measurements combined with a trending model including both the diffuser aging and the instrument sensitivity degradation. Note also that the MERIS radiometric scale based on the on-board calibration diffuser plates has been validated against a number of vicarious calibration methods and shown to be well within the estimated performance of <4%.

3.4.9 Uncertainty

The error budget of the solar calibration, leaving aside the uncertainty on the solar irradiance, is mainly driven by the accuracy of the characterization of the diffuser plates and its modelling, the instrument spectral model, and to a lesser degree, by the modelling errors of the diffuser aging, and by instrument degradation. Using well-protected, and therefore very stable, onboard diffuser plates as secondary standards, and monitoring the aging of the dedicated calibration plate by a second, less frequently exposed "identical" plate (in the case of MERIS), allows for the correction of the diffuser aging during the radiometric gain trending, to an accuracy of better than 0.2%. This makes it possible to reach an overall model error budget of <2%, as established for MERIS.

Uncertainty associated with knowledge of the solar irradiance contributes to the final error budget for the absolute calibration coefficients. Various solar observations have been merged and determined to have an error of ±1% (Neckel and Labs, 1984; Thuillier et al., 2003). Taking into account this error, the absolute radiometric calibration, radiance-based, can be performed with an overall uncertainty as low as ±3% (see also Krause et al., 2002).

It is important to emphasize, however, that ocean-colour remote sensing deals with normalized radiance or reflectance, i.e., the magnitude of the solar irradiance is not required, even though the basic ocean-colour product generated by satellite ocean-colour projects is water-leaving radiance. Bio-optical algorithms and inversion schemes to retrieve marine properties generally use remote-sensing reflectance (e.g., IOCCG, 2006). A reflectance-based calibration, however, requires that the solar flux should be constant between the time of the onboard calibration and the time of the ocean measurements. This is the case: the solar constant changes by only 0.2% over a 22-year solar cycle (see Barnes and Zalewski, 2003a). In view of the above, onboard reflectance calibration using the Sun and diffusers should be achievable with an overall uncertainty of ±2%, and this should be considered as the goal for the on-orbit, purely radiometric, absolute reflectance calibration of ocean-colour

sensors.

3.5 Spectral Calibration

Knowledge of an optical instrument's spectral characteristics is essential for determining radiometric response. The spectral radiance of the illumination source needs to be integrated over the instrument's line-shape response to quantify the amount of energy measured, noting that it will be different in calibration (e.g., solar spectrum) than in observation, which will be dominated by Rayleigh scattering in the atmosphere, especially at the ocean-colour wavelengths. Denoted as S_i, the instrument's spectral response, the measured radiance is given by (see Section 2.4):

$$\langle L(\lambda) \rangle \equiv \frac{\int L(\lambda) S_i(\lambda) d\lambda}{\int S_i(\lambda) d\lambda} \tag{3.6}$$

To convert the measured radiance to reflectance, both during observation and reflectance based calibration, the in-band solar irradiance can be computed by replacing $L(\lambda)$ in the above equation by irradiance $F_0(\lambda)$ (remembering to account for the varying Earth-Sun distance).

Instruments using multi-layer spectral filters need to have the response function of the "optical system" (filter, dichroic mirrors, etc.) measured precisely on the ground, over a large spectral domain, not only to determine the filter's "in-band" response, but also to quantify the amount of "out-of-band" signal the design allows through. The instrument's overall spectral response will be the product of the spectral characteristics of all optical elements involved in the optical path of each band, which may be different for each band, such as in scanning radiometers like MODIS.

A good estimate of the instrument's spectral response can be achieved by combining the spectral characteristics of all optical elements measured at component level. It is, however, crucial to measure the instrument end-to-end spectral response on the ground, with the instrument fully integrated: (1) to verify that the effective instrument spectral response is actually the product of all the elements' individual spectral responses; and (2) to quantify the amount of stray signal, i.e., stray light and out-of-band spectral response the instrument has, in order to "accept" the instrument (i.e., to determine whether it performs within the required/specified levels) and, as a minimum, to account for the stray signals in the processing, either as a correction term, or as an uncertainty.

Historically, multi-layer filters have not been very stable in the space environment, mainly due to water vapour absorbed in the coating while on the ground. This water vapour will evaporate in orbit, changing the physical dimensions of the coating layers, and will therefore introduce a spectral shift in the filter response. Modern filters, on the other hand, have shown negligible degradation over time, as revealed

on-orbit for MODIS from its spectral calibration device (Guenther et al., 1996). This is discussed in Section 3.5.1 below.

For imaging spectrometers such as MERIS, on the other hand, one needs to develop spectral models of the spectrometers (cameras) making up the instrument's field of view. A band generally consists of a number of spectral samples, i.e., charge-coupled device (CCD) "lines", and the band's overall spectral response is the sum of the spectral response of each "spectral-pixel = line" making up that band. The models should provide the spectral response of all CCD detector elements or, as a minimum, those involved in the operational band settings, to allow for computation of the spectral response for each pixel across the instrument field of view (MERIS=3700 pixels) and for all bands (MERIS=15). For more details, see Section 3.5.6.

3.5.1 Monochromators

Spectral calibration may be accomplished using onboard monochromators. These optical devices take a broadband light source and single out a specific narrow-band region of the electromagnetic spectrum. They have been used operationally for tracking on-orbit variations in MODIS spectral characteristics.

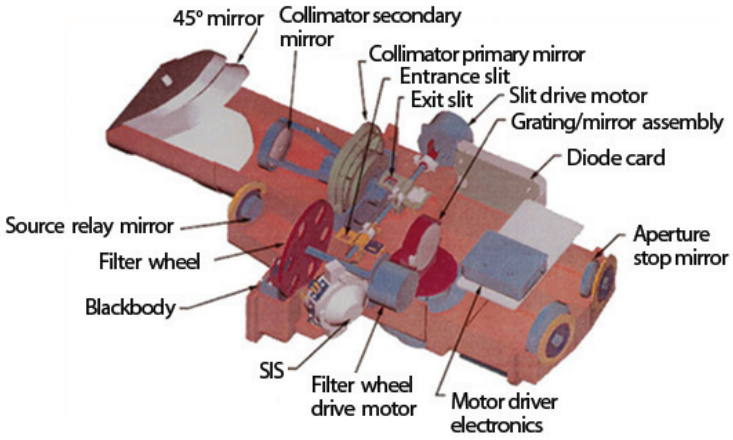

Figure 3.11 MODIS Spectroradiometric Calibration Assembly (SRCA) (credit NASA).

The MODIS onboard Spectro-Radiometric Calibration Assembly (SRCA) is an instrument by itself (Figure 3.11). It is capable of performing multiple functions. By slightly changing its configuration, the SRCA can be operated in three modes: radiometric, spatial, and spectral (Montgomery et al., 2000). When the SRCA is operated in spectral mode, it is configured as a monochromator with light sources and a collimator. When it is in radiometric or spatial mode, a plain mirror replaces the grating and the monochromator becomes an optical relay. The SRCA is also capable of performing wavelength self-calibration using stable and well-calibrated

spectral peaks of the didymium filter and a pair of reference detectors.

On the ground, the SRCA was characterized in a thermal vacuum (TV) chamber at both sensor and spacecraft levels before launch. The SRCA was operated on-orbit before the MODIS nadir door was opened. Two months after the MODIS-Terra nadir door was opened, the SRCA commenced normal spectral mode operations. A similar approach was used for MODIS-Aqua. The SRCA is routinely operated in the spectral mode every three months. The SRCA on-orbit performance is very stable.

The transfer to orbit of the spectral characterization was achieved by running the onboard SRCA on the ground in the spectral mode at nearly the same time as measuring the spectral characteristics and comparing the results (Xiong et al., 2006). It can be reasonably assumed that any bias is unchanged from pre-launch to on-orbit. With its internal wavelength self-calibration capability, the SRCA can be used to track the MODIS spectral performance from pre-launch to on-orbit and throughout its life.

Pre-launch tests demonstrated that use of ion-assisted deposition (IAD) filters greatly reduced band response shifts from the ambient to TV environments for the bands in the visible and near infrared. However, the on-orbit instrument temperature could still induce wavelengths shifts. The averaged temperature coefficient was measured to be 0.011 nm/K pre-launch and 0.008 nm/K on-orbit. Although these temperature coefficients measured pre-launch and on-orbit are both very small, the on-orbit results showed more variation. These thermal variations appear to be related to the bandwidth. Compared to the temporal changes, however, the impact of instrument temperature change is minor.

It has been observed that the recovered relative spectral response (RSR) profiles are fairly stable. Small changes have been detected for some bands, particularly in band 8 (0.412 μm) at its shorter wavelength sub-peak. Considering all the difficulties and challenges involved in the spectral characterization, such as wavelength calibration, reference transfer, changes in the on-orbit operational environment, and temperature and electronics configuration, the MODIS SRCA has been functioning well, providing useful information on the sensor's spectral performance.

The MODIS-Terra central wavelengths have shifted slightly since the pre-launch characterization toward shorter wavelengths during the first 1.5 years of on-orbit operation, for most of the bands, and have remained relatively stable since then (Xiong et al., 2006). With the exception of band 8, the central wavelength shifts for all the Terra MODIS bands in the visible and near infrared are less than 0.5 nm. If the initial changes from pre-launch to shortly after launch are ignored, the on-orbit shifts over the last five years have been within 0.2 nm on average. It seems that using IAD technology stabilizes the band central wavelengths. For MODIS-Aqua, the shifts in central wavelengths are also less than 0.5 nm, but for all bands, and the changes in bandwidth are also less than 0.5 nm, except for band 8 (-0.8 nm, Xiong et al., 2012).

3.5.2 Erbium-doped diffuser

The MERIS on-board calibration mechanism includes an Erbium-doped Spectralon^{TM} diffuser plate dedicated to spectral characterization, which offers a number of spectral absorption features (Figure 3.12) in the visible/near infrared spectral range. The absorption peaks selected for MERIS are those centred at 408 nm (Peak 1) and 522 nm (Peak 3).

Spectral calibration using an Erbium-doped solar diffuser plate is performed in two steps. On the first orbit, the instrument is configured to have 15 adjacent bands at the highest spectral sampling interval (1.25 nm in MERIS) centered on a spectral feature (Peak 1 or 3) and a radiometric calibration sequence is performed by deploying the frequently used "white" diffuser. On the following orbit, keeping the same spectral calibration band settings, the "pink" Erbium-doped diffuser is deployed during the calibration sequence. On the ground, the "spectral calibration pixels" are radiometrically calibrated using the "white" diffuser calibration signal, and when this calibration is applied to the measurement of the "pink" diffuser, it will show the Erbium spectral feature. To determine the position on the detector element of the CCD array of the peak of the Erbium absorption feature, a shape-matching algorithm is employed, comparing the Erbium measurements to a high resolution spectrum of Erbium, convolved with the spectral line shape of the pixels (2 nm).

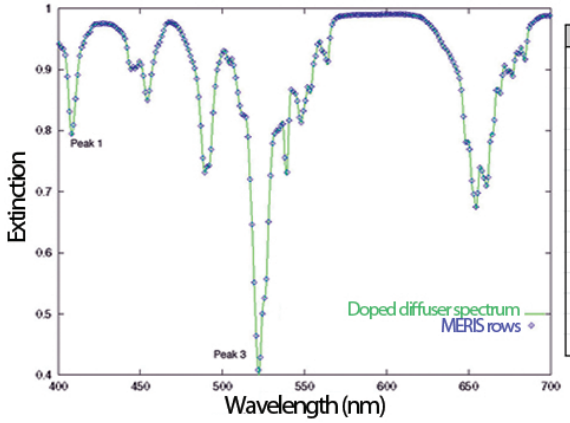

centre	width (nm)	centre	width (nm)
400.625	1.25	514.375	1.25
401.875	1.25	515.625	1.25
403.125	1.25	516.875	1.25
404.375	1.25	518.125	1.25
405.625	1.25	519.375	1.25
406.875	1.25	520.625	1.25
408.125	1.25	521.875	1.25
409.375	1.25	523.125	1.25
410.625	1.25	524.375	1.25
411.875	1.25	525.625	1.25
413.125	1.25	526.875	1.25
414.375	1.25	528.125	1.25
415.625	1.25	529.375	1.25
416.875	1.25	530.625	1.25
418.125	1.25	531.875	1.25

Figure 3.12 Erbium-doped Spectralon^{TM} diffuser reflection spectrum and instrument spectral band configuration.

Although these measurements have shown to be very useful to monitor the health of the instrument and determine the spectral stability of the instrument through regular measurements (every three months), the accuracy of the absolute wavelength derived from this method (estimated to be ± 0.3 nm) is not as good as those from the other methods. This is probably due to the width and shape of the absorption feature (Peak 3 is a doublet), and clearly not due to the weakness of the spectral signal.

3.5.3 Oxygen A-band

The absorption feature of atmospheric oxygen A-band (Figure 3.13) can be used for spectral calibration of spectrally programmable imaging spectrometers such as MERIS. This requires using complex algorithms, such as pressure minimization technique (Dubuisson et al., 2003, the LISE method), or neural network (Delwart et al., 2007, the FUB method), both based on radiative transfer computations to localize the spectral feature on the CCD array. The results are remarkably reproducible from one orbit to the other, and both methods yield very similar results. For spectral calibration, bright desert targets have been selected for MERIS. The method accuracy was estimated to be better than 0.2 nm (Delwart et al., 2007).

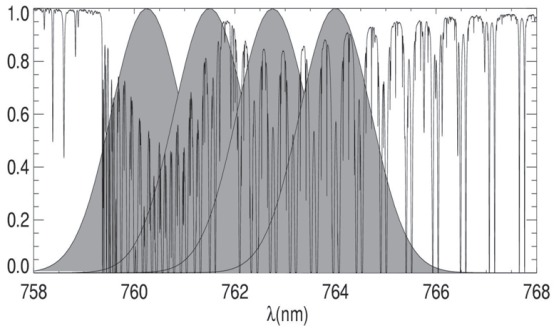

name	centre	width (nm)
blue-2	442.5	10
red-1	665	10
ref-1	753.125	6.25
O2-0	758.125	1.25
O2-1	759.375	1.25
O2-2	760.625	1.25
O2-3	761.875	1.25
O2-4	763.125	1.25
O2-5	764.375	1.25
O2-6	765.625	1.25
O2-7	766.875	1.25
O2-8	768.125	1.25
O2-9	769.375	1.25
ref-2	778.75	7.5
IR-1	865	10

Figure 3.13 Oxygen A-band absorption spectrum and instrument spectral band configuration for spectral calibration.

3.5.4 Fraunhofer lines

The solar Fraunhofer absorption lines in the solar spectrum can also be used for spectral calibration of spectrally programmable imaging spectrometers, using the solar diffuser (Delwart et al., 2004). The processing is performed using raw data, as radiometric calibration would remove the spectral signature inherent to the solar illumination. Figure 3.14 shows the Fraunhofer absorption features for four lines as well as the spectral band settings used for MERIS. To acquire the six selected Fraunhofer absorption features requires three orbits with each of two different band settings (i.e. Lines 1 and 4, 2 and 5, 3 and 6).

For the 396 nm absorption line, the spectral calibration results are well defined, mainly due the strength of the absorption feature. On the other hand, the results for the 854 nm absorption lines are much noisier, yet still reflect the spectral signature of the instrument rather well. This Fraunhofer line is kept in the processing due to its spectral position near the near infrared end of the spectral range. The quality of the method for the 588 nm and 866 nm lines, however, was considered inadequate, and results obtained using those lines were not used. Selection of the Fraunhofer lines for the instrument model (see Section 3.5.6) was made based on their coherence

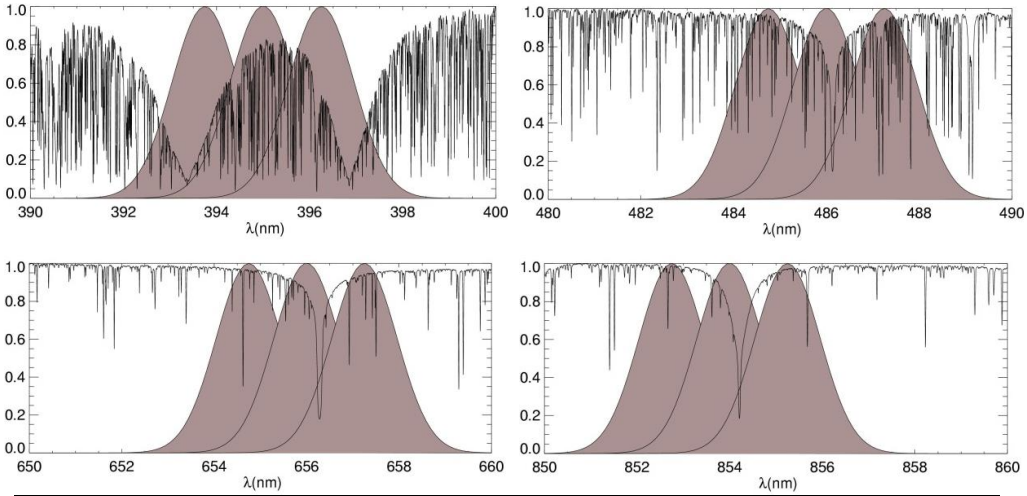

Line 1 (393 nm)	Line 2 (485 nm)	Line 3 (588 nm)	Line 4 (655 nm)	line 5 (855 nm)	Line 6 (867 nm)
394.375	483.125	584.375	653.125	850.625	863.125
395.625	484.375	585.625	654.375	851.875	864.375
396.875	485.625	586.875	655.625	853.125	865.625
398.125	486.875	588.125	656.875	854.375	866.875
399.375	488.125	589.375	658.125	855.625	868.125
400.625	489.375	590.625	659.375	856.875	869.375
401.875	490.625	591.875	660.625	858.125	870.625
403.125	491.875	593.125			

Figure 3.14 Top: Fraunhofer spectrum with typical MERIS detector normalised spectral response function overlay; for lines 1, 2 4 and 5 (from left to right). Bottom: Instrument band configuration for Fraunhofer spectral calibration of MERIS.

with each other.

3.5.5 Spectral model for imaging spectrometers

Imaging spectrometers need an instrument spectral model (dispersion law) to compute the in-band solar irradiance illuminating the calibration plaque during calibration, or the Earth during observation (Figure 3.15 for MERIS). As expected from the MERIS optical design, the measurements confirmed a very linear dispersion across the spectrum with a residual deviation $<\pm$ 0.3 nm with regards to a linear best fit.

From these measurements, a relatively simple and robust model could be derived for each MERIS camera, considering separately a mean dispersion law and an across-track deviation term.

$$\lambda(k,l) = <\lambda>(l) + \Delta\lambda(k), \tag{3.7}$$

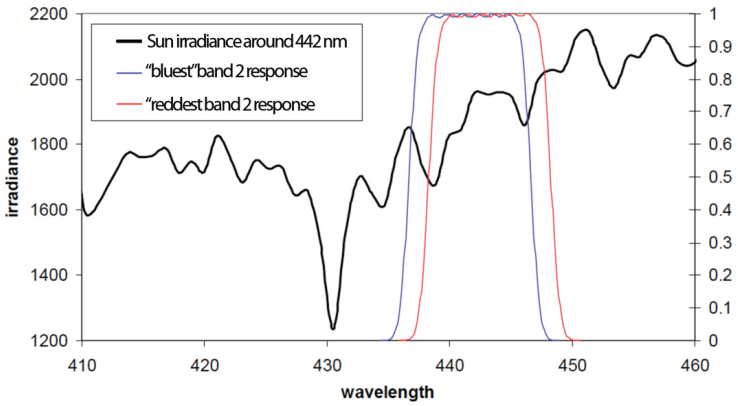

Figure 3.15 Reference solar irradiance around 440 nm and the extreme spectral response functions of MERIS band 2 (for pixel 740 of camera 1 and pixel 1 of camera 2 as "bluest" and "reddest", respectively).

where k and l stand for the spatial and spectral co-ordinates of a given detector, respectively, $<\lambda>(l)$, the mean dispersion law (mainly linear), is a polynomial of order 3 (best fit), and $\Delta\lambda(k)$, the across-track variation term, is a linear fit of the data at 395, 656 and 762 nm expressed relative to its mean value.

This simple equation defines the wavelength $<\lambda>(l)$ for the central pixel (370) of the CCD array, and the smile $\Delta\lambda(k)$ is accounted for with a linear spectral offset as a function of position in the field of view. The residual error from the spectral calibration with respect to the spectral model shows a RMS accuracy of the order of ± 0.1 nm, which could be improved with a more stringent selection of the calibration data, and a more elaborate model, in particular at the edge of each camera's field of view, where distortion is known to be more significant.

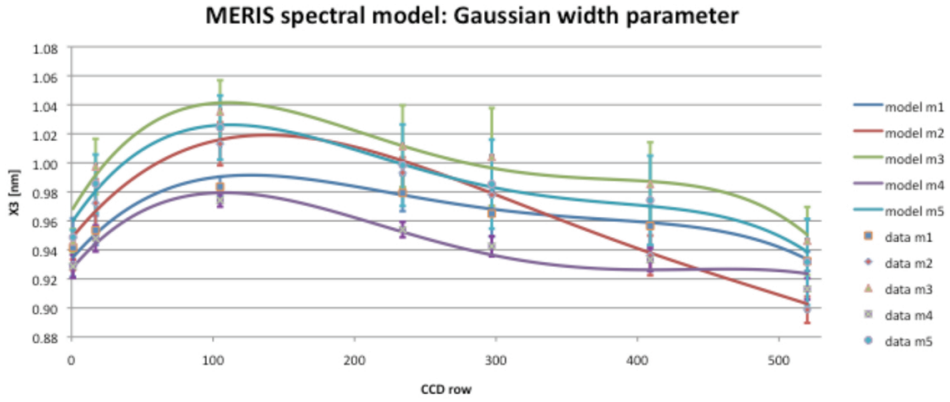

Figure 3.16 Pixel bandwidth deviation [nm] from linear trend as a function of line number (Line 1 = 390 nm, Line 520 = 1040 nm).

Finally, the instrument line-shape response for all pixels and bands is computed from the on-ground measurements, by introducing a variable bandwidth to the

Gaussian response function of the pixels, as a function of line number or wavelength. Figure 3.16 presents the variation of the pixel (line) spectral bandwidth as a function of line number (wavelength) for all five MERIS cameras. The spectral dependence of the bandwidth was fitted, per camera, with a fourth order polynomial to account for its spectral evolution. The root mean square of the bandwidth is included in the plot as is the error bar, showing that bandwidth does vary from pixel to pixel, within each camera, due to slight response non-uniformity (< 5%) within the 22.5 μm pixels.

Although on-orbit calibration can provide an adequate spectral model, it is mandatory that a complete spectral characterization of imaging spectrometers be made on the ground, in order to:

1. verify the proper integration of the optics;
2. provide the CCD pixel's line-shape response, and camera dispersion law; and
3. provide a pre-flight reference from which the spectral stability of the instrument can be derived.

It must be noted that it is important to take proper care of the wavelength shifts from air to vacuum environments, as these can be significant (0.2 nm) in the near infrared.

3.5.6 Spectral stability of MERIS

The spectral stability of the instrument has been monitored regularly by the onboard (Erbium) spectral calibrations and the bi-yearly spectral campaigns (Fraunhofer and oxygen A-band measurements). The results indicated that the spectral stability of the instrument is to within the measurement accuracy, i.e., ±0.1 nm. However, as can be seen in Figure 3.17, cameras 2 and 4 have suffered a shift of their spectral response during the first year on orbit, of approximately 0.15 nm, which later stabilized to within 0.05 nm for Camera 2 and 0.07 nm for Camera 4, while Cameras 1, 3 and 5 have barely drifted <0.05 nm over the complete mission lifetime.

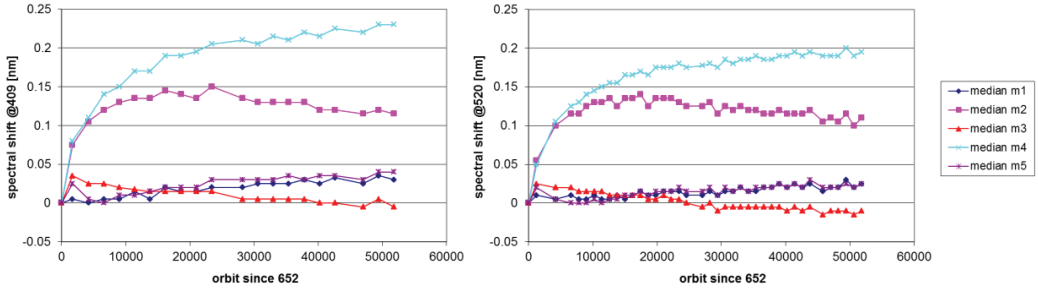

Figure 3.17 Spectral stability since orbit 652 (15/04/2002 to 11/03/2012) as monitored using Erbium doped diffuser measurements: left, peak 1 (ca. 408 nm), and right, peak 3 (ca. 520 nm).

This spectral shift is wavelength independent i.e., it does not affect the spec-

trometer's dispersion law, but only causes a uniform spectral offset per camera for all bands.

The calibration data used to derive the instrument spectral model is from fall 2003 measurements (Delwart et al., 2004), and the regular spectral calibrations of MERIS have shown the instrument to be stable to within ±0.05 nm since that time. Such a small amount of spectral shift has a very low impact on the absolute radiometric accuracy, e.g., ±0.05% at 442 nm, and did not justify specific spectral trending.

Chapter 4

Calibration Using Natural Earth Targets

Bertrand Fougnie and Robert Frouin

4.1 Introduction

To cope with degradation after launch, most ocean-colour sensors are equipped with onboard calibration devices. These devices include internal lamps, solar diffusers, and monochromators. In addition, the spacecraft may be positioned to view the Moon as a calibration target (also discussed in Chapter 3). The accuracy provided by onboard techniques, however, may not be sufficient for ocean-colour applications, and vicarious techniques are needed to verify the onboard device and achieve the required accuracy.

Some ocean-colour sensors, in particular the POLDER instrument, do not have onboard calibration capability at all, or very limited capability. They rely on vicarious techniques using natural Earth targets for calibration, absolute and relative (i.e., multi-temporal and inter-band). The choice was deliberate for the POLDER instrument: it was too expensive to implement a calibration system in the compact POLDER design, and it was difficult to build a device that covered the entire bidirectional field of view. For many other ocean-colour sensors equipped with on-board calibration devices (e.g., SeaWiFS, MODIS, MERIS), these vicarious techniques have been used as alternative techniques to check or evaluate the consistency of the existing official calibration.

A variety of vicarious techniques using natural Earth targets have been developed and applied successfully for many ocean-colour sensors. They use Rayleigh scattering over the ocean for absolute calibration, high-altitude deep convective clouds (also called DCC), desert sites (also called pseudo-invariant sites), or ocean sun glint for relative calibration, and they include "system" vicarious calibration, in which instrument and algorithm are intimately linked. These techniques are reviewed in the following sections, which include uncertainties and application examples.

In this chapter, the calibration will often be evaluated referring to the ratio ΔA_k defined as the ratio of MI, the *measured* TOA normalized radiance derived from the sensor (assuming a given calibration), and CI, the *computed* TOA normalized radiance (computed in various ways, depending on the calibration technique).

4.2 Absolute Calibration Using Rayleigh Scattering

The TOA signal measured by a satellite sensor observing oceanic targets is, for the most part, due to scattering of the incident solar irradiance by atmospheric components, especially in the visible. In this spectral range, and for non-turbid situations (atmospheric and marine), the molecular scattering, so-called Rayleigh scattering, is the main process contributing to the TOA signal, and this contribution can be accurately predicted and computed using surface pressure, knowing the spectral response of the instrument. It should be noted, however, that the radiative transfer codes used to compute the TOA signal have some uncertainties. These uncertainties are not a significant issue as long as the atmospheric correction scheme (creation of look-up tables for molecular and aerosol scattering, etc.) is based on the same radiative transfer code.

Other processes contributing to the TOA signal are aerosol scattering, backscattering by the water body, diffuse reflection by whitecaps, specular (or Fresnel) reflection by the surface, and gaseous absorption. Satellite acquisitions over such oceanic targets can be selected so that the contribution of these secondary processes is minimized. After very restrictive cloud screening and rejection of turbid situations, the molecular scattering signal may constitute as much as 90% of the TOA signal for these acquisitions, for spectral bands from the blue to the red parts of the spectrum (typically 443 to 670 nm). This forms the basis of the calibration method using Rayleigh scattering.

This method, derived from Vermote et al. (1992), was previously explained in Hagolle et al. (1999). The approach is statistical, in the sense that climatology is used for marine reflectance, and cases too contaminated by aerosols are rejected, i.e., the effect of aerosols requires a very small correction. This contrasts with the vicarious radiometric calibration using *in situ* measurements (e.g., Fougnie et al., 1999), in which the TOA signal is computed using measurements of aerosol optical properties and water-leaving radiance. The advantage of the method using Rayleigh scattering is that the calibration is neither geographically or geo-physically limited, but it is derived from a large set of oceanic sites, from both hemispheres and for a large set of conditions.

4.2.1 Selection of observations

4.2.1.1 Geographical selection

The marine contribution represents 10 to 15% of the TOA signal for the blue bands and is consequently an important source of error in attempting to meet the 1 or 2% accuracy in the TOA signal. A climatological study, based on analyzing one year of SeaWiFS data, was performed by Fougnie et al. (2002b) to select adequate oceanic sites for which spatial homogeneity is guaranteed and for which moderate seasonal

effects exist. This climatology was, in general, confirmed in Fougnie et al. (2010) over 9 years of SeaWiFS data. Using such pre-defined oceanic sites, the dispersion of the results inside a given site is reduced significantly, as well as biases between results obtained over the different sites. In practice, six major oceanic sites were recommended in Fougnie et al. (2002b; 2010) i.e. in the North and South Pacific, the North and South Atlantic, and the Indian Ocean (see Table 4.1 and Figure 4.1).

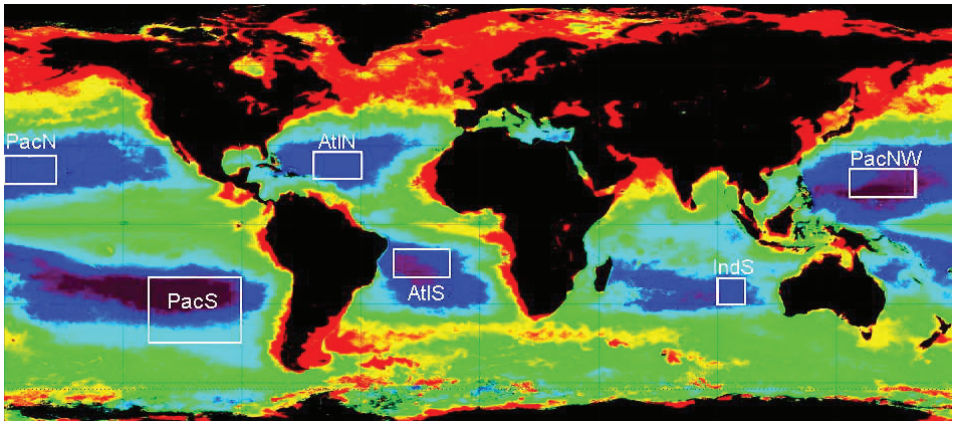

Figure 4.1 Major oceanic sites recommended for the statistical calibration method using Rayleigh scattering (after Fougnie et al., 2002b; 2010).

Table 4.1 Major oceanic sites recommended for the statistical calibration method using Rayleigh scattering (after Fougnie et al., 2002b; 2010.)

No.	Name	Location	Latitude (deg)		Longitude (deg)	
			min	max	min	max
1	PacSE	South-East of Pacific	-44.9	-20.7	-130.2	-89.0
2	PacNW	North-West of Pacific	10.0	22.7	139.5	165.6
3	PacN	North of Pacific	15.0	23.5	179.4	200.6
4	AtlN	North of Atlantic	17.0	27.0	-62.5	-44.2
5	AtlS	South of Atlantic	-19.9	-9.9	-32.3	-11.0
6	IndS	South of Indian	-29.9	-21.2	89.5	100.1

4.2.1.2 Clear-pixel selection

It is obvious that a cloud mask is applied to the data, but in addition, only pixels distant by about 10 pixels (or 10 km) from a cloud are retained to avoid adjacency effects. Furthermore, a strict threshold is applied to the TOA reflectance (in fact the product of reflectance and $cos(\theta).cos(\theta_0)$) in order to reject data with appreciable aerosol loading and sub-pixel clouds. A threshold is also applied to the surface wind speed extracted from meteorological data to avoid possible contamination by

surface whitecaps: only situations with a wind speed less than 5 m s^{-1} are selected. Importantly, we can be highly restrictive about these thresholds (i.e., retain only very clear pixels), yet obtain statistically significant results.

4.2.1.3 Geometrical selection

Pixels potentially contaminated by sun glint are rejected, i.e., observations with viewing direction inside a cone of ±60° around the specular direction are discarded. Also, acquisitions corresponding to extreme geometries, such as solar or viewing zenith angle greater than 60°, are rejected.

4.2.1.4 Ancillary data

Some exogenous data are necessary to compute the TOA signal accurately, such as the surface pressure, the surface wind speed, or the total ozone amount. Naturally, only pixels for which these ancillary data are available, are selected.

4.2.2 Computation of the TOA signal

The following general formulation is used to compute the TOA signal (reflectance):

$$\begin{aligned}\rho_{\mathrm{TOA}}(\theta_0,\theta,\phi) = t_g(\theta_0,\theta)\Big(&\rho_A(\theta_0,\theta,\phi)\\ &+ \rho_w(\theta_0,\theta,\phi)T(\theta_0,\theta)/[1 - S_A\rho_w(\theta_0,\theta,\phi)]\Big)\end{aligned} \tag{4.1}$$

where θ_0, θ, and ϕ are the solar and viewing zenith angles and relative azimuth angle, respectively, t_g is the total gaseous transmittance, ρ_A is the molecular and aerosol contribution including coupling terms and specular reflection by the wavy surface, ρ_w is the marine reflectance, T is the total atmospheric transmission for aerosols and molecules, and S_A is the atmospheric albedo. Note that t_g depends on the amount of absorbers (essentially ozone), ρ_A on aerosol optical thickness, surface pressure, and wind speed, T on surface pressure and wind speed, and S_A on aerosol optical thickness. These various terms are evaluated as described below.

4.2.2.1 Aerosol and molecular scattering contribution

The atmospheric functions ρ_A, T and S_A are computed using an accurate radiative transfer model, such as the successive order of scattering code of Deuzé et al. (1989) or Lenoble et al. (2007). This code includes polarization and specular reflection by the wavy surface. The molecular scattering contribution is accurately computed knowing the surface pressure and the molecular optical thickness corresponding to the spectral band considered. For this, the Rayleigh equivalent optical thickness for a given spectral band is calculated by weighting the spectral optical thickness

computed according to Gordon et al. (1988) by the spectral solar irradiance and the spectral response within the band. The background aerosol contribution is computed knowing its optical thickness estimated at 865 nm (or another reference band) and extrapolated for the considered spectral band using a Maritime 98 aerosol model (Gordon and Wang, 1994). In practice, the restrictive thresholds used for the clear pixel selection lead to a residual aerosol optical thickness lower than 0.05 at 865 nm, and usually about 0.02 – 0.035.

4.2.2.2 Marine contribution

This contribution, representing about 10% of the TOA signal, is estimated over the pre-defined oceanic sites through a climatological study (Fougnie et al., 2002b; 2010). The typical marine reflectance for these sites is 0.033 at 443 nm, 0.020 at 490 nm, 0.0049 at 555 nm, and 0.0007 at 670 nm, and is close to values derived through a bio-optical model using a surface pigment concentration of 0.07 mg m^{-3}. A spectral interpolation can be performed when the spectral band of interest is not exactly the same as one of the SeaWiFS spectral bands for which the climatological values are available. In addition, a bi-directional correction is added as an option to take into account appreciable differences in the viewing and solar geometries of the pixel to calibrate and the angular conditions of the climatological values derived from SeaWiFS (e.g., due local time of overpass or case of multi-directional viewing sensors). This correction is made according to Morel and Gentili (1993).

4.2.2.3 Gaseous contribution

A correction for gaseous absorption is performed for each spectral band. The main contributors are water vapour (mainly around 565 and 865 nm), ozone (mainly around 490, 565, and 670 nm), oxygen (around 765 nm) and nitrogen dioxide (mainly around 443 and 490 nm). The correction can be made using transmittance models such as SMAC (Rahman and Dedieu, 1994), in which gaseous transmittance varies exponentially with air mass and gaseous amount.

4.2.3 Error budget

Table 4.2 summarizes the error budget of the method. For this budget, we have estimated the impact on calibration results of typical uncertainties on the input parameters. We have considered errors made on the surface pressure and surface wind speed (impacting the Rayleigh contribution), on the calibration of the 865 nm band, on the expected aerosol model (impacting the aerosol contribution), on the gaseous absorption, and on the marine reflectance. In this error budget evaluation, using the root-mean-squared (RMS) error as a measure of performance is appropriate and realistic, because of the large amount of data considered in the synthesis, i.e., several geometric, geographic, and geophysical conditions.

In general, the error budget, in terms of RMS, is less than 3.5%. For shorter wavelengths, 443, 490, and 510 nm, the performance is determined by the accuracy of the marine reflectance. This confirms the interest of, and justifies the use of the complementary vicarious approach, in some cases, based on *in situ* measurements to improve the accuracy of the statistical results. For wavelengths near 565 nm, the performance depends equally on the errors of all the parameters. In the red part of the spectrum, i.e., 670 nm, error in the calibration in the near infrared (865 nm) becomes the limiting factor to accuracy.

Table 4.2 Typical error budget for the six main sources of uncertainties.

Error (in %)	443	490	510	565	670
surface pressure: 10hPa	0.81	0.81	0.81	0.81	0.82
surface wind speed: 2 m s^{-1}	1.00	1.00	1.00	1.00	1.00
calibration at 865: 3%	0.50	0.40	0.49	0.74	1.42
aerosol model (50% at 443)	0.57	0.55	0.53	0.42	0.33
gas amount error of 20%	0.12	0.38	0.71	1.62	0.74
marine reflectance	3.06	2.59	2.16	0.96	0.33
RMS	3.41	3.36	3.00	2.43	2.11
MAX	6.06	5.73	5.70	5.55	4.64

4.2.4 Calibration algorithm and analysis

The evaluation consists of comparing the TOA normalized radiance computed from the radiative transfer model (CI) with the normalized radiance derived from the sensor measurements (MI), assuming a given calibration (the one we want to evaluate). Consequently, the ratio ΔA_k, defined as MI/CI, provides a measure of the difference in actual calibration coefficients with respect to reference values. This comparison is made for each selected pixel and/or viewing direction.

It was evidenced that a site-by-site analysis is sometimes useful. In fact, residual biases still exist on the specified marine reflectance and these biases differ for each oceanic site. If we limit the analysis to one given site, the bias will be the same for each pixel of the data set, with certain relative effects (of course, not absolute), such as a small temporal decrease or multi-angular calibration errors, that become easier to detect.

Analysis in relation to various other parameters can help with understanding potential problems. For example, the variation with viewing geometry (zenith viewing angle, for instance) may indicate some problem in the multi-angular calibration, often called the smile effect. The variation with aerosol content may reveal a problem in the calibration of the 865 nm spectral band (or the spectral band used to estimate the aerosol amount), or the supposed aerosol model (Maritime 98). The variation

with the Rayleigh contribution or with geometry may point to some residual problem with the polarization sensitivity of the instrument.

4.2.5 Application examples

Figures 4.2 and 4.3 display ΔA_k calibration coefficients obtained for POLDER-2 (January to June 2003) and SeaWiFS (April to August 2000).

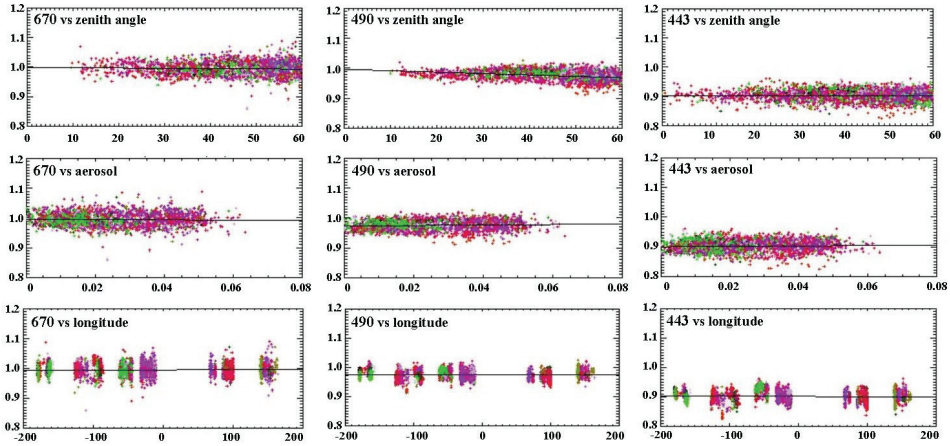

Figure 4.2 Absolute radiometric calibration of POLDER-2 at 443, 490, and 670 nm during the period from January to June 2003. Calibration coefficients ΔA_k are displayed as a function of viewing zenith angle (top), aerosol optical thickness (middle), and longitude (bottom).

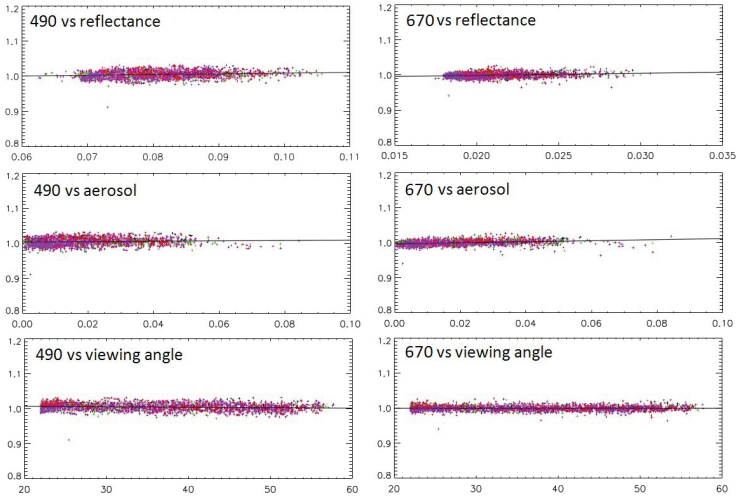

Figure 4.3 Absolute radiometric calibration of SeaWiFS at 490 nm and 670 nm during the period from April to August 2000. Calibration coefficients ΔA_k are displayed as a function of reflectance, aerosol optical thickness and zenith viewing angle.

The estimated ΔA_k calibration coefficients for POLDER-2, with respect to pre-launch values, do not depend significantly on aerosol optical thickness, viewing zenith angle, and geographic location except perhaps for band 490 nm, which shows a slight variation with the viewing angle. At the opposite extreme, no variation with viewing angle is observed for SeaWiFS while a very small dependence with reflectance or aerosol optical thickness is apparent, especially at 670 nm. The values ($\pm$ one standard deviation) are 0.995 ($\pm$0.019), 0.976 ($\pm$0.014), and (0.902$\pm$0.017) for POLDER-2, and 1.004 ($\pm$0.010) and 0.999 ($\pm$0.007) for SeaWiFS. The standard deviations represent less than 2% of the ΔA_k values, attesting to the accuracy of the method. The temporal evolution of the radiometric calibration may be monitored by systematically and operationally examining suitable sites, allowing not only detection of long-term trends, but also of high frequency changes that may occur as a result of changes in the data processing, or due to onboard calibration adjustments, as evidenced in Figure 4.4 for MERIS.

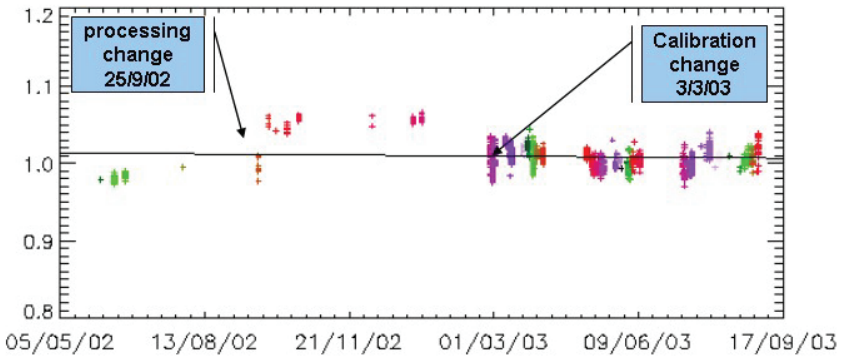

Figure 4.4 Temporal change in the early versions of MERIS products as seen through the calibration coefficient A_k at 490 nm derived over Rayleigh scattering.

As this example illustrates, the Rayleigh scattering method is efficient for the absolute calibration of ocean-colour sensors. This method has been applied for many ocean-colour sensors (Fougnie et al., 2012a) with very good results as reported in Fougnie et al. (2007) for PARASOL, Bruniquel et al. (2013) for SeaWiFS, Fougnie et al., (2012b) for MERIS, and Fougnie et al. (2013) for MODIS. The method provides calibration coefficients with an inaccuracy of 3-4% (better statistically), for spectral bands in the visible and red. The method is not applicable to the near infrared, where molecular scattering is ineffective. A more accurate specification of the marine reflectance in the blue would reduce uncertainties in this spectral range. Using oligotrophic waters is not ideal in the blue because the marine reflectance is high, but it is difficult to find oceanic areas away from the coast with large and stable chlorophyll concentrations.

4.3 Inter-Band Calibration Using Sun Glint

The sun glint reflectance from the ocean surface is high and spectrally flat over the spectral range of interest, i.e., the visible to near infrared. Consequently, it provides an opportunity to inter-calibrate spectral bands. After a proper selection of the satellite data is made (see below), the processes contributing to the TOA signal are molecular scattering, background aerosol scattering, backscattering by the water body, gaseous absorption, and of course, specular reflection (glitter), which contributes 60 to 90% of the total signal depending on wavelength and wind speed.

Essentially, the sun glint reflectance depends on the geometrical conditions and on surface roughness. It is predicable using models based on observations (Cox and Munk, 1954; 1955), although it is difficult to determine accurately the surface wind speed (RMS accuracies generally less than 1-2 m s^{-1}), leaving aside the potential limitations of the model. This explains why the sun glint approach is not a good candidate for absolute calibration. It is, however, adequate for inter-band calibration, where the problem is avoided by using a reference band (in practice a band in the red i.e., 670 nm) to fully characterize the glitter signal, regardless of the wind speed and direction, or more precisely, the surface roughness.

4.3.1 Selection of observations

4.3.1.1 Geographical selection

The sun glint areas are indeed bright, but pre-selected oceanic sites are used to reduce the uncertainties on marine reflectance. Oceanic sites are the same as those presented in Section 4.2 for the calibration using Rayleigh scattering (Fougnie et al., 2002b and 2010).

4.3.1.2 Clear-pixel selection

For multi-directional sensors such as POLDER or MISR, a threshold is applied to the signal measured in the near infrared, in a direction for which the glitter contamination becomes null (the case of POLDER is described in detail in Hagolle et al., 1999). If the sensor is not multi-directional, exogenous data can be used to estimate the aerosol amount and reject targets potentially contaminated by aerosol (as shown by Hagolle et al., 2004); otherwise the accuracy of the method is degraded.

4.3.1.3 Geometrical selection

The brightest conditions are selected using a threshold on the wave angle θ_n defined by:

$$\theta_n = arcos\Big([cos(\theta_0) + cos(\theta)]/[2cos(\theta_p/2)]\Big) \tag{4.2}$$

with

$$\theta_p = arcos[cos(\theta_0)cos(\theta) + sin(\theta_0)sin(\theta)cos(\phi)], \tag{4.3}$$

where θ_p is the angle between the solar and viewing directions. Only the pixels corresponding to a wave angle below 4° are retained.

4.3.1.4 Ancillary data

Some exogenous data are necessary to compute accurately the TOA signal, namely the surface pressure, the surface wind speed, and the total ozone amount, and only the pixels for which these ancillary data are available are selected. A restrictive threshold is applied to the surface wind speed: observations with wind speeds greater than 5 m s^{-1} are discarded to avoid possible contamination by surface whitecaps.

4.3.2 Computation of the TOA signal

The following general formulation is used to compute the TOA signal (reflectance):

$$\begin{aligned}\rho_{\mathrm{TOA}}(\theta_0,\theta,\phi) = t_g(\theta_0,\theta)\Big(&\rho_A(\theta_0,\theta,\phi) + \rho_g(\theta_0,\theta,\phi)T_{dir}(\theta_0,\theta) \\ &+ \rho_w(\theta_0,\theta,\phi)T(\theta_0,\theta,)/[1 - S_A\rho_w(\theta_0,\theta,\phi)]\Big)\end{aligned} \tag{4.4}$$

where ρ_g is the sun glint reflectance, T is the total atmospheric transmission for aerosols and molecules and T_{dir} is the direct atmospheric transmission for aerosols and molecules. Compared with Equation 4.1, Equation 4.4 includes explicitly the sun glint contribution. The different terms of this equation are determined as described below.

4.3.2.1 Glitter reflectance

The reference band in the red (e.g., 670 nm) is used to estimate the sun glint reflectance, after correcting the contributions due to Rayleigh and aerosol scattering and gaseous absorption, and the marine reflectance.

4.3.2.2 Aerosol and molecular scattering contribution

As in the Rayleigh scattering method, ρ_A and T, are computed using an accurate radiative transfer model, such as the successive order of scattering code of Deuzé et al., (1989) or Lenoble et al. (2007), which includes polarization and specular reflection by the wavy surface. The molecular scattering contribution is computed from the surface pressure and molecular optical thickness corresponding to the spectral band considered. The background aerosol contribution is computed using

the aerosol characterization made in a viewing direction outside the glitter influence when the sensor is multi-directional (e.g., POLDER, MISR), or using arbitrary assumptions (e.g., climatological values) when this is not the case (e.g., SeaWiFS, MERIS, MODIS).

4.3.2.3 Marine contribution

The term involving the marine reflectance represents about 5% of the TOA signal for the shorter wavelengths in the sun glint viewing conditions, and much less in the reference band in the red. The marine reflectance is specified from the statistical study of Fougnie et al. (2002b; 2010). Typical values at the pre-selected oceanic sites are given in Section 4.2.2

4.3.2.4 Gaseous contribution

As described in Section 4.2.2 for the Rayleigh scattering method, gaseous absorption is corrected in each spectral band using a transmittance model, for example the SMAC model (Rahman and Dedieu, 1994).

4.3.3 Error budget

To estimate the error budget of the sun glint calibration method, the major errors are considered. These include the error on the refractive index of water (limitation above 1 μm, small variations with temperature and salinity). The inter-band method can be extended to spectral bands centered at 1.0, 1.6 or 2.2 μm, but in the near infrared and beyond uncertainties on the refractive index become predominant in the error budget. Other errors taken into account are those on the marine reflectance (20%), on the gaseous correction (considering a 20% error on the amount), on the aerosol correction (considering the aerosol model is wrong and optical thickness is biased by 0.03), and on wind speed. Note that the error due to the wind speed is negligible because the glitter signal is not computed using the wind speed, but is measured through the reference red band.

The sun glint signal is highly polarized especially in the particular angular configuration of observing near the Brewster angle (see Toubbé et al., 1999 and Hagolle et al., 2004). Consequently, errors due to polarization sensitivity of the sensor may be significant: for ocean-colour sensors, the residual difference error between spectral bands is estimated at 0.5%.

Table 4.3 gives the error budget for the inter-band calibration between the reference band (here 670 nm) and the other bands. Of course, when considering absolute aspects, i.e., propagating the absolute calibration to the other bands, the calibration error of the reference band should be taken into account. In the Table, MAX is the maximum error that we can expect. Consequently, when a large amount

Table 4.3 Typical error budget for the inter-band calibration method (in %) using Sun glint.

Error (in %)	443	490	510	565	865
Surface pressure (Rayleigh) 15 hPa	0.34	0.25	0.22	0.16	0.03
Seawater refraction index	0.30	0.24	0.21	0.14	0.60
Aerosol error (model and amount)	1.01	0.78	0.69	0.43	0.53
Gas amount error of 20%	0.75	0.83	1.03	1.78	0.77
Wind speed	0.01	0.01	0.01	0.01	0.01
Marine reflectance	1.50	1.10	0.94	0.33	0.00
Polarization sensitivity	0.50	0.50	0.50	0.50	0.50
RMS	2.07	1.70	1.66	1.94	1.21
MAX	4.40	3.71	3.58	3.34	2.43

of data is used to perform the inter-band calibration, which is generally possible, this maximum error corresponds approximately to the 3-sigma error on results obtained for very different geometrical, geographic and geophysical conditions. The root-mean-squared of the individual errors, RMS, is a good indicator of the actual accuracy of the method. It is generally less than 2%, the maximum value being obtained at 443 nm due to the uncertainty in the marine reflectance. At 565 nm, RMS is almost 2% due to possible uncertainty in the ozone amount (the largest uncertainty), hence the gaseous transmittance.

4.3.4 Calibration algorithm and analysis

The intrinsic sun glint reflectance, ρ_g, derived from the TOA reflectance measured in the reference spectral band, is used to predict the TOA reflectance in the other spectral bands, i.e., to obtain CI. The choice of the reference band is crucial for the global accuracy of the method. In order to obtain a good accuracy, the reference band must be well calibrated, since any calibration error in the reference band is transmitted to the band to be calibrated. Since for many ocean-colour sensors the confidence in the pre-flight calibration is lower than for the Rayleigh scattering calibration, so the reference band should be chosen among the spectral bands that are calibrated with the latter.

The algorithm first seeks the wind speed that corresponds to a TOA radiance equal to the measured TOA radiance in the reference band. Then this wind speed estimate is used to compute the reflectance that should be measured in the other bands. The computations of the TOA reflectance require information on aerosol optical properties. It is necessary to obtain this information from another sensor that does not observe in the sun glint. The sensitivity study of Hagolle et al. (2004) indicates that accuracy is weakly affected by aerosol optical thickness for maritime aerosols (small spectral dependence of the aerosol reflectance), and that pixels for which the optical thickness is above 0.15 and the Ångström coefficient is above 0.3,

should be discarded.

4.3.5 Application examples

Figure 4.5 displays the ΔA_k calibration coefficients obtained for MODIS at 469, 858, 1240, and 2130 nm as a function of the zenith viewing angle. They show little dispersion, especially at 858 nm, near the reference band. The dispersion is larger towards the blue at 469 nm, or the shortwave infrared, at 2130 nm. This can be attributed to uncertainty in the modelling of the interactions between surface reflection and molecular/aerosol scattering, and to uncertainty in the water reflectance. The transfer of the calibration in the red to the near infrared is accurate, and allows an absolute calibration in this spectral range, complementing the Rayleigh scattering method.

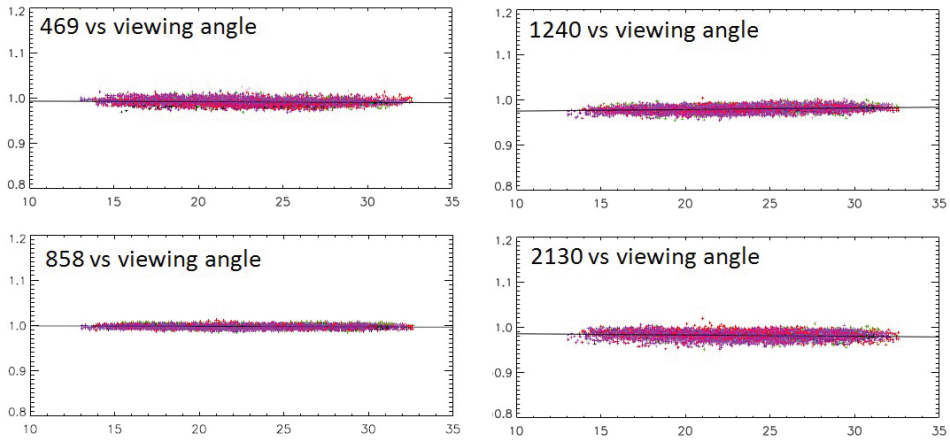

Figure 4.5 Inter-band calibration (ΔA_k coefficient) of the MODIS spectral bands at 469, 858, 1240, and 2130 nm using the sun glint method as a function of zenith viewing angle. Data were collected in December 2003. The spectral band of reference is centered at 645 nm.

Figure 4.6 illustrates the potential of the method for monitoring temporal changes in the calibration. The ΔA_k calibration coefficient at 765 nm, transferred from 670 nm as described above, is displayed as a function of time during the operational periods of PARASOL. A significant temporal trend is apparent. It was confirmed in Fougnie et al., (2009) by other techniques and considered for a correction of the calibration on the Level-1 update. The same result is obtained for the MERIS calibration at 858 nm, transferred from 620 nm. A perfect stability of this inter-band calibration is observed, validating the temporal consistency of the official calibration used to generate the Level-1 archive.

This inter-band calibration method has been successfully applied for MERIS (Fougnie et al., 2012b), MODIS (Fougnie et al., 2013), and PARASOL (Fougnie et al., 2007) and is recommended for ocean-colour sensors (Fougnie et al., 2012a; IOCCG,

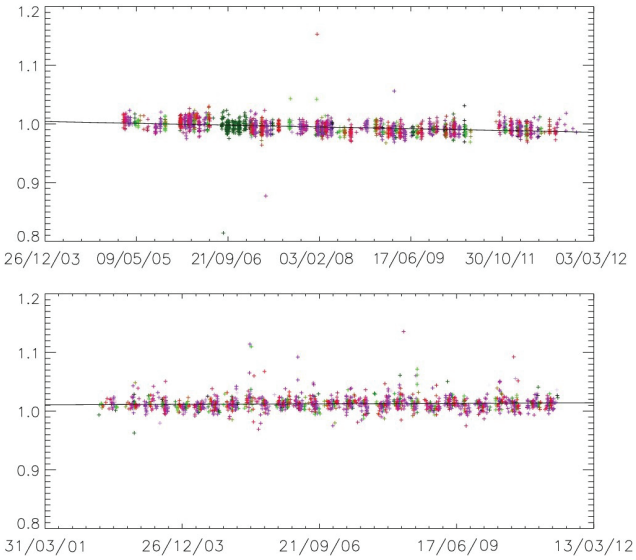

Figure 4.6 Temporal evolution of the ΔA_k coefficient obtained before correction at 765 nm for PARASOL (top) and after correction at 865 nm for MERIS (bottom) using the sun glint inter-band calibration method.

2012) because the sun glint calibration method is an efficient way to transport with a good accuracy the calibration of spectral bands in the visible to infrared bands up to 2,130 nm. If the uncertainty of the absolute calibration coefficient of the reference band at 670 nm is 2% RMS (see Section 4.2), then the calibration of a band at 865 nm can be obtained with an uncertainty of about 3.3%. It is important to note, however, that many ocean-colour sensors saturate over sun glint, limiting the application of the method. Furthermore, issues of non-linearity in the sensor response should be carefully addressed for the method to be effective for ocean-colour remote sensing.

4.4 Inter-Band Calibration Over Bright Clouds

From the point of view of satellite sensor calibration, high and dense scattering clouds are diffusers comparable to the Moon, i.e., they exhibit a white spectral signature and very limited perturbing contributors, which simplifies the modelling. Such clouds are excellent candidates for inter-band calibration purposes or multi-temporal monitoring, as discussed in Vermote and Kaufman (1995), Hagolle et al. (1999), Lafrance et al. (2002), and Fougnie et al. (2007; 2009).

Selecting high convective clouds, also called deep convective clouds (DCC), guarantees negligible, or very small surface effect, aerosol and Rayleigh scattering contributions, and a small impact of cloud microphysics, i.e., of the particle types composing the cloud. The modelling of such an intensively scattering system becomes greatly simplified, indeed.

A first approximation of a perfectly white spectral behavior of the cloud, after correction of gaseous absorption, gives an inter-band calibration accuracy within a few percent by extrapolating the cloud reflectance measured at a given spectral band of reference. A refined modelling, described hereafter, uses the reference band to invert the cloud optical thickness assuming a type of cloud top particles, and computes for other bands the reflectance to be compared with the satellite sensor measurement through a radiative transfer look-up-table.

4.4.1 Selection of observations

The success of the calibration over clouds is made by a rigorous selection of adequate targets and viewing geometries (see details in Fougnie and Bach, 2009).

4.4.1.1 Geographical selection

The candidate targets are thick convective cumulonimbus clouds over oceans, i.e., a relatively dark surface. They develop above subtropical warm oceans, in inter-tropical latitudes between 30°N and 30°S, and are regularly affected by atmospheric convective dynamics.

4.4.1.2 Cloud selection

The two most important characteristics to consider for selection are dense scattered convective clouds and very high altitude clouds. This can be guaranteed using a powerful criterion that makes use of absorption bands near 763 nm (when available) from which it is possible to derive the apparent oxygen pressure, yielding a good estimation of the cloud top altitude. A restriction to apparent pressure lower than 400 hPa leads to cloud altitude higher than 8-km. But the altitude is not sufficient: cirrus clouds are not good candidates, while cumulonimbus are adequate. The best criterion to guarantee the selection of a very dense convective cloud is the TOA reflectance that must be greater than 0.8 in the near infrared band (e.g., 865 nm). Another complementary spectral criterion may be carefully used considering the fact that the residual Rayleigh contribution above the cloud is about 2-3% in the blue band. To select clouds above the ocean, observations located at less than 30 km from a coastline are discarded. Finally, a criterion is considered for characterizing the homogeneity of the cloud: the relative standard deviation of the TOA reflectance for the near infrared band in a 30×30 km^2 area must be less than 3%.

4.4.1.3 Geometrical selection

It is recommended that observations corresponding to viewing geometries near the specular reflection be rejected by selecting relative viewing azimuth angles between 30 and 150°. To avoid possible shadowing effects, measurements corresponding

to solar zenith angle greater than 30°, or viewing zenith angle greater than 40°, are discarded. In addition, restricting the analysis to such "near-nadir" geometries limits the impact of cloud microphysics, which is unknown (Lafrance et al., 2002; Fougnie and Bach, 2009).

4.4.2 Computation of the TOA signal

The computation of the TOA signal is made using the formulation described below:

$$\rho_{\mathrm{TOA}}(\theta_0, \theta, \phi) = t_g(\theta_0, \theta)\rho[\theta_0, \theta, \phi, (\tau^n_{cld} + \tau^n_a + \tau^n_R)_n] \tag{4.5}$$

where ρ is the reflectance at the top of the cloud/atmosphere system and, for each layer n, τ_{cld} is the cloud optical thickness, and τ_R and τ_a the molecular and aerosol optical thicknesses respectively. The reflectance at the top of the cloud/atmosphere system, ρ, is computed using a Discrete Ordinates code (Stamnes et al., 1988) assuming a vertical description of the cloud and atmosphere divided into 16 layers, and for which cloud particle type, aerosol type, and optical thickness are defined according Lafrance et al. (2002).

4.4.2.1 Cloud optical thickness

The reference band in the red (e.g., 670 nm) is used to estimate the cloud optical thickness by an inversion algorithm using look-up-tables computed with the Discrete Ordinates code. An accurate description of the cloud microphysics should require a multi-phase and vertical profile description, which is usually unknown. In the modelling, the convective cloud is divided into a lower layer from 1 to 6 km high composed of liquid water droplets, covered by an upper layer from 6 to 15 km high composed of ice particles. This approximation, discussed in Lafrance et al. (2002), is in fact realistic. The liquid layer is homogeneous with a size distribution corresponding to cumulonimbus droplets as reported in Stephens (1978). The ice particles are hexagonal columns, plates or compact hexagonal crystals as observed by Chepfer et al. (1998). Each particle is characterized by its albedo, asymmetry factor, phase function, and scattering and extinction coefficients. In practice, the plate particle type is used as a good compromise, and variations with model particle have a small effect, at least for the visible range (see Fougnie and Bach, 2009).

4.4.2.2 Molecular scattering contribution

The vertical molecular profile is computed for the 16 atmospheric layers from the product of the vertical pressure profile for a standard tropical profile (McClatchey et al., 1972) and the usual molecular optical thickness.

4.4.2.3 Aerosol scattering contribution

The aerosol contribution is taken as representative of mid-latitude summer conditions, i.e., a WMO (1986) Maritime-I case including 3 homogeneous layers: an under layer of maritime aerosols from sea surface to 2 km high with an optical thickness of 0.05 at 550 nm, a layer of continental aerosols from 2 km to 12 km high with an optical thickness of 0.025 at 550 nm, and an upper background layer of stratospheric aerosols up to 12 km high with an optical thickness of 0.005 at 550nm. The global aerosol optical thickness is consequently 0.08 at 550 nm.

4.4.2.4 Surface contribution

The marine reflectance just above the surface is assumed Lambertian and to correspond to a typical chlorophyll concentration of 0.1 mg m^{-3}. Sun glint is not considered because viewing geometries favoring sun glint are discarded.

4.4.2.5 Gaseous contribution

For the selected convective cloud conditions, water vapor and oxygen absorption can be neglected in the 443 to 865 bands, as shown in Lafrance et al. (2002). On the other hand, the ozone contribution, mainly affecting 490, 565, and 670 nm bands must be taken into account using a transmittance model with the ozone content from TOMS data or climatology, as input.

4.4.3 Error budget

To estimate the error budget of the calibration method over clouds, the major errors are considered. Using very dense and high convective clouds essentially limits the errors due to the particle model for the top of the cloud. The cloud top altitude leads to an uncertainty in the Rayleigh scattering contribution above the cloud (error of 3 km), the gas content (error of 20% on ozone and oxygen), and the background stratospheric aerosol content (100% error on the optical thickness). Uncertainties for the other contributors have a very small or negligible effect. The various errors are quantified and summarized in Table 4.4.

For the 490, 565 and 765 nm spectral bands, close to the 670 nm reference band, the error due to cloud microphysics is very small. For the 565 and 765 nm bands, the method inaccuracy is mostly due to the uncertainty in gaseous transmission, which represents about 6% for both bands (ozone for 565 nm and oxygen for 765 nm). For the 443 nm blue band, inaccuracy is dominated by errors in cloud top altitude, directly linked to the observed Rayleigh scattering contribution, and cloud microphysics. At the opposite end of the spectrum, i.e., 865 nm, cloud microphysics becomes the main uncertainty. The error budget is the most favorable at 490, 565, and 765 nm, for which the RMS performance is about 1%.

Table 4.4 Typical error budget for the inter-band calibration method over clouds.

Error type	443	490	565	765	865
Cloud particle model (microphysics)	2.19	1.01	0.73	0.47	2.33
Cloud top altitude (3 km)	0.69	0.42	0.18	0.07	0.11
Aerosol (100% on stratospheric AOT)	0.14	0.09	0.05	0.02	0.04
Gas amount (20% for O_3/O_2)	0.39	0.19	0.81	0.95	0.34
RMS	2.33	1.12	1.11	1.06	2.36
MAX	3.41	1.72	1.77	1.51	2.82

4.4.4 Calibration algorithm and analysis

As described in Section 4.2.4, the ratio of the measurements made by the satellite sensor to the TOA reflectance gives the absolute calibration coefficient, ΔA_k, for the considered spectral band. In the process, the intrinsic cloud optical thickness, τ_{cld}, derived from the reflectance measured by the instrument in the reference spectral band, is used to predict the reflectance in other spectral bands. As for inter-band calibration over sun glint, the choice of the reference band is crucial for the global accuracy of the method. To obtain a good accuracy, the reference band must be well calibrated, since any calibration error in the reference band is transmitted to the band to be calibrated. A spectral band that was previously calibrated over Rayleigh scattering is usually selected, and the best compromise is the red 670 nm band.

Assuming a cloud particle type (hexagonal, plate, or column) for the upper layer of the cloud, the inter-band calibration over clouds method is an efficient way of transporting the calibration of a reference band in the visible to other bands in the visible and near-infrared (from 490 to 865 nm). For greater wavelengths, assumptions made on cloud microphysics, and especially the absorption process inside the clouds, becomes a limiting factor. For example, it was found to be impossible to calibrate in the absolute, the 1020 nm spectral band of the POLDER-3 instrument aboard PARASOL using the cloud inter-band method to propagate absolute calibration in the red, but pertinent results were nevertheless obtained for multi-temporal calibration. For sensors designed for ocean-colour observations, nonlinearity issues of the instrumental response must be carefully addressed for unbiased interpretation of the results. However, the main limitation is saturation occurrences, since such sensors have acquisition dynamic ranges that are often dimensioned for clear atmosphere observations.

4.4.5 Application examples

Figure 4.7 displays the ΔA_k calibration coefficients obtained for MERIS at 442, 560, 708, and 885 nm as a function of the TOA reflectance at 681 nm, the reference band. As for the inter-band method over sun glint, they show little dispersion, especially

in the visible range (0.4% for 443 nm), near the reference band (0.2% for 560 nm). The dispersion is larger at 885 nm because of slightly increased uncertainties due to the cloud optical thickness and cloud particle type, as demonstrated in Fougnie and Bach (2009). The transfer of the calibration in the red to blue and the near infrared is accurate, and allows an absolute calibration in this spectral range, complementing other calibration methods (Rayleigh, sun glint).

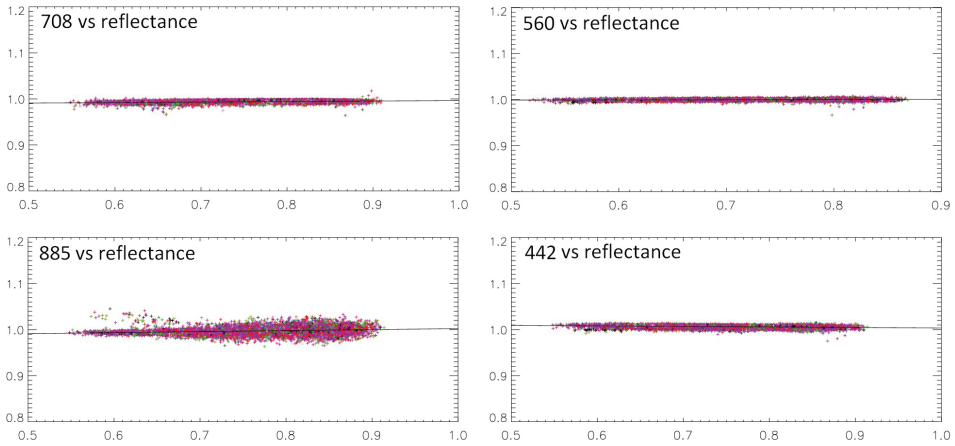

Figure 4.7 Inter-band calibration (ΔA_k coefficient) of the MERIS spectral bands at 442, 560, 708, and 885 nm using the cloud method. Data were collected between 2002 and 2011. The spectral band of reference is centered at 681 nm.

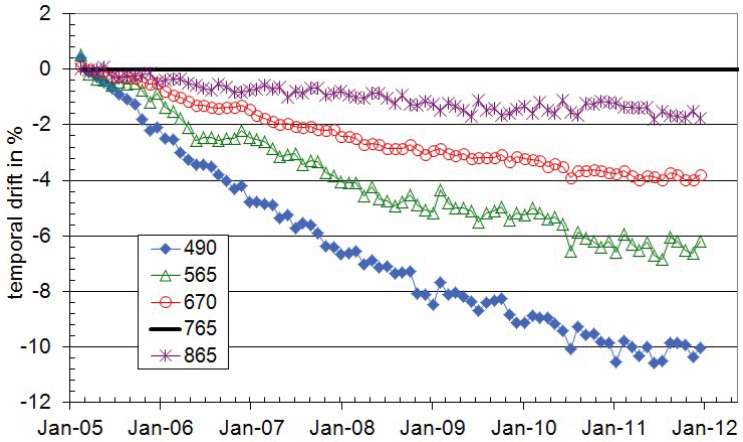

Figure 4.8 Temporal monitoring of the radiometric sensitivity obtained for PARASOL/POLDER-3 spectral bands (except 443 nm) using the inter-band calibration over cloud method and 765 nm as a temporal stable reference (see also Fougnie and Bach, 2009).

Figure 4.8 illustrates the strong potential of the method for monitoring temporal changes in the calibration coefficients. The ΔA_k calibration coefficient for 490 nm to 865 nm, transferred from 765 nm as described above, is displayed as a

function of time during the 7 years of POLDER-3 aboard PARASOL. Assuming 765 nm as a temporal stable reference, a significant decrease with time was detected, monitored, and modelled for all spectral bands. This decrease has been confirmed using other calibration methods, including the Rayleigh scattering method, the inter-band calibration over sun glint, and the cross-calibration over desert sites (Fougnie and Bach 2009).

4.5 Cross-Calibration Over Desert Sites

Measurements over natural targets of pseudo-invariant calibration sites (PICS) such as desert sites have been exploited for many years for cross-calibration and multi-temporal monitoring purposes in the solar spectral range. Accessibility in term of cloudiness and stability with time are the main advantages of such sites.

In the cross-calibration exercise of two sensors, simultaneous measurements of the sensor-to-be-calibrated and the reference sensor, hereafter called StC and RS, respectively, are usually required in order to minimize geometric effects strongly limiting the direct comparison of measurements. The use of stable and homogeneous desert sites allows a wider applicability of such comparisons through a bidirectional and spectral characterization of the surface reflectance of the site.

In this approach, fully described in Lachérade et al. (2013), 20 adequate desert sites were selected, and observations by several space sensors, including ocean-colour sensors, have been collected for many years (Cabot et al., 1999; Lachérade et al., 2013). The size of the desert sites is 90×90 km^2, and for one given acquisition the radiometric and geometric quantities are averaged over the site and saved into the archive. This archive offers the ability to select various reference sensors depending on the objective. In particular, it allows multi-sensor comparisons as reported, for example, by Fougnie et al. (2002a; 2012a).

4.5.1 Selection of observations

All steps for the selection of observations are described in detail in Lachérade et al. (2013).

4.5.1.1 Geographical selection

Observations over 20 desert sites are privileged (Table 4.5). These reference sites have been identified through a systematic climatological study using METEOSAT-4 data (Cosnefroy et al., 1993) and documented in Lachérade et al. (2013). Selection criteria were:

- an excellent spatial homogeneity based on 3% dispersion threshold on the TOA reflectance over the 90×90 km^2 area,
- a temporal stability better or equal to 15% on a seasonal scale,

- a low cloud cover with annual percentages of clear days greater or equal to 50%, and
- precipitation lower than 10 mm per month to avoid surface reflectance anomalies (Cosnefroy et al., 1996).

Table 4.5 Name and location (latitude and longitude) of the 20 desert sites selected for cross-calibration (after Lachérade et al., 2013).

Site	Lat.	Lon.	Site	Lat.	Lon.	Site	Lat.	Lon.
Algeria 1	23.65	-0.55	Libya 1	24.50	13.30	Mauritania 1	19.40	-9.30
Algeria 2	26.00	-1.20	Libya 2	25.05	20.48	Mauritania 2	20.85	-8.78
Algeria 3	30.32	7.60	Libya 3	23.15	23.30	Niger 1	19.85	10.00
Algeria 4	30.10	5.70	Libya 4	28.55	23.39	Niger 2	21.10	10.60
Algeria 5	31.02	2.23	Arabia 1	18.88	46.76	Niger 3	21.57	7.96
Egypt 1	27.12	26.10	Arabia 2	20.13	50.96	Mali 1	19.12	-4.85
Sudan	21.90	28.22	Arabia 3	28.70	43.50			

4.5.1.2 Cloud selection

The cloud mask is based on a threshold using a spectral criterion. Measurements for which ($\rho_{865} - \rho_{443}$) is less than 0.2*($\rho_{865} + \rho_{443}$), where ρ_{865} and ρ_{443} are TOA reflectance at 865 and 443 nm, respectively, are declared cloudy. The second powerful criterion is the use of oxygen absorption bands when available, for example bands centered at 753 and 760 nm for MERIS, or 763 and 765 nm for POLDER. Observations for which the difference between the surface pressure and the apparent pressure derived from the absorption bands is greater than 200 hPa are flagged cloudy and discarded. Finally, sensors having thermal infrared bands also provide very useful information for cloud screening.

4.5.1.3 Geometrical selection

No particular restriction is required, but it was identified that calibration results derived from acquisitions near the backscattering direction, or for very large viewing zenith angles, become inaccurate because of bidirectional effects of the ground surface and/or limitation in the atmospheric correction.

4.5.2 Computation of the TOA signal

The following general formulation is used to compute the TOA signal (reflectance) for a given spectral band λ :

$$\rho_{\mathrm{TOA}}(\lambda,\theta_0,\theta,\phi) = t_g(\lambda,\theta_0,\theta).\Big(\rho_A(\lambda,\theta_0,\theta,\phi) + \rho_{sur}(\lambda,\theta_0,\theta,\phi)T(\lambda,\theta_0,\theta)/[1-S_A(\lambda)\rho_{sur}(\lambda,\theta_0,\theta,\phi)]\Big) \tag{4.6}$$

where ρ_{sur} is the desert surface reflectance.

4.5.2.1 Surface reflectance

The surface reflectance ρ_{sur} considered in Equation 4.6 to compute the TOA reflectance for the sensor to be calibrated (StC) is estimated as follows. Starting with ρ_{RS}, the TOA reflectance measured by the reference sensor (RS), the reference surface reflectance, $\rho_{RS_{sur}}$, is computed as:

$$\rho_{RS_{sur}} = [\rho_{RS} - \rho_A t_g]/[T t_g - S_A \rho_A t_g + S_A \rho_{RS}] \tag{4.7}$$

where t_g, S_a, ρ_A, and T have been defined previously, and where θ_0, θ, ϕ and λ are omitted for clarity. Different options are possible to estimate the surface reflectance for the StC, ρ_{sur}. A band-by-band approach, directly assuming for a given spectral band that $\rho_{sur} = \rho_{RS_{sur}}$, may be used when spectral bands of StC and RS are nearly identical. This is the case, for example, when cross-calibrating POLDER-1 with POLDER-2, MODIS-Aqua with MODIS-Terra, or when cross-calibrating the MERIS 490 nm band with the SeaWiFS 490 nm band. More generally, the surface reflectance, ρ_{sur}, can be assessed from the transmission of the spectral band λStC and a surface reflectance spectrum, ρ_{spec}, according to:

$$\rho_{sur}(\lambda_{StC}) = \int \lambda_{StC}\rho_{spec}(\lambda)t(\lambda)d\lambda \tag{4.8}$$

where the surface spectrum is obtained through spectral interpolation of $\rho_{RS_{sur}}$ using a spline function (Lachérade et al., 2013; Henry et al., 2013) or a specific mathematical model (Cabot et al., 1999; Miesch et al., 2003).

4.5.2.2 Atmospheric scattering contribution

The atmospheric TOA reflectance, including molecules, aerosol, and coupling terms, is computed using a radiative transfer code like 6S (Vermote et al., 1997), assuming a constant desert aerosol model with an optical thickness of 0.2. The assumptions about aerosols are expected to be representative of the average conditions, except for marginal large aerosol events (Cabot et al., 1999; Govaerts and Clerici, 2004).

4.5.2.3 Gaseous contribution

Ozone content, water vapor, and surface pressure are taken from meteorological data. Gaseous transmittance is computed for atmospheric corrections using a transmittance model, for example SMAC (Rahman and Dedieu, 1994).

4.5.2.4 Error budget

Table 4.6 summarizes the error budget of the cross-calibration method, which is limited to the main uncertainties in the input parameters, approximation in the modelling, and assumptions for the description of the atmosphere-surface system. The errors considered are those made in the surface reflectance model (estimated in Miesch et al., 2003, but unfortunately dependant on the interpolation method as described in Henry et al., 2013), in the selection of the reference measurements (including the selection of the reference geometry using the sensitivity study of Cabot et al., 1998; 1999), in the gaseous absorption, in the atmospheric correction (including aerosol contribution and surface pressure uncertainty), and in the reference sensor reflectance (including an inter-band calibration error). As in the other calibration methods, the RMS error is considered as an appropriate and realistic measure of performance.

Table 4.6 Typical error budget for the calibration method using desert sites.

Error Type	443	490	510	565	670	765	865
Surface reflectance model: 2%	1.23	1.53	1.73	2.08	2.10	2.28	2.06
Geometry	0.50	0.50	0.50	0.50	0.50	0.50	0.50
Surface pressure: 10 hPa	0.49	0.34	0.26	0.14	0.05	0.03	0.01
Gas amount: 20%	0.04	0.32	0.61	1.51	0.56	2.08	0.12
Aerosol content: 30% on τ_a	2.57	2.60	2.32	1.72	1.14	1.00	0.90
Aerosol model	2.87	1.60	1.01	0.05	0.60	0.86	1.01
Reference inter-band calibration	1.00	1.00	1.00	1.00	1.00	1.00	1.00
RMS	4.23	3.63	3.33	3.29	2.76	3.53	2.71
MAX	8.70	7.90	7.45	6.99	5.94	7.75	5.61

In general, the error budget, in terms of RMS, is about 3-4%. For longer wavelengths, the major source of error originates from the surface reflectance estimation because of limitations in the interpolation model or inter-band calibration error of the reference sensor. For shorter wavelengths, the error in the atmospheric contribution becomes the dominant factor.

For multi-temporal calibration purposes, the error budget is significantly improved, since the impact of errors affecting the estimation of surface reflectance, i.e., inter-band calibration of the RS and surface reflectance model, are strongly reduced. The accuracy of the method for multi-temporal calibration is nearly twice as good as for the red/near infrared bands. The improvement is not so important for shorter wavelengths, because other processes, mainly atmospheric contribution errors, are major factors.

4.5.2.5 Calibration algorithm and analysis

In the standard processing (Lachérade et al., 2013), the algorithm searches for each acquisition of the StC, all the measurements of the RS acquired for the same geometric conditions, i.e., same solar and viewing azimuth/zenith angles ± a given tolerance (typically 2° for zenith angles and 5° for relative azimuth angles). Reciprocal viewing conditions may be occasionally considered (Cabot et al., 1999) if it is required to extend the dataset when cross-calibrating sensors with very different acquisition geometries, for example when comparing MODIS-Aqua acquisitions near 13:30 UT with MODIS-Terra acquisitions near 10:30 UT. Nevertheless, the usually preferred alternative to enlarge matchups is to relax the criteria for the geometrical selection, i.e., 5° in zenith and 10° in azimuth (Lachérade et al., 2013). Note that the geometrical selection defined above does not imply simultaneity of both the StC and RS acquisitions. If the data archive of the RS covers many years, several reference acquisitions would be found, since the same geometric coincidence between StC and RS usually occurs every year. Consequently, for one acquisition of the StC, several acquisitions of the RS are usually selected as reference.

For each pair of measurements identified (i.e., a StC measurement and a RS measurement), the evaluation consists of comparing the normalized radiance measured by the StC (MI) with the TOA normalized radiance (CI) computed using Equation 4.6 with the surface reflectance estimated using the RS measurement obtained from Equation 4.8 as input. The ratio ΔA_k, defined by MI/CI, provides an estimation of the cross-calibration between the StC and the RS for each spectral band.

As is the case for all calibration methods, analyzing the sensitivity of results with input parameters can help to understand potential problems (see Lachérade et al., 2013). For example, strong variations with viewing zenith angles in the blue part of the spectrum may reveal atmospheric correction problems, i.e., an inaccurate representation of aerosol model and content. The multi-temporal analysis requires a regular temporal sampling over each site. Since for ocean-colour sensors the dynamic range is often dimensioned for clear atmosphere normalized radiances, a strong deviation of ΔA_k may suggest nonlinearity problems of the instrumental response (Fougnie et al., 2001; Hagolle and Cabot, 2006).

4.5.2.6 Application examples

Figure 4.9 illustrates the cross-calibration method for the MERIS and MODIS instruments. The ΔA_k coefficients for the 8 years of MERIS acquisitions were obtained using as reference 8 years of MODIS measurements. A very good consistency within 1-2% is found for 442, 560, 681 and 865 nm and RMS errors are in accordance with the error budget detailed in Section 4.5.2.4, i.e., about 4% in 442 nm, down to 2% in 865 nm. No significant variation is observed with the viewing zenith angle or other geometrical and geophysical parameters.

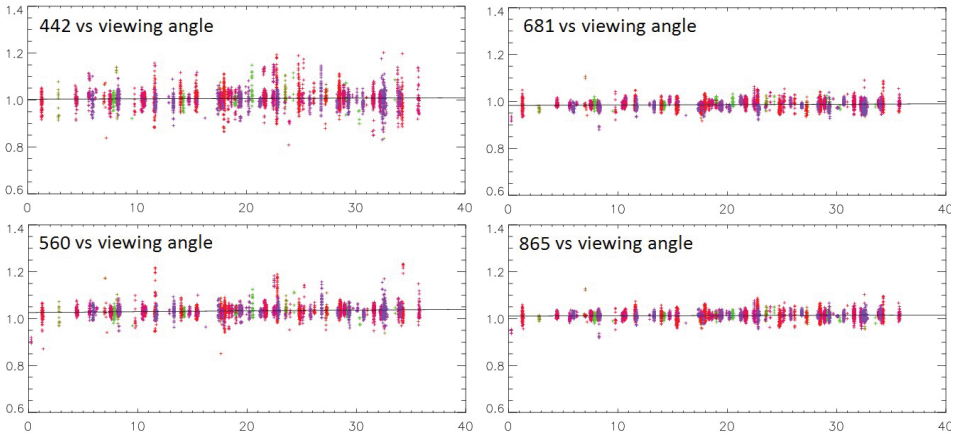

Figure 4.9 Cross-calibration of MERIS and MODIS instruments in the 442, 560, 681, and 865 nm MERIS spectral bands as a function of the zenith viewing angle. Measurements are MERIS acquisitions from May to December 2009 and reference data are MODIS acquisitions from April to May 2011.

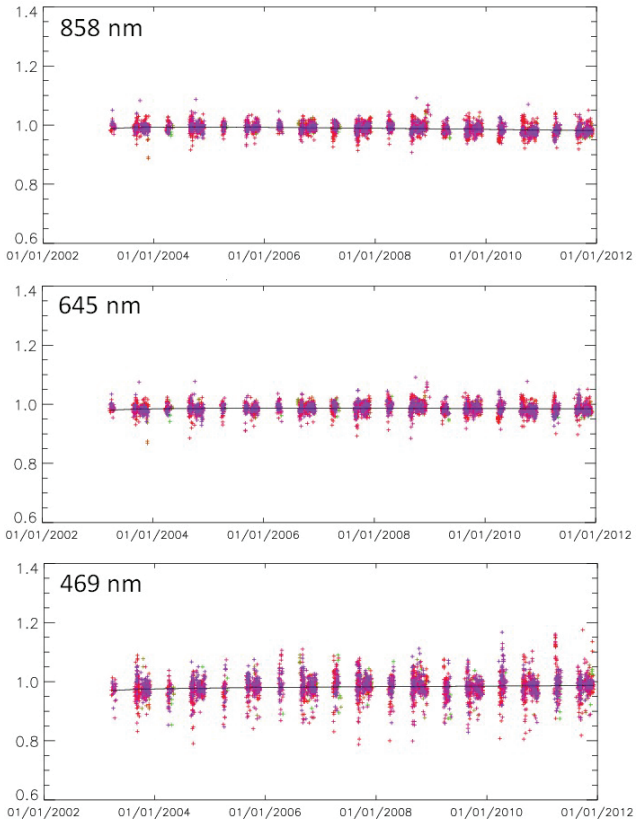

Figure 4.10 Multi-temporal calibration of MODIS using MERIS as reference, for spectral bands at 858, 645, and 469 nm.

Figure 4.10 shows the MODIS time series as observed over desert sites for the 469, 645, and 858 nm bands. Cross-calibration over desert sites is useful to validate the stability of the radiometry, and the MODIS time series does not show any significant evidence of temporal residual effects. Many cross-calibrations between various ocean-colour sensors have been elaborated and published in recent years. Cross-calibration of MERIS, MODIS, PARASOL, and SeaWiFS can be found in Lachérade et al. (2013) and Fougnie et al. (2012a; 2012b; 2013).

4.6 Absolute Calibration Using Sky Radiance and Solar Extinction

An absolute calibration method suitable for the red and infrared bands of ocean-colour sensors was proposed in Gordon and Zhang (1996) (see also Gordon, 1997; 1998). It involves making surface measurements of solar extinction and sky radiance at the time of satellite overpass. Using the algorithm developed by Wang and Gordon (1993) to estimate aerosol phase function and single scattering albedo, Gordon and Zhang (1996) showed that the top-of-atmosphere radiance can be predicted with an accuracy of 1-2% in the near infrared (if the surface radiometer is perfectly calibrated). They indicated "a reasonable calibration strategy in the near infrared is to place unattended sun photometer and sky radiometer units on small remote islands". A variant of this method was proposed in Santer and Martiny (2003). Instead of iterating directly over phase function and single scattering albedo, the measured sky radiance is first corrected for multiple scattering effects. The "pseudo" phase function, i.e., the product of phase function and single scattering albedo, is then obtained immediately using the primary scattering formulation. The process is repeated once to improve the correction of multiple scattering and, therefore, the determination of the "pseudo" phase function. Both studies concluded that the most important source of error in the prediction of the top-of-atmosphere radiance is the accuracy of the sky radiance.

4.6.1 Predicting TOA radiance

In the spectral range of interest, 700-900 nm, the diffuse reflectance of Case-I waters, i.e., waters whose optical properties are governed by their biogenic content, is practically null (Morel, 1988). When the surface winds are light (i.e., less than 7 m s^{-1}), the ocean surface is generally free of whitecaps, and their effect on surface reflectance is also negligible (Frouin et al., 1996; Gordon, 1997). In these conditions, the only contribution from the surface to the TOA radiance is due to Fresnel reflection. This contribution can be taken into account using the Cox and Munk (1954; 1955) model for isotropic wave-slope distribution, which depends on wind speed. Away from the direction of specular reflection, the satellite signal is

mostly atmospheric in nature, i.e., essentially composed of photons that have not interacted with the surface and water body, with contributions due to scattering by molecules (Rayleigh scattering) and aerosols.

An accurate radiative transfer code, such as the successive-order-of-scattering code of Deuzé et al. (1989), see also Lenoble et al. (2007), may be used to solve the radiation-transfer equation and predict the TOA radiance, L_{TOA}. This code has been compared with a Monte Carlo code (Santer et al., 2003), and the study has shown that agreement between the output of the two codes is within 1% over land and 1.2% over ocean. The input variables of the radiation transfer code to compute L_{TOA} are the aerosol optical thickness, the "pseudo" aerosol phase function, and the surface wind speed. The scattering properties of the aerosols may be obtained using solar extinction and sky radiance data from CIMEL radiometers of the Aerosol Robotic Network (AERONET) (Holben et al., 1998).

4.6.1.1 Solar extinction measurements

A basic description of the aerosols can be obtained from the solar extinction measurements. The solar irradiance $E(\lambda_i)$ measured in spectral band centred on λ_i can be related to the total optical thickness of the atmosphere, τ_{tot}, using the Langley-Bouguer law, that is:

$$E(\lambda_i) = E_0(\lambda_i)(d_0/d)^2 exp[-m\tau_{tot}(\lambda_i)], \tag{4.9}$$

where E_0 is the extra-terrestrial solar irradiance, d and d_0 the actual and mean Earth-Sun distance, respectively, and m the total air mass. Knowing the calibration coefficient E_0, the total optical thickness τ_{tot} can be derived from Equation 4.9. The aerosol optical thickness τ_a can be deduced from τ_{tot} by subtracting the ozone optical thickness τ_{O_3} and the Rayleigh optical thickness τ_r (obtained from the ozone content and the surface pressure, respectively), using:

$$\tau_a(\lambda_i) = \tau_{tot}(\lambda_i) - \tau_{O_3}(\lambda_i) - \tau_r(\lambda_i). \tag{4.10}$$

A dynamic Ångström coefficient $\alpha(\lambda_1, \lambda_2)$ between wavelengths λ_1 and λ_2 can be computed from $\tau_a(\lambda_i)$. It is defined as:

$$\alpha(\lambda_1, \lambda_2) = ln[\tau_a(\lambda_1)/\tau_a(\lambda_2))]/ln(\lambda_1/\lambda_2). \tag{4.11}$$

This coefficient characterizes the spectral dependency of τ_a, an indicator of size distribution and, therefore, aerosol type. However, $\alpha(\lambda_1, \lambda_2)$ is not sufficient to determine completely the aerosol type. Nevertheless, an aerosol model can be associated to $\alpha(\lambda_1, \lambda_2)$. Following the SeaWiFS and MODIS standard atmospheric correction algorithm (Gordon and Wang, 1994; Gordon, 1997), the aerosol model can be selected among candidates based on Shettle and Fenn (1979) data, namely Maritime, Coastal, Tropospheric, and Urban types with a relative humidity of 70, 90,

and 98%. Among these models, only the Urban type absorbs substantially. In the following, the candidate models will be referred to as, for example, M98 (Maritime model with a relative humidity of 98%), or T70 (Tropospheric model with a relative humidity of 70%).

Once the model is identified, its single scattering albedo and phase function are determined, and they can be used with the aerosol optical thickness derived from the extinction measurements as input variables to the radiation-transfer code to simulate the TOA radiance. This approach to calibration, however, depends critically on the set of aerosol models to choose from, and the set of models described above may not be realistic or appropriate to the problem, as documented in some studies (e.g., Gross-Colzy et al., 2003; Smirnov et al., 2003). More realistic models based on CIMEL measurements at AERONET coastal and island sites (Ahmad et al., 2010) may be used instead.

4.6.1.2 Sky radiance measurements

Another approach to simulate the TOA signal utilizes sky radiance measurements. In this method, proposed by Santer and Martiny (2003), no assumption on the aerosol model is required to obtain the phase function. The inversion scheme can be summarized as follows.

As the CIMEL radiometer measures the total downward radiance, we first correct the measured radiance from multiple scattering effects. We call f the corrective factor defined as:

$$f = [L^{(1)}/L]_{theo} \approx [L^{(1)}/L]_{meas}, \tag{4.12}$$

where $L^{(1)}$ and L stand respectively for the primary and total radiance in the atmosphere. Simulated $L^{(1)}$ and L are obtained using the radiation transfer code. The aerosol parameters used as first input to the code are τ_a and α derived from the CIMEL extinction measurements and the associated Junge size distribution $n(r)$ written as:

$$n(r) = Cr(^{\alpha-3}. \tag{4.13}$$

Once the measured principal plane radiance is corrected for multiple scattering effects, the primary scattering approximation for a homogeneous atmosphere is used, formalized as:

$$P' = 4L^{(1)} exp(\tau_{tot}/\mu_v)\left(1 - exp[-\tau_{tot}(1/\mu_s - 1/\mu_v)]^{-1}\right)[\mu_s/(\mu_s - \mu_v)]^{-1}, \tag{4.14}$$

where P' is the total "pseudo" phase function (molecules plus aerosols) and μ_v and μ_s are the cosine of the view and solar zenith angles, respectively. The total "pseudo" phase function P' is related to the "pseudo" phase function of the aerosols $\omega_a P_a$ via the following equation:

$$P' = (\omega_a \tau_a P_a + \tau_r P_r)/(\tau_a + \tau_r), \tag{4.15}$$

where ω_a and P_a are the single scattering albedo and phase function of the aerosols, respectively, and P_r is the phase function of the molecules. Knowing τ_{tot} from the extinction data and the geometrical conditions, $\omega_a P_a$ is easy to deduce from the primary scattering radiance $L^{(1)}$ previously derived from Equation 4.13.

The process is then iterated as follows. The parameter f is computed again using the radiation-transfer code, but with the $\omega_a P_a$ derived from Equations 4.14 and 4.15 (above) instead of the $\omega_a P_a$ computed from a Junge size distribution and a real refractive index of 1.45 (order zero). Equations 4.14 and 4.15 are then applied to get a new value of $\omega_a P_a$. The iterative process is stopped when f is stabilized to within less than 0.5%. Note that P' is required as input to the radiation-transfer code, not the individual terms on the right-hand side of Equation 4.15, but working with $\omega_a P_a$ provides for easier quality control of the results.

4.6.1.3 Error budgets on $F, \omega_a P_a$ and L_{TOA}

The radiance-based method described above relies on an iterative process to retrieve the aerosol "pseudo" phase function $\omega_a P_a$. According to Equation 4.14, the basic errors associated with $\omega_a P_a$ are due to errors in the parameter f, and in the extrapolation of the phase function to 180°, and to uncertainties linked to the calibration of the CIMEL radiometer, both in radiance and irradiance.

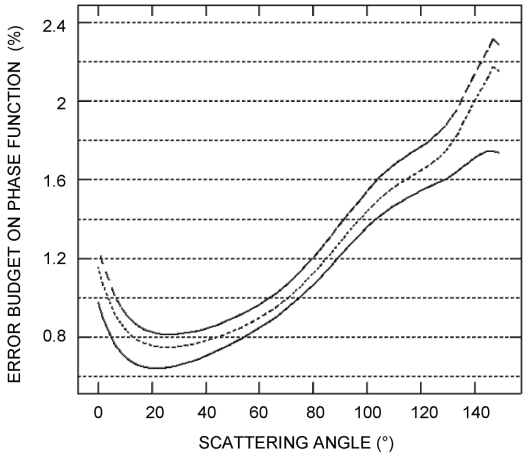

Figure 4.11 Error budget for the $\omega_a P_a$ product derived for the M90 model (solid line), the T90 model (dashed line), and the U90 model (micro-dashed line). The visibility is 23 km, the solar zenith angle 75°, the wind speed 7 m s^{-1} and the wavelength is 865 nm.

Figure 4.11 displays the error budget on $\omega_a P_a$ derived for the M90 model (solid line), the T90 model (dashed line), and the U90 model (micro-dashed line). The visibility is 23 km, the solar zenith angle is 75 degrees, and the wind speed is 7 m s^{-1}. Wavelength is 865 nm. The error increases with scattering angle in the backward scattering region, reaching 2.2% for the most absorbing model, U90, which is quite

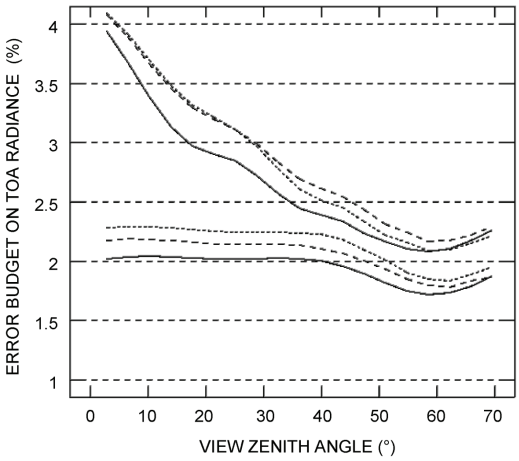

Figure 4.12 Error budget for L_{TOA} computed for the M90 model (solid line), the T90 model (dashed line), and the U90 model (micro-dashed line). The visibility is 23 km, the solar zenith angle 30° (upper plots) and 60° (lower plots), the relative azimuth angle 90°, and the wind speed 7 m s^{-1}.

satisfactory. Note that the individual errors on $\omega_a P_a$ are positive or negative, and therefore partly compensate.

In the error budget for L_{TOA} (Figure 4.12), we also have to account for uncertainties on wind speed and aerosol optical thickness separately. Simulations of L_{TOA} at 865 nm were performed for the same aerosol models as in Figure 4.11, a visibility of 23 km, two solar zenith angles (θ_0 of 30° and 60°), and an azimuth difference $\Delta\omega$ of 90°. The results, reported in Figure 4.12, indicate that the maximum error in L_{TOA} occurs in the case of a high solar elevation (θ_0=30°) and low viewing zenith angles. Nevertheless, even in that case, the error on L_{TOA} does not exceed 3.2% in the SeaWiFS geometry (θ from 20° to 70°). In an optimum case (θ_0=60°), the uncertainty related to L_{TOA} is in the order of 2% in the SeaWiFS geometry. In conclusion, the radiance-based method has a typical inaccuracy between 2 and 3% depending on solar zenith angle and sensor geometry.

Including typical errors due to atmospheric transmittance (0.6%), aerosol polarization (1%), and radiation-transfer model (1.2%), the error budget for L_{TOA} at 865 nm becomes 2.6 to 3.4%, depending on angular geometry. This error budget, however, does not take into account environmental effects, i.e., interactions between photons and the land surface, which may be significant for some coastal sites (see Schwindling et al., 1998 for a discussion of these effects).

4.6.2 Application to SeaWiFS calibration in the near infrared

This calibration method was applied to the calibration of SeaWiFS in the near infrared (band 8, centered on 865 nm, Martiny et al., 2005a). CIMEL data acquired at two locations were used, from a platform off Venice, Italy, and from a site on the west

coast of Lanai, near the MOBY buoy site. Environmental effects were not significant for the conditions selected for the study. Strict criteria were used to select SeaWiFS and CIMEL data acquired during the years 1999 and 2000 at the Venice site and during about 50 pre-selected days of the years 1998, 1999, and 2001 at the Lanai site. The first criterion is that SeaWiFS data must have scattering angles lower than 150° in order to match CIMEL sky-radiance measurements. The second criterion deals with the atmospheric stability in space for SeaWiFS imagery, and in time for CIMEL data. This resulted in 26 selected days for the calibration study: 19 for the Venice site and 7 for the Lanai site.

Table 4.7: Summary of calibration studies for the SeaWiFS and MERIS sensors.

Authors	**Method**	**Results**
Martiny et al., 2004	Simulations using CIMEL sky radiance measurements over ocean	MERIS: -0.8%
Antoine and Chami, 2004	Simulations using CIMEL extinction measurements over ocean	MERIS: +2.0%
Hagolle and Cabot, 2004	Sun glint method	MERIS: +1.6%
	Sensors inter-calibration with POLDER as a reference over desert targets	SeaWiFS/MERIS: -8.0%
Govaerts and Clerici, 2004	Sensors inter-calibration with SEVIRI/MSG as a reference over desert targets	SeaWiFS/MERIS: -7.3%
Nieke et al., 2004	Simulations using CIMEL measurements over snow targets	SeaWiFS/MERIS: -2.9%

Using for the analysis the days with at least two phase-function retrievals i.e., 20 out of 26 days, it was found that the SeaWiFS radiance in band 8, as provided by the NASA OBPG, was biased low by 7.0% ± 2.8% (Figure 4.13). No significant dependence on aerosol optical thickness and scattering angle was detected. These findings, instrument independent, were in agreement with results from calibration studies accomplished in the framework of the MERIS calibration/validation activities (Table 4.7).

The methodology presented above can also be applied to bands in the red as well as shorter wavelength bands, if the diffuse marine reflectance is known, or measured. It provides an alternative, purely radiometric, “vicarious” calibration to the “entire system” calibration (Evans et al., 1994; Franz et al., 2007) routinely performed by the NASA OBPG, which does not separate sensor from algorithms. However, as noted in Martiny et al. (2005b), it is difficult to retrieve the aerosol parameters in the visible using sky radiance measurements in the principal plane,

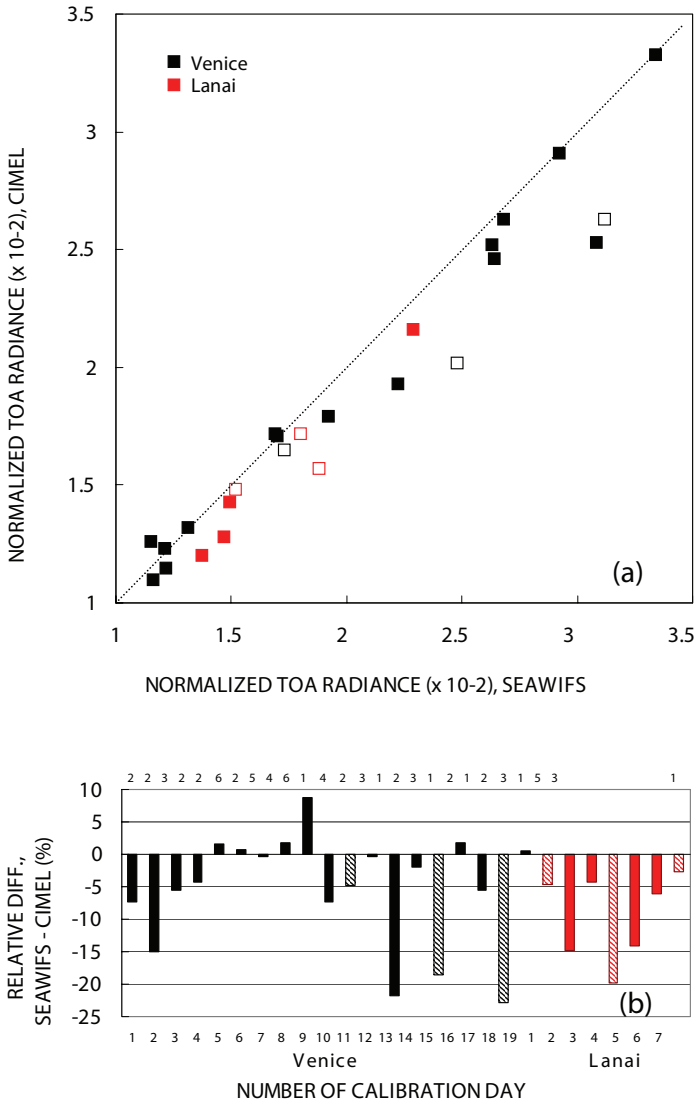

Figure 4.13 SeaWiFS radiometric calibration in the near infrared (band 8), for the 19 days selected for the Venice site and the 7 days selected for the Lanai site. (a) CIMEL retrieved TOA radiance versus SeaWiFS TOA measurements. (b) Relative difference between SeaWiFS measurements and CIMEL retrievals. Labels on the top represent the number of principal plane sets used for the computation of the TOA radiance (after Martiny et al., 2005a).

because of more important Rayleigh and surface contributions. A fairly automated radiometric calibration system based on the proposed methodology and exploiting the remote acquisition of CIMEL data from island and coastal sites around the globe, in particular the oceanic sites of the AERONET-OC network (Zibordi et al., 2009), might be envisioned. It would allow one to check and monitor operationally, at relatively low cost, the absolute calibration of satellite ocean-colour sensors, at least

in the red and near infrared where the ocean can be considered black, while they operate in orbit.

4.7 System Absolute Calibration

The required accuracy in water-leaving radiance for ocean biogeochemistry studies, i.e., ±5% absolute in the open ocean (see Chapter 2), is extremely demanding in terms of radiometric calibration, because the radiance measured from space at ocean-colour wavelengths may be 10 times larger than the water-leaving radiance (e.g., Gordon, 1987). Assuming perfect atmospheric correction, the absolute radiometric calibration of the satellite sensor must be accurate to a fraction of one percent. This is not achievable by the purely radiometric vicarious calibration methods described above, which are accurate to a few percent, at best, although statistically (i.e., through many realizations) a much better accuracy may be obtained. An in-orbit calibration strategy for achieving the required accuracy, originally developed for the Coastal Zone colour Scanner (CZCS) (Evans and Gordon, 1994), consists of comparing retrievals of water-leaving radiance with *in situ* measurements at the time of satellite overpass and adjusting the calibration coefficients to force agreement between retrieved and measured quantities (Gordon, 1998). This strategy, which aims at correcting for errors due to purely radiometric calibration techniques (after taking into account pre-launch instrument calibration/characterization, transfer to orbit, and temporal degradation) and for biases in the atmospheric correction algorithm, has been employed operationally for the processing of imagery from major satellite ocean-colour missions.

4.7.1 Method description

In this "system" vicarious calibration, the instrument is not considered separately from the atmospheric correction scheme, but part of the same system, because both are necessary for the retrieval of water-leaving radiance. For most ocean-colour sensors, two spectral bands in the near infrared are used to determine aerosol radiance and, therefore, perform atmospheric correction in the visible bands (Gordon, 1997). For example, they are centered at 765 and 865 nm for SeaWiFS, 748 and 869 nm for MODIS, and 779 and 865 nm for MERIS. The system vicarious calibration method assumes that the water body at the calibration site is black (null water-leaving radiance) and that the longer near infrared band is perfectly calibrated. The radiometric calibration in the shorter infrared band is then adjusted such that the expected aerosol model at the calibration site (Wang and Gordon, 2002) is retrieved correctly by the atmospheric correction scheme. Since this calibration is independent of the calibration in the visible bands, it does not need to be a known and stable aerosol type, low aerosol loading, and negligible water-leaving radiance in the near infrared. Two locations that fit the requirements are currently used

by the NASA OBPG to calibrate the shorter infrared bands of SeaWiFS and MODIS: the South Pacific Gyre and the Southern Indian Ocean (Franz et al., 2007). The assumed aerosol model at those locations is the maritime model of Shettle and Fenn (1979) with 90% relative humidity. Once the calibration in the near infrared bands is accomplished, the atmospheric correction scheme is operated on satellite imagery acquired over the calibration site to retrieve water-leaving radiance in the shorter, ocean-colour bands of the satellite sensor, and the retrievals are compared with *in situ* measurements. The calibration coefficients are finally adjusted to yield the expected water-leaving radiance.

The calibration site for the visible bands must ideally satisfy specific criteria (Gordon, 1998). Firstly, the aerosols (especially non absorbing) should be mostly of maritime origin with optical thickness below 0.1 in the visible (i.e., very clear atmosphere). In such situations, molecular scattering is the dominant process affecting the top-of-atmosphere radiance in the visible, reducing the impact of inherent uncertainties associated with the atmospheric correction scheme. Secondly, the water-leaving radiance should be uniform over the scale of several pixels, and the spatial contrast should be minimum over a distance of about 10–20 km to minimize adjacency effects. Thirdly, the water-leaving radiance should be as small as possible to reduce the effect of errors in the measured water-leaving radiance, i.e., the calibration site should be located in mesotrophic waters. Unfortunately, such waters often occur in coastal regions, where aerosols are likely to be absorbing and have an optical thickness above 0.1 in the visible, and where spatial variability in marine reflectance may be large. However, it was shown in recent works (Bailey et al., 2008; Mélin and Zibordi, 2010) that some criteria could be relaxed and still allow the required level of accuracy for TOA radiance.

In principle, any available water-leaving radiance data set collected during cruises in the world oceans, dedicated or opportunistic, could be used for the "system" calibration if the above criteria are met. One difficulty is managing and controlling quality of different data sets. It is desirable, however, to have long-term calibration sites, logistically attractive, where instrumentation can be properly maintained on a regular basis during the lifetime of a satellite mission. Such sites exist, where buoys with appropriate instrumentation have been deployed for many years, namely MOBY located off Lanai (Clark et al., 2003) and BOUSSOLE located in the northwestern Mediterranean Sea (Antoine et al., 2008). The optical mooring measurement program is complemented by regular cruises during which marine optical and biological properties are measured. Coastal CIMEL sun photometer stations provide information about aerosol properties. The sites only possess the first two desirable attributes, i.e., spatial homogeneity and relatively small aerosol influence. The clear waters make the accuracy requirement on water-leaving radiance challenging. The MOBY and BOUSSOLE sites have been operated systematically since 1997 and 2003, respectively, and the data have been adequate for system vicarious calibration of SeaWiFS, MODIS, and MERIS.

A basic assumption in the system vicarious calibration is that the pre-launch calibration of the longer near infrared band, after transfer to orbit, is correct. Wang and Gordon (2002) examined this assumption using simulated data and concluded that as long as the calibration error at 865 nm is less than 10% in magnitude, when aerosol optical thickness is moderate (less than 0.2 at 865 nm), the calibration in the visible bands remains sufficiently accurate. Eplee et al. (2001) confirmed this theoretical result by showing that, for SeaWiFS, changing the sensitivity by 5% at 865 nm would only require changing the sensitivity by 0.5% at 555 nm and 0.3% at 443 nm to restore agreement between satellite estimates of water-leaving radiance and measurements.

The "system" vicarious calibration is sensor independent (i.e., applicable to any ocean-colour sensor), but intimately linked to the atmospheric correction scheme. Therefore, if the scheme is altered, e.g., to account for new aerosol models, new calibration coefficients must consequently be used to maintain consistency. Other atmospheric schemes may proceed in different ways, and their application to Level 1b imagery is not straightforward, i.e., a specific system vicarious calibration is required beforehand. Furthermore, the calibration adjustments, which are dependent on atmospheric correction, are not expected to offset algorithm deficiencies over the entire range of oceanic and atmospheric conditions, especially in coastal regions and inland waters, since they are performed over open-ocean sites with typical maritime aerosols. These limitations notwithstanding, the system vicarious calibration method is suitable – and essential – to provide the required accuracy on water-leaving radiance for science applications in the vast majority of the world oceans.

4.7.2 Method accuracy

Uncertainties in the system vicarious calibration may be due to errors in the atmospheric correction algorithm, uncertainties in the near infrared calibration, uncertainties in the water-leaving radiance measurements, possible changes in the satellite sensor not captured during the transfer to orbit of the pre-launch calibration coefficients, and other factors, e.g., bi-directional effects in the water-leaving radiance, ignored or not properly taken into account. From various sensitivity studies, including global clear-water time series analysis, Eplee et al. (2001) concluded that the SeaWiFS gains obtained by the "system" calibration method applied at the MOBY site were accurate to 0.9% at 765 nm and 0.3% in the visible bands. Franz et al. (2007) performed a similar study with about 10 years of SeaWiFS data instead of a few years, showing that the vicariously adjusted gains were very stable during the first 10 years of the mission, with a standard deviation consistently at or below 1% at all wavelengths and an accuracy of about 0.1% on the mean values. They also investigated the change in vicarious gain with respect to sample size. Stabilization to within 0.1% of the 10-year averaged value was achieved with about 30, 40, and

30 samples at 443, 555, and 765 nm, respectively, and it took 2-3 years to obtain a sufficient number of samples at the MOBY site. This provides some indication of the number of satellite/surface match-ups and, therefore, the *in situ* measurement program required to reach adequate quality in remotely sensed water-leaving radiance via "system" vicarious calibration.

4.7.3 Application example

Figure 4.14 from Franz et al. (2007) illustrates the system vicarious calibration method. The results are for SeaWiFS, and they were obtained using screened SeaWiFS/MOBY match-ups during September 1997 to March 2006. The screening process was extensive, with strict criteria for the presence of clouds and their shadows, stray light, and whitecaps, variations in illumination conditions during the MOBY measurement cycle, navigation problems and atmospheric correction failure, within a 5 x 5 pixel box centered on the MOBY location. Consequently, only 10% (or 150 potential match-ups) passed the screening process.

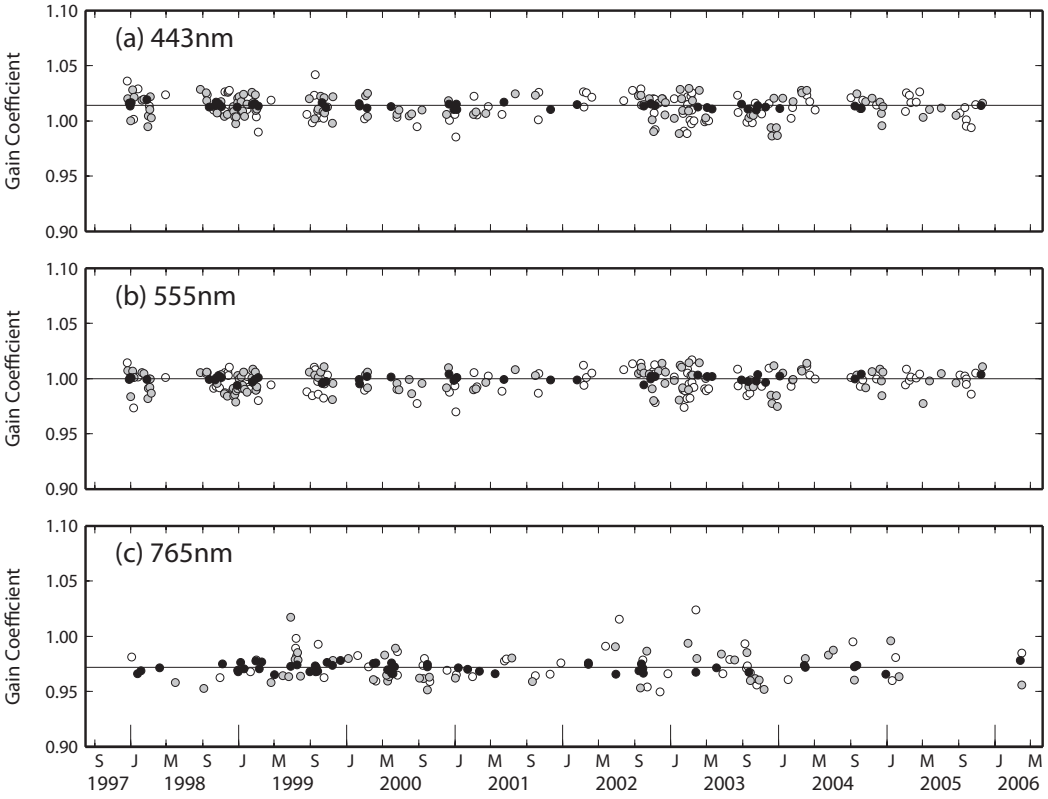

Figure 4.14 Ratio of sensor gains obtained after and before "system" vicarious calibration derived for SeaWiFS bands at 443, 555, and 765 nm based on match-ups acquired from September 1997 to March 2006. The filled circles are the gain ratios that passed the quality screening process (after Franz et al., 2007.)

The vicarious calibration adjustments are relatively small, i.e., 3.8% at 412 nm, decreasing progressively to 2.8% at 765 nm, with a standard deviation of about 1% about the mean values, i.e., within the uncertainty derived from the calibration transfer-to-orbit experiment (Barnes et al., 2000). No significant trends with solar and viewing zenith angles were detected. The adjustments are also stable with time, suggesting that temporal degradation is accounted for properly by the onboard lunar and solar calibrations (Barnes et al., 1999; 2001), and that the MOBY data are consistent over the 10-year time series.

4.8 Other Approaches

On-orbit radiometric cross-calibration of ocean-colour instruments is an important activity to ensure product consistency and generate climate data records. A better merging of the geophysical ocean-colour products would obviously require processing all the Level-1 data with the same algorithm applied to different sensors that have been cross-calibrated, meaning with a common reference to the same absolute radiometric calibration.

The cross-calibration process, i.e., relating the detector output of a sensor in a spectral band to the detector output of another sensor in a similar spectral band, requires measuring the same radiance. This is difficult to achieve when the two instruments are on different polar orbits, which is usually the case for global ocean-colour sensors. Apart from viewing the Moon, one has to rely on measuring the solar radiation reflected by the Earth-atmosphere system at the same time and location because of its variability. Moreover, the Earth-atmosphere system may have some bidirectional reflectance function that necessitates observing under the same solar and viewing geometry. Lastly, if the spectral bands of the measurements to be compared do not have the same or close definition, some empirical transformation has to be applied to make the comparison meaningful, thus the cross-calibration.

Bright surfaces, mostly arid deserts (e.g., Sahara) have been used to cross-calibrate satellite ocean-colour sensors with some success (see Section 4.5). The methodology assumes that the variations of the bidirectional reflectance of the surface with the viewing and solar geometry is accurately known, and that the atmosphere has a minimum influence. Moon calibration is about the same technique with the advantage of having no atmosphere interference, but this requires spacecraft manoeuvres in order to view the Moon (Eplee et al., 2009). Cao et al. (2004) suggested cross-calibrating the sensors over the polar regions by taking advantage of the multiple passes of a polar-orbiting platform at high latitude. This allows one to better meet the geometry and simultaneity requirements.

The cross-calibration results using the Moon obtained by Eplee et al. (2009) have shown that MODIS-Terra and -Aqua observations agree, band-to-band, at the 1-3% level, while SeaWiFS and MODIS agree at the 3-8% level. For ocean-colour products

generated from those instruments, however, the on-orbit "system" vicarious calibration mitigates the calibration biases, except in the 865 nm atmospheric correction band. The main implication of the study is that the number of lunar observations should be maximized during operational phase, and the phase angle range of the observations minimized.

Since ocean-colour remote sensing deals with a lower dynamics of the radiometry than over the land/ice surface or the Moon, using the highly reflecting targets of the desert, polar caps, and Moon for cross-calibration is not ideal, because of possible linearity and saturation problems. Waters at instrumented buoys like MOBY and BOUSSOLE (Clark et al., 1997; Antoine et al., 2006) and the "stable" waters in the center of the subtropical gyres (e.g., Hagolle et al., 1999) may be used as cross-calibration targets, but in this case most of the TOA radiance is due to atmospheric scattering, which strongly depends on geometry. Kwiatkowska et al. (2008) used observations over oligotrophic waters and clear atmospheres to cross-calibrate SeaWiFS and MODIS. MODIS-Terra on-orbit degradation, namely, changes in response versus scan angle (RVS) and polarization sensitivity, could not be tracked by on-board calibrators. The signal measured by MODIS at the TOA was thus modelled in the visible bands using the water-leaving radiance and aerosol optical parameters estimated by SeaWiFS, the sensor of reference. The approach proved effective to derive the RVS and polarization sensitivity of MODIS-Terra, and their trend over the mission life, allowing for significant improvement in the quality of MODIS-Terra ocean-colour products, especially in the blue where the degradation was the largest. The method was implemented operationally.

In-flight comparison between polar-orbiting sensors is limited by simultaneously viewing a location with the same geometry. The probability of such an event for sensors onboard platforms having different equatorial crossing times increases with latitude. It is nevertheless not very frequent over the polar region (Cao et al., 2004). Inter-calibrating two different geostationary sensors is even more difficult, or unfeasible, when their sub-satellite points are far away on the Equator. It is possible, however, to cross-calibrate ocean-colour sensors observing from different polar orbits using a geostationary sensor of reference, which acts as the intermediary between the ocean-colour sensors. Compared with other cross-calibration techniques, the advantage is that collocated coincidences in time and geometry are easier to find, i.e., more numerous, between the ocean-colour and reference sensors. Furthermore, many coincidences occur over oceanic regions, allowing the cross-calibration to be performed at radiance levels typically encountered in ocean-colour remote sensing.

Consider the cross-calibration of two polar-orbiting sensors using a geostationary sensor. Denoted by $\rho_{1i}(t)$ and $\rho_{2j}(t')$ the reflectance measured at time t by the first polar-orbiting sensor and t' by the second polar-orbiting sensor in spectral bands i and j, respectively, and by $\rho_{ref}(t)$ and $\rho_{ref}(t')$ the reflectance measured at t and t' by the geostationary sensor in a spectral band of reference. It is assumed here, for simplicity, that the polar-orbiting and geostationary sensors observe at exactly the

same time. Differences in observation time, generally small, can be accounted for in application. The cross-calibration coefficients between each polar-orbiting sensor and the geostationary sensor, A_{1i} and A_{2j}, can be written:

$$A_{1i} = \rho_{ref}(t)/f_{1i}[\rho_{1i}(t)] \tag{4.16}$$

$$A_{2j} = \rho_{ref}(t')/f_{2j}[\rho_{2j}(t')] \tag{4.17}$$

where f_{1i} and f_{2j} are empirical functions that relate ρ_{1i} and ρ_{2j} to ρ_{ref}. These functions are determined theoretically, from simulations for realistic environment and geometry conditions. If the two sensors are perfectly inter-calibrated, A_{1i} is equal to A_{2j}. Differences between A_{1i} and A_{2j}, on the other hand, will indicate that the calibration of the two sensors is not consistent and, therefore, needs to be adjusted accordingly. It is assumed, indeed, that the three sensors involved do not exhibit degradation or other changes between t and t'. The difference between these times, however, is expected to be small, i.e., a few hours.

Note that depending on the spectral band, the ρ_{ref} measurements may not be well correlated to ρ_1 and ρ_2 measurements in a single spectral band, but to measurements in several spectral bands. For example, the reference band of the geostationary sensor may contain several bands of sensors like MODIS or MERIS. The formalism remains the same, but Equations 4.16 and 4.17 become:

$$A_{1M} = \rho_{ref}(t)/f_{1M}[\rho_{1i}(t), i = 1, 2, ..., M] \tag{4.18}$$

$$A_{2M} = \rho_{ref}(t')/f_{2M}[\rho_{2j}(t'), j = 1, 2, ..., N] \tag{4.19}$$

where the empirical functions f_{1M} and f_{2N} now relate ρ_{ref} to a combination of measurements ρ_{1i} in M spectral bands and ρ_{2j} in N spectral bands. Consequently, differences between A_{1M} and A_{2N} will only be indicative of calibration inconsistencies in combination of spectral bands, not single bands. If not complete, this information is useful, and A_{1M} should be equal to A_{2N} in any calibration normalization.

Developing an efficient and accurate cross-calibration algorithm based on the polar-orbiting/geostationary methodology described above requires addressing a number of issues, namely surface target selection, solar and viewing geometry coincidence, and spectral band matching, and taking into account instrument characteristics and radiometric noise. It is desirable, for example, to observe ocean targets in backscattering conditions and avoid sun glint contamination. Since the tolerated difference in zenith angle is more restrictive (smaller) at large zenith angles, the selection may be limited to relatively low zenith angles. Note that observations along the same line of sight by the polar-orbiting and geostationary sensors are expected to occur near the Equator, the only region where the viewing azimuth angles would

match. Geometry coincidence would occur at higher latitudes if the polar-orbiting sensor measures at a tilted angle (as in the case of SeaWiFS). Imagers onboard current meteorological satellites in geostationary orbit may serve as reference, but the methodology has great potential in the future, in view of new geostationary sensors, which will have improved performance and characteristics, allowing a more accurate and complete cross-calibration of ocean-colour sensors.

Chapter 5

Recommendations

Robert Frouin, Steven Delwart, Bertrand Fougnie, Howard Gordon, Andreas Neumann, David Antoine, Pierre-Yves Deschamps, Cédric Fichot, Jean-Paul Huot and Mayumi Yoshida

A variety of techniques are available for checking the calibration of satellite ocean-color sensors after launch and maintaining the level of radiometric quality required for biogeochemistry applications during the entire operational phase of the missions. These techniques are diverse, based on different physical principles, and have different accuracies. They require onboard devices or spacecraft manoeuvres, utilize artificial or natural light sources, or exploit observations of suitable targets under specific conditions. Each technique may address a particular aspect of the calibration problem, such as absolute calibration, relative inter-band calibration, relative multi-temporal calibration, and sensor inter-calibration. Some techniques are generally applicable to all sensors, and others are sensor specific. For example inter-band calibration using sun glint or reflective clouds is not appropriate when the sensors saturate over those targets. Since calibration accuracy requirements are very demanding, i.e., a small fraction of one percent absolute, they should be carefully considered in the design of ocean-colour radiometers.

Any postlaunch calibration strategy or plan should take into consideration all the techniques available to bring about beneficial information regarding instrument radiometric performance. Redundancy in the techniques is not a luxury, but necessary to make sure that instrument changes are well understood and corrected adequately, and accuracies well established. Specific recommendations are given below.

- To achieve the uncertainty requirements for scientific applications, e.g., ±5% absolute in the blue and ±1% relative (i.e., band to band), or 30% on chlorophyll concentration, radiometric calibration should be accurate to a fraction of 1%. This is not achievable by standard, purely radiometric techniques, but the target accuracy by those techniques should be ±2%.
- Reflectance calibration has a number of advantages compared with radiance calibration and should therefore be performed preferentially. The solar constant does not need to be known, and it is much easier to do on-orbit reflectance

calibration than radiance calibration. But the bi-directional reflectance of the reference target should be monitored for stability. Furthermore, in the atmospheric correction process the molecular reflectance is given in look-up tables, and transforming this reflectance into radiance may greatly increase the error in water-leaving radiance.

- Sensors have non-ideal performance that must be understood. They should be fully characterized before launch for out-of-band response, polarization sensitivity, bright target/scattered light response, and non-linearity.
- Vicarious calibration or calibration adjustment is needed to meet accuracy objectives. "Radiometric" vicarious calibration techniques should be applied first, even though they may not be sufficient in terms of accuracy. "System" vicarious calibration, i.e., calibration of the sensor and the atmospheric correction algorithm, should be applied to refine the coefficients obtained by the "radiometric" vicarious techniques. In fact, "system" vicarious calibration is a complementary and fundamental part of the calibration process for any satellite ocean-colour mission.
- Calibration sites should be selected so that the satellite signal can be computed with the best accuracy possible, i.e., sufficiently far from land, in spatially homogenous oceanic regions, where the contribution of the ocean is as small as possible, where aerosol optical thickness is generally low and aerosols are not absorbing, and where cloud cover is favorable. Coastal sites are generally not adequate for vicarious calibration, although they are necessary for algorithm validation. Measurements of not only water-leaving radiance, but also aerosol optical properties and ancillary variables should be made at the calibration sites. Sites like MOBY and BOUSSOLE have sufficient attributes to achieve the calibration accuracy required for ocean-colour applications.
- Measurements at any suitable location (not only a few sites), collected with diverse instrumentation, should be considered in the check-of-calibration activities to ensure proper accuracy, provided they meet the strict calibration criteria. This would facilitate the acquisition of a sufficient number of match-ups to achieve convergence on calibration coefficients early in the mission operational phase.
- The data used by ocean-colour project offices for sensor calibration, including satellite radiance, water-leaving radiance, aerosol measurements, and ancillary measurements, should be made available to the ocean-colour community at large. This would allow investigators to perform their own calibration, using their own radiation transfer codes and atmospheric correction algorithms.
- For calibration, space agencies rely on schemes that differ, even when instruments are similar in concept and principle. Some resolution needs to occur. A common strategy should be devised and applied to all the sensors. Emphasis should be

placed on sensor inter-calibration to improve the spatial coverage of ocean-colour products and yield long-term consistent time series from multiple satellites, for climate studies.

Acronyms and Abbreviations

ADC	Analog-to-Digital Converter
ADEOS	Advanced Earth Observing Satellite (Japan)
AERONET	Aerosol Robotic Network
AOI	Angle of Incidence
AOT	Aerosol Optical Thickness
ATSR	Along Track Scanning Radiometer
AU	Astronomical Units
BOUSSOLE	Buoy for the acquisition of a long-term optical series (Mediterranean Sea)
BRDF	Bidirectional Reflectance Distribution Function
C	Chlorophyll concentration
CCD	Charge-Coupled Device
CI	Computed TOA normalized radiance or reflectance
CZCS	Coastal Zone Color Scanner
DCC	Deep Convective Clouds
GLI	Global Imager (Japan)
GOCI	Geostationary Ocean Colour Imager (Korea)
GOME	Global Ozone Monitoring Experiment
GSFC	Goddard Space Flight Center (NASA)
IAD	Ion-Assisted Deposition
IOCCG	International Ocean-Colour Coordinating Group
IS	Integrating Sphere
ISRO	Indian Space Research Organization
L_{TOA}	Top-of-atmosphere sensor radiance
MERIS	Medium Resolution Imaging Spectrometer (ESA)
METEOSAT	Meteorological Satellite
MI	Measured normalized radiance or reflectance
MISR	Multi-angle Imaging SpectroRadiometer (USA)
MOBY	Marine Optical Buoy
MODIS	Moderate Resolution Imaging Spectroradiometer (NASA)
MOS	Moderate Optoelectrical Scanner (Germany)
NASA	National Aeronautics & Space Administration
NIR	Near-Infrared
NIST	National Institute of Standards and Technology (USA)
NPL	National Physical Laboratory (UK)
OBPG	Ocean Biology Processing Group (NASA)

OCL	Offset Control Loop
OCM	Ocean Colour Monitor (India)
OCTS	Ocean Color and Temperature Scanner (Japan)
OLCI	Ocean and Land Colour Imager (ESA)
OMI	Ozone Monitoring Instrument
PARASOL	Polarization & Anisotropy of Reflectances for Atmospheric Sciences coupled with Observations from a Lidar (France)
PICS	Pseudo-Invariant Calibration Sites
POLDER	Polarization and Directionality of the Earth's Reflectances (CNES)
PTB	Physikalisch-Technische Bundesanstalt (Germany)
PTFE	polytetrafluoroethylene
RMS	Root-Mean-Squared
RS	Reference sensor
RSR	Relative Spectral Response
RVS	Response Versus Scan angle
ROLO	Robotic Lunar Observatory model (USGS)
SCIAMACHY	Scanning Imaging Absorption Spectrometer for Atmospheric Chartography
SeaWiFS	Sea-viewing Wide Field-of-view Sensor (NASA)
SMAC	Simplified Method for Atmospheric Corrections
SRCA	Spectro-Radiometric Calibration Assembly
StC	Sensor-to-calibrate
TNO	Dutch abbreviation for "Netherlands Organization for Applied Scientific Research"
TOA	Top of Atmosphere
TOMS	Total Ozone Mapping Spectrometer
TPD	TNO institute for applied physics
TV	Thermal Vacuum
VIIRS	Visible Infrared Imager Radiometer Suite
WMO	World Meteorological Organization

References

Ahmad, Z., B. A. Franz, C. R. McClain, E. J. Kwiatkowska, J. Werdell, E. P. Shettle, and B. N. Holben, New aerosol models for the retrieval of aerosol optical thickness and normalized water-leaving radiances from the SeaWiFS and MODIS sensors over coastal regions and open oceans, Appl. Opt., 49, 5545-5560, 2010.

Ainsworth, E., C. Pietras, and S. Bailey, Analysis of match-up results, in In situ aerosol optical thickness collected by the SIMBIOS program (1997-2000): Protocols, data QC, and analysis, G. S. Fargion, R. Barnes, and C. McClain, Eds., 73-87, (NASA Goddard Space Flight Center, Maryland), 2001.

Antoine, D., and M. Chami, Vicarious calibration of MERIS level-1b observations: early results obtained at the Villefranche AERONET site, Working meeting on MERIS and AATSR Calibration and Geophysical Validation (MAVT), ESRIN, Frascati, Italy, 20-24 October 2003, Proceedings on CD-rom, 2004.

Antoine, D., P. Guevel, J.-F. Desté, G. Bécu, F. Louis, A.J. Scott, and P. Bardey, The "BOUSSOLE" buoy A new transparent-to-swell taut mooring dedicated to marine optics: Design, tests and performance at sea, J. Atmos. Ocean. Technol., 25, 968-989, 2008.

Bailey, S. W., S. B. Hooker, D. Antoine, B. A. Franz, and P. J. Werdell, Sources and assumptions for the vicarious calibration of ocean color satellite observations, Appl. Opt., 47, 2035-2045, 2008.

Barnes, P. Y., E. A. Early, B. C. Johnson, J. J. Butler, C. J. Bruegge, S. Biggar, P. R. Spyak, and M. Pavlov, Intercomparisons of reflectance measurements, Proc. SPIE 3425, 1998.

Barnes, R. A., R. E. Eplee, Jr., S. F. Biggar, K. J. Thome, E. F. Zalewski, P. N. Slater, and A. W. Holmes, SeaWiFS transfer-to-orbit experiment, Appl. Opt., 39, 5620-5631- 2000.

Barnes, R. A., R. E. Eplee, F. S. Patt, H. H. Kieffer, T. C. Stone, G. Meister, J. J. Butler, and C. R. McClain, Comparison of SeaWiFS measurements of the Moon with the U. S. Geological Survey lunar model, Appl. Opt., 43(31),5838-5854, 2004.

Barnes, R. A., R. E. Eplee Jr., F. S. Patt, and C. R. McClain, Changes in the radiometric sensitivity of SeaWiFS determined from lunar and solar-based measurements, Appl. Opt., 38, 4649-4664, 1999.

Barnes R. A., R. E. Eplee, G. M., Schmidt, F. S., Patt and C. R. McClain, Calibration of SeaWiFS. I. Direct techniques, Appl. Opt., 40, 6682-6700, 2001.

Barnes, R. A., and F. Zalewski, Reflectance-based calibration of SeaWiFS: I. Calibration coefficients, Appl. Opt., 42, 1629-1647, 2003a.

Barnes, R. A., and F. Zalewski, Reflectance-based calibration of SeaWiFS: II. Conversion to radiance, Appl. Opt., 42, 1648-1660, 2003b.

Brown, S. W., NIST facility for spectral irradiance and radiance responsivity calibrations with uniform sources, Metrologia, 37, 579, 2003.

Bruegge, C., N. Chrien, and D. Haner, A Spectralon BRF database for MISR calibration applications. Remote Sens. Environ., 76, 354-366, 2001.

Bruegge, C. J., A. E. Stiegman, R. A. Rainen, and A. W. Springsteen, Use of Spectralon as a diffuse reflectance standard for in-flight calibration of Earth orbiting sensors, Opt. Eng., 32, 805-814, 1993.

Bruniquel, V., G. Fontanilles, L. Bourg, B. Fougnie, and P. Henry, Absolute calibration of SeaWiFS using Rayleigh scattering, International Ocean Colour Science Meeting, Darmstadt, Germany, 6-8 May, 2013.

Butler, J., P. Y. Barnes, E. A. Early, C. van Eijk-Olij, A. E. Zoutman, S. van Leeuwen, J. G. Schaarsberg, and H. Park, Comparison of ultraviolet Bi-directional Reflectance Distribution Function (BRDF) measurements of diffusers used in the calibration of the Total Ozone Mapping Spectrometer (TOMS), Proc. SPIE 4881, 2003.

Cabot, F., O. Hagolle, H. Cosnefroy, and X. Briottet, Inter-calibration using desertic sites as a reference target, Proc. IGARSS'98, 6-10 July, 5, 2713-2715, 1998.

Cabot, F., O. Hagolle, C. Ruffel, and P. Henry, Use of remote sensing data repository for in-flight calibration of optical sensors over terrestrial targets, Proc. of SPIE'99, Denver, CO, USA, July 1999.

Cao, C., M. Weinreb, and H. Xu, Predicting simultaneous nadir overpasses among polar-orbiting meteorological satellites for the inter-satellite calibration of radiometers, J. Atmos. Oceanic Technol., 21, 537-542, 2004.

Chang, R. Y., R. M. Huppe, C. Chase, and D. P. D'Amato, Optimization of Spectralon through numerical modeling and improved processes and designs, Proc. SPIE 6666, 2007.

Chen, H., and X. Xiong, MODIS solar diffuser stability monitor: Function and applications, Proc. SPIE 7452, 18-1, 2009.

Chen, H., X. Xiong, and A. Wu, Alternative Approach to Characterize Response versus Scan-angle (RVS) for MODIS Reflective Solar Bands, Proc. SPIE 8176, 12-1, 2011.

Chepfer, H., G. Brogniez, and Y. Fouquart, Cirrus clouds microphysical properties deduced from POLDER observations, J. Quant. Spectrosc. Radiat. Transf., 60, 375-390, 1998.

Chommeloux, B. G. Baudin, G. Gourmelon, J-L. Bézy , C. Van Eijk-Olij, J. Groote Schaarsberg, H. Werij, and E. Zoutman, Spectralon Diffusers used as in-flight optical calibration hardware, Proc. SPIE 3427, 382-393, 1998.

Clark, D. K., Phytoplankton Algorithms for the Nimbus-7 CZCS, in "Oceanography from Space", J. R. F. Gower, Ed., Plenum, New York, NY, 227-238, 1981.

Clarke, P. J., COOMET International comparison of relative reflectance standard, National Physics Laboratory Report, COEM 23, 1998.

Clark, D. K., M. A. Yarbrough, M. Feinholz, S. Flora, W. Broenkow, Y. S. Kim, B. C. Johnson, S. W. Brown, M. Yuen, and J. L. Mueller, MOBY, a radiometric buoy for performance monitoring and vicarious calibration of satellite ocean color sensors: measurement and data analysis protocols, in "Ocean Optics Protocols for Satellite Ocean Color Sensor validation", NASA Tech. Memo. 2003 - 211621/Rev4, VI, edited by J. L. Mueller, G. S. Fargion, and C. R. McClain, 139 pp., NASA GSFC, Greenbelt, Md, 2003.

Cosnefroy, H., X. Briottet, and M. Leroy, Characterization of desert areas with METEOSAT-4 data for the calibration of optical satellite sensors, Recent Advance in Sensors, Radiometric Calibration, and Processing of Remotely Sensed Data, Proc. SPIE, 1938, 203-211, 1993.

Cosnefroy, H., M. Leroy, and X. Briottet, Selection and characterization of Saharian and Arabian desert sites for the calibration of optical satellite sensors, Remote Sens. Environ., 58(1), 101-114, 1996.

Courreges-Lacoste, G. B., J. G. Schaarsberg, R. Sprik, and S. Delwart, Modeling of Spectralon diffusers for radiometric calibration in remote sensing, Opt. Eng., 42, 3600- 3607, 2003.

Cox, C., and W. Munk, Measurements of the roughness of the sea surface from photographs of the sun's glitter, J. Opt. Soc. Atm., 44, 838-850, 1954.

Cox, C., and W. Munk, Slopes of the sea surface deduced from photographs of the sun glitter, Bull. Scripps Inst. Ocean., 6, 401-488, 1955.

Dainty, J. C., Laser Speckle and Related Phenomena, Springer-Verlag, Berlin, Heidelberg, New York, 1975.

Datla, R. U., J. P. Rice, K. Lykke, B. C. Johnson, J. J. Butler and X. Xiong, Best practice guidelines for pre-Launch characterization and calibration of instruments for passive optical remote Sensing report to Global Space-based Inter-Calibration System (GSICS) Executive Panel, NOAA/NESDIS, World Weather Building, Camp Springs, Maryland 20746, September 2009.

Delwart, S., and L. Bourg, MERIS calibration: 7th Year in space, Proc. SPIE 7474, 30, 2009.

Delwart, S., and L. Bourg, Radiometric calibration of MERIS, Proc. SPIE 8176, 13-1 to 13-10, 2011.

Delwart, S. and R. Preusker, L. Bourg, and R. Santer, MERIS spectral calibration campaigns, Proc. SPIE V5570, 381-390, 2004.

Delwart, S., R. Preusker, L. Bourg, R. Santer, D. Ramon, and J. Fischer, MERIS in-flight spectral calibration Int. J. Remote Sens., 28, 479-496, 2007.

Deuzé, J.-L., M. Herman, and R. Santer, Fourier series expansion of the transfer equation in the atmosphere-ocean system, J. Quant. Spectrosc. Radiat. Transfer, 41, 483-494, 1989.

Dinguirard, M., and P. N. Slater, Calibration of space-multispectral imaging sensors: A review, Remote Sens. Environ., 68, 194-205, 1999.

Dubuisson P., R. Borde, D. Desailly, and R. Santer, In-flight spectral calibration of the oxygen-A band channel of MERIS, Int. J. Remote Sens., 24, 1177-1182, 2003.

Early, E. A., P. Y. Barnes, B. C. Johnson, J. J. Butler, C. J. Bruegge, S. F. Biggar, P. S. Spyak, and M. M. Pavlov, Bidirectional reflectance round robin in support of the Earth observing system program, J. Atmos. Ocean. Technol., 17, 1077-1091, 2000.

Eplee, R. E., Jr., R. A. Barnes, F. S. Patta, G. Meister, and C. R. McClain, SeaWiFS lunar calibration methodology after six years on orbit. Proc. SPIE, 5542, doi:10.1117/12.556408, 2004.

Eplee, R. E. Jr., F. S. Patt, R. A. Barnes, and C. R. McClain, SeaWiFS long-term solar diffuser reflectance and sensor noise analysis, Appl. Opt., 46(5), 762-773, 2007.

Eplee, R. E., Jr., W. D. Robinson, S. W. Bailey, D K. Clark, P. J. Werdell, M. Wang, R. A. Barnes, and C. R. McClain, Calibration of SeaWiFS. II. Vicarious techniques, Appl. Opt., 40, 6701-6717, 2001.

Eplee, R. E., J. Sun, G. Meister, F. S. Patt, T. C. Stone, X. Xiong and C. R. McClain, Cross Calibration of SeaWiFS and MODIS Using On-Orbit Observations of the Moon, Appl. Opt., 50(2),120-133, 2011.

Eplee, R. E. Jr., K. R. Turpie, G. F. Fireman, G. Meister, T. C. Stone, F. S. Patt, B. A. Franz, S. W. Bailey and C. R. McClain, VIIRS on-orbit calibration for ocean color data processing, in Earth Observing Systems XVII, J. J. Butler, X. Xiong,and X. Gu, eds. Proc. SPIE 8510, 85101H, 2012.

Eplee, R. E., X. Xiong, J.-Q Sun, G. Meister, and C. R. McClain, The cross-calibration of SeaWiFS and MODIS using on-orbit observations of the moon, Proc. SPIE 7452, 74520X, doi: 10.1117/12.825160, 2009.

Evans, R. H., and H. R. Gordon, Coastal Zone Color Scanner system calibration: A retrospective examination, J. Geophys. Res., 99, 7293-7307, 1994.

Feng, X., J. R. Schott, and T. Gallagher, Comparison of methods for generation of absolute reflectance-factor values for bidirectional reflectance-distribution function studies, Appl. Opt., 32, 1234-1242, 1993.

Flasse, S. P., M. M. Verstraete, B. Pinty, and C. J. Bruegge, Modeling Spectralon's bidirectional reflectance for in-flight calibration of Earth-orbiting sensors, Proc. SPIE 1938, 100-108, 1993.

Fougnie, B., and R. Bach, Monitoring of radiometric sensitivity changes of space sensors using Deep Convective Clouds - Operational application to PARASOL, IEEE Trans. Geosci. Remote Sens., 47(3), 851-861, 2009.

Fougnie, B., G. Bracco, B. Lafrance, C. Ruffel, O. Hagolle, and C. Tinel, An overview of PARASOL in-flight calibration and performance, Appl. Opt., 46(22), 5,435-5,451, 2007.

Fougnie, B., F. Cabot, O. Hagolle, and P. Henry, CNES Contribution to Ocean Color Calibration: Cross-calibration over Desert Sites, SIMBIOS Project 2001 Annual Report, NASA/TM-2002-210005, 159-163, 2002a.

Fougnie, B., P.-Y. Deschamps, and R. Frouin, Vicarious calibration of the POLDER ocean color spectral bands using in-situ measurements, IEEE Trans. Geosci. Remote Sens. 37, 1576-1574, 1999.

Fougnie, B., O. Hagolle, and F. Cabot, In-flight measurement and correction of nonlinearity of the POLDER-1's sensitivity, 8th Symposium of the International Society for Photogrammetry and Remote Sensing, Aussois, France, 8-12 January, 2001.

Fougnie B., P. Henry, S. Lachérade, P. Gamet, D. Jolivet, B. Lafrance, V. Bruniquel, G. Fontanilles, L. Bourg, and L. Gross-Colzy, In-flight calibration of space sensors through common statistical vicarious methods: Toward an ocean color virtual constellation, Ocean Optics XXI, Glasgow, Scotland, 8-12 October, 2012a.

Fougnie B., P. Henry, S. Lachérade, C. Miquel, and L. Bourg, Validation of the MERIS 3rd reprocessing Level-1 calibration through various vicarious approaches - Perspectives for OLCI,Sentinel-3 OLCI/SLSTR and MERIS/AATSR Workshop, Frascati, Italy, 15-19 October, 2012b.

Fougnie, B., P. Henry, A. Morel, D. Antoine, and F. Montagner, Identification and characterization of stable homogeneous oceanic zones : Climatology and impact on inflight calibration of space sensor over Rayleigh scattering, Proc. Ocean Optics XVI, Santa Fe, New Mexico, 18-22 November, 2002b.

Fougnie, B., S. Lachérade, P. Henry, P. Gamet, V. Bruniquel, and G. Fontanilles, MODIS-AQUA calibration over various natural targets - What can be learned from alternative statistical approaches?, Proceedings CALCON'13 Meeting, Logan, Utah, August 26-29, 2013.

Fougnie B., J. Llido, L. Gross-Colzy, D. Blumstein, and P. Henry, Climatology of oceanic zones suitable for in-flight calibration of space sensors, Earth Observing Systems XV, SPIE Optics and Photonics, San Diego, California, 1-5 August, 2010.

Franz, B. A., S. W. Bailey, P. J. Werdell, and C. R. McClain, Sensor-independent approach to the vicarious calibration of satellite ocean color radiometry, Appl. Opt., 46, 5068-5082, 2007.

Franz, B. A., E. J. Kwiatkowska, G. Meister and C. R. McClain, Moderate Resolution Imaging Spectrometer on Terra: limitations for ocean color applications, J. Appl. Remote Sens., 2, 023525, 2008.

Frouin, R., M. Schwindling, and P.Y. Deschamps, Spectral reflectance of sea foam in the visible and near infrared: in-situ measurements and remote sensing implications, J. Geophys. Res., 101, 14361-14371, 1996.

Garver, S., and D. Siegel, Inherent optical property inversion of ocean color spectra and its biogeochemical interpretation: 1 time series from the Sargasso Sea, J. Geophys. Res., 102C, 18607-18625, 1997.

Georgiev, G. T., and J. J. Butler, BRDF study of gray-scale Spectralon, Proc. SPIE 7081, 7081, 07-5, 2008.

Georgiev, G. T., and J. J. Butler, The effect of speckle on BRDF measurements, Proc. SPIE 5882, 2005.

Gordon, H. R., Atmospheric correction of ocean color imagery in the Earth observing system era, J. Geophys. Res., 102D, 17081-17106, 1997.

Gordon, H. R., Calibration requirements and methodology for remote sensors viewing the oceans in the visible, Remote Sens. Environ., 22:103-126. 1987.

Gordon, H. R., In-orbit calibration strategy for ocean colour sensors, Remote Sen. Environ., 63, 265-278, 1998.

Gordon, H. R., Remote sensing of ocean color: a methodology for dealing with broad spectral bands and significant out-of-band response, Appl. Opt., 34, 8363-8374, 1995.

Gordon, H. R., and D. K. Clark, Clear water radiances for atmospheric correction of Coastal Zone Color Scanner imagery, Appl. Opt., 20, 4175-4180, 1981.

Gordon, H. R., and A. Morel, Remote Assessment of Ocean Color for Interpretation of Satellite Visible Imagery: A Review, Springer-Verlag, New York, 114, 1983.

Gordon, H. R., and M. Wang, Retrieval of water-leaving radiance and aerosol optical thickness over the oceans with SeaWiFS: A preliminary algorithm, Appl. Opt., 33, 443-452, 1994.

Gordon, H. R., and T. Zhang, How well can radiance reflected from the ocean atmosphere system be predicted from measurements at the surface, Appl. Opt., 35, 6527- 6543, 1996.

Gordon, H. R., J. W. Brown, and R. H. Evans, Exact Rayleigh scattering calculations for use with the Nimbus-7 Coastal Zone Color Scanner, Appl. Opt., 27, 862-871, 1988.

Gordon, H. R., D. K. Clark, J. W. Brown, O. B. Brown, R. H. Evans, and W. W. Broenkow, Phytoplankton pigment concentrations in the middle Atlantic Bight: Comparison of ship determinations and Coastal Zone Color Scanner measurements, Appl. Opt., 22, 20-36, 1983.

Gordon, H. R., T. Du, and T. Zhang, Atmospheric correction of ocean color sensors: Analysis of the effects of residual instrument polarization sensitivity, Appl. Opt., 36, 6938-6948, 1997.

Govaerts, Y. M., and M. Clerici, Comparison of MSG/SEVIRI calibration reference with MERIS BRF over bright desert calibration targets, Working meeting on MERIS and AATSR Calibration and Geophysical Validation (MAVT), ESRIN, Frascati, Italy, 20-24 October 2003, Proceedings on CD-rom, 2004.

Gross-Colzy, L., R. Frouin, C. M. Pietras, and G. S. Fargion, Non-supervised classification of aerosol mixtures for ocean color remote sensing, in Ocean Remote Sensing and Applications, R. Frouin, Y. Yuan, and H. Kawamura, Eds, Proc. SPIE 4892, 95-104, 2003.

Guenther B., W. Barnes, E. Knight, J. Barker, J. Harnden, R. Weber, M. Roberto, G. Godden, H. Montgomery, and P. Abel, MODIS Calibration: A brief review of the strategy for at-launch calibration approach, J. Atmos. Ocean. Tech., 13 274-285,1996.

Hagolle, O., and F. Cabot, Absolute calibration of MERIS using natural targets, Working meeting on MERIS and AATSR Calibration and Geophysical Validation (MAVT), ESRIN, Frascati, Italy, 20-24 October 2003, Proceedings on CD-rom, 2004.

Hagolle, O., and F. Cabot, Calibration of MERIS using natural targets, Second MERIS and AATSR Calibration and Geophysical Validation Workshop, Frascati, 20-24 March, 2006.

Hagolle, O., P. Goloub, P.-Y Deschamps, H. Cosnefroy, X Briottet, T. Bailleul, J.-M. Nicolas, F. Parol, B. Lafrance, and M. Herman, Results of POLDER in-flight calibration, IEEE Trans. Geosci. Remote Sens., 37(7), 1550-1566, 1999.

Hagolle, O., J.-M. Nicolas, B. Fougnie, F. Cabot, and P. Henry, Absolute calibration of VEGETATION derived from an interband method based on the sun glint over ocean, IEEE Trans. Geosci. Remote Sens., 42, 1472-1481, 2004.

Haner, D., B. T. McGuckin, and C. J. Bruegge, Polarization characteristics of Spectralon illuminated by coherent light, Appl. Opt., 38, 6350-6356, 1999.

Henry, P., G. Chander, B. Fougnie, C. Thomas, and X. Xiong, Assessment of spectral bands impact on inter-calibration over desert sites using simulation based on EO-1 Hyperion data, IEEE Trans. Geosci. Remote Sens., Special Issue on Inter-Calibration, 51(3) 1297-1308, 2013.

Holben, B., T. Eck, I. Slutsker, D. Tanré, J.-P. Buis, A. Setzer, E. Vermote, J. Reagan, Y. Kaufman, T. Nakajima, F. Lavenu, I. Jankowiak, and A. Smirnov, A federated instrument network and data archive for aerosol characterization, Remote Sens. Environ., 66, 1-16, 1998.

IOCCG, Remote Sensing of Inherent Optical Properties: Fundamentals, Tests of Algorithms and Applications, Lee, Z.-P. (ed.), Reports of the International Ocean Color Coordinating Group, No. 5, IOCCG, Dartmouth, Canada, 2006.

IOCCG, Mission Requirements for Future Ocean-Colour Sensors, McClain, C. and G. Meister (eds.), Reports of the International Ocean-Colour Coordinating Group, No. 13, IOCCG, Dartmouth, Canada, 2012.

Kang, G., P. Coste, H. Youn, F. Faure, and S. Choi, An in-orbit radiometric calibration method of the Geostationary Ocean Color Imager, IEEE Trans. Geosci. Remote Sens., 48, 4322-4328, 2010.

Kieffer, H. H., Photometric stability of the lunar surface, Icarus, 130, 323-327, 1997.

Kieffer, H. H., and T. C. Stone, The spectral irradiance of the moon, Astron. J., 129: 2887-2901, 2005.

Krause, K., S. Biggar, K. Thome, J. Eagen, and D. Kenyon, On-orbit radiometric calibration using a solar diffuser, Proc. SPIE 4483, 135-145, 2002.

Kwiatkowska, E. J., B. A. Franz, G. Meister, C. R. McClain, and X. Xiong, Cross calibration of ocean color bands from Moderate Resolution Imaging Spectroradiometer on Terra platform. Appl. Opt., 47: (36) 6796-6810, 2008.

Lachérade, S., B. Fougnie, P. Henry, and P. Gamet, Cross-calibration over desert sites: Description, methodology, and operational implementation, IEEE Trans. Geosci. Remote Sens., Special Issue on Inter-Calibration, 51(3), 1098-1113, 2013.

Lafrance, B., O. Hagolle, B. Bonnel, Y. Fouquart, G. Brogniez, and M. Herman, Interband calibration over clouds for POLDER space sensor, IEEE Trans. Geosci. Remote Sens., 40, 131-142, 2002.

Leland, J. E., and A. V. Arrechi, Phase 2 analysis of Spectralon material for use in onboard calibration systems for the medium-resolution imaging spectrometer (MERIS), Proc. SPIE 2475, 384-392, 1995.

Lenoble, J., M. Herman, J.L. Deuzé, B. Lafrance, R. Santer, and D. Tanré, A successive order of scattering code for solving the vector equation of transfer in the Earth's atmosphere with aerosols, J. Quant. Spectrosc. Radiat. Transfer, 107, 479-507, 2007.

Maritorena, S., D. A. Siegel, and A. R. Peterson, Optimization of semi-analytical ocean color model for global scale applications, Appl. Opt., 41, 2705-2714, 2002.

Martiny, N., R. Frouin, and R. Santer, Radiometric calibration of SeaWiFS in the near infrared, Appl. Opt. 44(36), 7828âĂŞ7844, 2005a.

Martiny, N., R. Santer, and I. Smolskaia, Vicarious calibration of MERIS over dark water in the near infrared, Remote Sens. Environ., 94(4), 475-490, 2005b.

McClatchey, R. A., R. W. Fenn, J. E. A. Shelby, F. E. Voltz, and J. S. Garing, Optical properties of the atmosphere, Tech. Rep. AFCRL-72-0497, Hanscom AirForce Base, Bedfort, MA, 1972.

Meister, G., B. A. Franz, E. J. Kwiatkowska, and C.R. McClain, Corrections to the calibration of MODIS Aqua ocean color bands derived from SeaWiFS data, IEEE Trans. Geosci. Remote Sens., 50(1), 310-319, 2012.

Meister, G., J. Sun, R. E. Jr. Eplee, F. S. Patt, X. Xiong, and C. R. McClain, Proc. SPIE, 7081, 70810D, 2008.

Mélin, F., and G. Zibordi, Vicarious calibration of satellite ocean color sensors at two coastal sites, Appl. Opt., 49, 798-810, 2010.

MERIS Team, MERIS Detailed processing model, PO-TN-MEL-GS-0002, 2011. Available at: https://earth.esa.int/pub/ESA_DOC/ENVISAT/MERIS/Meris_DPM_L1b_i8r0.pdf.

Miesch, C., F. Cabot, X. Briottet, and P. Henry, Assimilation method to derive spectral ground reflectance of desert sites from satellite datasets, Remote Sens. Environ., 87(2-3), 359-370, 2003.

Montgomery, H., N. Che, K. Parker, and J. Bowser, The algorithm for MODIS wavelength on-orbit calibration bands using the SRCA, IEEE Trans. Geosci. Remote Sens., 38(2), 877-884, 2000.

Morel, A., Optical modelling of the upper ocean in relation to its biogenous matter content (case 1 water), J. Geophys. Res., 93, 10749-10768, 1988.

Morel, A., and B. Gentili, Diffuse reflectance of oceanic waters (2): Bi-directional aspects., Appl. Opt., 32, 6864-6879, 1993.

Neckel, H., and D. Labs, The solar radiation between 3300 and 12500 Å, Solar Physics 90(2), 205-258, 1984.

Neumann, A., Calibration of ocean-color sensors, IOCCG Training Course in "Remote Sensing of Ocean Color", Ahmedabad, India, February 2001.

Nicodemus, F. E., J. C. Richmond, J. J. Hsia, I. W. Ginsburg, and T. Limperis, Geometrical considerations and nomenclature for reflectance, National Bureau of Standards Monograph, 160, 1977.

Nieke, J., M. Hori, R. Höller, and I. Asanuma, Satellite sensor inter-calibration: a case study for 28 March 2002, Working meeting on MERIS and AATSR Calibration and Geophysical Validation (MAVT), ESRIN, Frascati, Italy, 20-24 October 2003, Proceedings on CD-rom, 2004.

Petroy, S. B., J. E. Leland, B. Chommeloux, C. J. Bruegge, and G. Gourmelon, Phase 1 analysis of Spectralon material for use in on-board calibration systems for the medium resolution imaging spectrometer (MERIS), Proc. SPIE 2210, 616-624, 1994.

Proctor, J. R., and P. Y. Barnes, NIST High accuracy reference reflectometer spectrophotometer, J. Res. Nat. Inst. Stand. Technol., 101, 619-62,1996.

Rahman, H., and G. Dedieu, SMAC: a simplified method for the atmospheric correction of satellite measurements in the solar spectrum, Int. J. Remote Sens., 15, 123-143, 1994.

Rahman, H., M. M. Verstraete, and B. Pinty, Coupled surface-atmosphere reflectance (CSAR) model. 1. Model description and inversion on synthetic data, J. Geophys. Res., 98, 20779-20789, 1993.

Rast, M., J.-.L Bezy, and S. Bruzzi, The ESA Medium Resolution Imaging Spectrometer MERIS a review of the instrument and its mission, Int. J. Remote Sens., 20, 1681-1702, 1999.

Santer, R., and N. Martiny, Sky radiance measurements for ocean-colour calibration validation, Appl. Opt., 42, 896-907, 2003.

Santer, R., F. Zagolski, and E. Dilligeard, Radiative transfer code comparison for MERIS vicarious calibration, Envisat Validation Workshop, ESRIN, Frascati, Italy, 9-13 December 2002, Proceedings on CD-rom, 2003.

Schiff, T. F., M. W. Knighton, D. J. Wilson, F. M. Cady, and J. C. Stover, Design review of a high accuracy UV to near IR scatterometer, Proc. SPIE 1995, 121-123, 1993.

Schwindling, M., P.-Y. Deschamps, and R. Frouin, Verification of aerosol models for satellite ocean color remote sensing, J. Geophys. Res., 103, 24919-24935, 1998.

Shettle, E. P., and R. W. Fenn, Models of the aerosols of the lower atmosphere and the effects of humidity variations on their optical properties, Technical Report 0214 (Air Force Geophysical Laboratory, Hanscom Air Force Base, Mass., 1979.

Slater, P. N., S. F. Biggar, J M. Palmer, and K. J. Thome, Unified approach to pre- and in-flight satellite-sensor absolute radiometric calibration, Proc. SPIE 2583, 130, 1995.

Smirnov, A., B. N. Holben, O. Dubovik, R. Frouin, T. F. Eck, and I. Slutsker, Maritime component in aerosol optical models derived from AERONET (Aerosol Robotic Network) data, J. Geophys. Res., 108, 4033, doi:10.1029/2002JD002701, 2003.

Smorenburg, C., A. L. G. van Valkenburg, and H. G. C. Werij, Absolute radiometric calibration facility, Proc. SPIE 2583, 166, 1995.

Stamnes, K., S. C. Tsay, W. Wiscombe, and K. Jayaweera, Numerically stable algorithm from discrete - ordinate - method radiative transfer in multiple scattering and emitting layered media, Appl. Opt., 12, 2502-2509, 1988.

Stephens, G. L., Radiation profiles in extended water clouds - Part I: Theory, J. Atmos. Sci., 35, 2111-2122, 1978.

Stiegman, A. E., C. J. Bruegge, and A. W. Springsteen, Ultraviolet stability and contamination analysis of Spectralon diffuse reflectance material, Opt. Eng., 32, 799-804, 1993.

Stone, T. S. and H. H. Kieffer, Assessment of uncertainty in ROLO lunar irradiance for on-orbit calibration, Proc. SPIE, 5542, 300-310, 2004.

Sun, J.-Q., X. Xiong, and W. L. Barnes, MODIS solar diffuser stability monitor sun view modeling, IEEE Trans. Geosci. Remote Sens., 4, 1845-1854, 2005.

Sun, J.-Q., X. Xiong, W. L. Barnes, and B. Guenther, MODIS reflective solar bands on-orbit calibration, IEEE Trans. Geosci. Remote Sens., 45, 2383-2393, 2007.

Sun, J.-Q., X. Xiong, and B. Guenther, MODIS solar diffuser stability monitor performance, Proc. SPIE 4483, 2002.

Thuillier, G., M. Hersé, D. Labs, T. Foujols, W. Peetermans, D. gillotay, P. C. Simon, and H. Mandel, The solar spectral irradiance from 200 to 2400 nm as measured by the SOLSPEC spectrometer from the Atlas and Eureca missions, Solar Phys., 214, 1-22, 2003.

Toubbé, B., T. Bailleul, J.L. Deuzé, P. Goloub, O. Hagolle, and M. Herman, In-flight calibration of the POLDER polarized channels using the Sun's glitter, IEEE Trans. Geosci. Remote Sens., 37, 513-525, 1999.

Tsai, B. K., D. W. Allen, L. M. Hanssen, B. Wilthan, and J. Zeng, A comparison of optical properties between high density and low density sintered PTFE, Proc. SPIE 7065,0Y, 2008.

Van Brug, H., and G. B. Courréges Lacoste, Spectral features, effects, and cures, Proc. SPIE 6677, 03, 2007.

Vermote, E., and Y.-J. Kaufman, Absolute calibration of AVHRR visible and near infrared channels using ocean and cloud views, Int. J. Remote Sens., 16, 13, 2317-2340, 1995.

Vermote, E., R. Santer, P.-Y. Deschamps, and M. Herman, In-flight calibration of large field of view sensors at shorter wavelengths using Rayleigh scattering, Int. J. Remote Sens., 13, 3409-3429, 1992.

Vermote, E., D. Tanré, J. L. Deuzé, M. Herman, and J. J. Morcrette, Second Simulation on the Satellite Signal in the Solar Spectrum: 6S: An overview, IEEE Trans. Geosci. Remote Sens., 35, 675-686, 1997.

Waluschka, E., X. Xiong, D. Moyer, B. Guenther, W. L. Barnes, and V. V. Salomonson, Modeling studies of the MODIS solar diffuser attenuation screen and comparison with on-orbit measurements, Proc. SPIE 5542, 342-353, 2004.

Wang, M., and H. R. Gordon, Calibration of ocean color scanners: how much error is acceptable in the near infrared? Remote Sens. Environ., 82, 497-504, 2002.

Wang, M., and H. R. Gordon, Retrieval of the columnar aerosol phase function and single scattering albedo from sky radiance over the ocean: Simulations, Appl. Opt., 32, 4598-4609, 1993.

Wang, Z., X. Xiong, and W. L. Barnes, Further investigation on MODIS solar diffuser screen vignetting function and its implementation in RSB calibration, Proc. SPIE, 8153, 8153-08, 2011.

World Meteorological Organization, A preliminary cloudless standard atmosphere for radiation computation, WMO Rep. 24, WCP-112, Geneva, Switzerland, 1986.

Xiong, X., N. Che, and W. L. Barnes, Terra MODIS on-orbit spectral characterization and performance, IEEE Trans. Geosci. Remote Sens., 44, 2198-22016, 2006.

Xiong, X., B. Wenny, J. Sun, A. Angal, A. Wu, H. Chen et al., Overview of Aqua MODIS 10-year on-orbit calibration and performance, Proc. SPIE 8533, 16-1, 2012.

Xiong, X., J. Sun, W. L. Barnes, V. V. Salomonson, J. Esposito, H. Erives, and B. Guenther, Multiyear on-orbit calibration and performance of Terra MODIS reflective solar bands, IEEE Trans. Geosci. Remote Sens., 45(4), 879-889, 2007.

Yoon, H. W., H. W., David W. A., G. P. Eppeldauer, and B. K. Tsai, The Extension of the NIST BRDF Scale from 1100 nm to 2500 nm, Proc. SPIE 7452, 2009.

Yoshida, M., and the GLI Calibration Team, GLI calibration results for ocean color channels, IOCCG Workshop on "In flight Calibration of Ocean-Color Sensors", Fremantle, Australia, 30 October 2004.

Zhang, T., and H. R. Gordon, Columnar aerosol properties over oceans by combining surface and aircraft measurements: sensitivity analysis, Appl. Opt., 36, 2650-2662, 1997.

Zibordi, G., Mélin, F., Berthon, J-F., Holben, B., Slutsker, I., Giles, D. et al., AERONET-OC: A network for validation of ocean color primary products, J. Atmos. Oceanic Technol., 26, 1634-1651, 2009.
Zimmermann, G., and A. Neumann, The imaging spectrometer experiment MOS on IRSP3 - three years of experience, J. Spacecraft Technol., 10, 1-9, 2000.